RECURRENT SPATIO-TEMPORAL STRUCTURES IN PRESENCE OF CONTINUOUS SYMMETRIES

A Thesis
Presented to
The Academic Faculty

by

Evangelos Siminos

In Partial Fulfillment
of the Requirements for the Degree
Doctor of Philosophy in the
School of Physics

Georgia Institute of Technology
version 2.0 April 6 2009

ACKNOWLEDGEMENTS

I would like to thank my advisor, Predrag Cvitanović, for his constant encouragement and support, for the time he put in my education and advisement, and for his patience with some of my bolder ideas. Numerics did rarely converge until Ruslan L. Davidchack stepped in and taught me how to do things correctly, always providing useful advice and totally changing the route of this thesis. Yueheng Lan has put a lot of effort in bequeathing his knowledge and experience in the problem, and I am grateful to him for pointing out to the existence of the E_1 equilibrium at the $L = 22$ system size among many other tips. I have profited from John F. Gibson's insights into phase space visualization of high-dimensional fluid flows, discussions with Jonathan Halcrow on desymmetrization of Lorenz and other flows, and I thank G. Robinson, Jr., National Science Foundation grant DMS-0807574 and Gerondelis Foundation for partial financial support. I thank Loukas Vlahos for initiating my interest in nonlinear dynamics during my undergraduate studies and his invaluable help in starting this journey.

I would like to thank my parents for their firm support and love that laid down the foundations for everything. Kalli has been cheerful company while I was writing this thesis and her keystrokes helped randomize the content. Last and most important, I would like to thank Sophia for her encouragement, support, patience and understanding that were so valuable in every stage of this work and made completing it possible.

TABLE OF CONTENTS

SUMMARY

When statistical assumptions do not hold and coherent structures are present in spatially extended systems such as fluid flows, flame fronts and field theories, a dynamical description of turbulent phenomena becomes necessary. In the dynamical systems approach, theory of turbulence for a given system, with given boundary conditions, is given by (a) the geometry of its ∞-dimensional phase space and (b) the associated measure, i.e., the likelihood that asymptotic dynamics visits a given phase space region.

In this thesis this vision is pursued in the context of Kuramoto-Sivashinsky system, one of the simplest physically interesting spatially extended nonlinear systems. With periodic boundary conditions, continuous translational symmetry endows phase space with additional structure that often dictates the type of observed solutions. At the same time, the notion of recurrence becomes relative: asymptotic dynamics visits the neighborhood of any equivalent, translated point, infinitely often. Identification of points related by the symmetry group action, termed symmetry reduction, although conceptually simple as the group action is linear, is hard to implement in practice, yet it leads to dramatic simplification of dynamics.

Here we propose a scheme, based on the method of moving frames of Cartan, to efficiently project solutions of high-dimensional truncations of partial differential equations computed in the original space to a reduced phase space. The procedure simplifies the visualization of high-dimensional flows and provides new insight into the role the unstable manifolds of equilibria and traveling waves play in organizing Kuramoto-Sivashinsky flow. This in turn elucidates the mechanism that creates unstable modulated traveling waves (periodic orbits in reduced space) that provide a skeleton of the dynamics. The compact description of dynamics thus achieved sets the stage for reduction of the dynamics to mappings between a set of Poincaré sections.

CHAPTER I

INTRODUCTION

1.1 Dynamicist's vision of turbulence

This thesis is part of a wider effort [23] to describe turbulence from a dynamical systems perspective that goes back to the seminal paper of Hopf [49]. The relation of dynamics to turbulence underlies many fundamental developments in dynamical systems theory, from the very (re)discovery of chaos by Lorenz [63] to the Ruelle-Takens [76] view of turbulence, to the work on inertial manifolds [15] of partial differential equations (PDEs). The emphasis here is not on the transition to turbulence or on the derivation of reduced models of a partial differential equation. On the contrary we ask: For a given system, with given boundary conditions, which we are able to numerically simulate to sufficient accuracy to resolve its finest features, how do we develop a dynamical description? Hopf's answer [49] is to consider the dynamics of a PDE not as the evolution of snapshots of the underlying field but as dynamics on an ∞-dimensional phase space in which every point corresponds to a state of the system. In this space a generic turbulent trajectory visits neighborhood of a "regular" solution for a while, then switches to another one, and so on. For any given system, parameter values and boundary conditions there are two ingredients to implementing this vision: (a) the geometry of the phase space and (b) the associated natural measure, i.e., the likelihood that asymptotic dynamics visits a given phase space region.

To explain what we mean by geometry of phase space of a dynamical system, let us consider a finite dimensional system of coupled ordinary differential equations of the form

$$\frac{dx}{dt} = v(x)\,, \tag{1}$$

where $x\,,\ v \in \mathbb{R}^N$. The trajectory $f^t(x_o)$ of an initial condition x_o is obtained by integrating (1).

The simplest solution that might exist in such a system is an *equilibrium* point that is left invariant by the flow, $f^t(x_o) = x_o$ for all times. When we examine the neighborhood of the equilibrium we find that it can be decomposed into a (local) *stable subspace* along which points converge towards the equilibrium and a (local) *unstable subspace* along which points stray away from the equilibrium under time evolution (for the time being *center subspaces* along which neither happens will be ignored). The global continuation of the stable (unstable) subspace under backward (forward) time evolution is the *stable (unstable) manifold* of the equilibrium. Stable and unstable manifolds are *flow-invariant*: the trajectory through any point on the manifold stays on it for all times. Invariant manifolds provide topological obstructions for any other solution: as a trajectory cannot cross an invariant manifold, it is forced to follow its stretching and folding. In nonlinear systems studied in this thesis, the unstable manifolds are stretched away from an equilibrium until nonlinearity causes them to fold sharply back. This provides a basic mechanism for *recurrence*: trajectories of points in the *non-wandering set* return arbitrarily close to the initial point. This set of non-wandering orbits, which for dynamics that are locally expanding (there are directions along which we depart away from any solution) and globally mixing (we are always forced to fold back) we will loosely identify with the *chaotic attractor*, contains the "regular" solutions

in Hopf's vision: periodic orbits that close after finite time,

$$x(t+T) = x(t)\,, \tag{2}$$

where T the period. Periodic orbits provide a complete characterization of the topology of a chaotic attractor in low dimensional systems [39], and most importantly they can be used to quantitatively approximate the natural measure and calculate "observable" quantities, such as Lyapunov exponents and escape rates, within the framework of periodic orbit theory [20], briefly summarized here in Appendix B. The reason we refer here to the totality of phase space relations between invariant solutions as "geometry" rather than "topology" is that we are not only interested in elucidating the topological mechanisms that result in recurrences but also in the exact phase space positions of invariant objects, such as periodic orbits, and metric distances between different solutions.

The first successful quantitative implementation of Hopf's vision for a spatially extended system, to the best of the author's knowledge, can be found in Christiansen *et al.* [14]. The object of study was Kuramoto-Sivashinsky system, a dissipative PDE in one spatial dimension, as one of the simplest systems that exhibits features reminiscent of fluid turbulence (see Chapter 5 for details). A large set of periodic orbits, embedded into the attractor and ordered hierarchically was located. Shorter orbits provided the basic building blocks of the attractor, while longer ones contributed quantitative corrections to periodic orbit averages. This investigation was continued for a "more turbulent" Kuramoto-Sivashinsky system by Y. Lan and Cvitanović [58; 60].

Recently, phase space of moderate Reynolds number wall bounded shear flows became experimentally [47] and computationally [54; 27; 81; 80; 38] accessible. The charting of Navier-Stokes phase space, for specific boundary conditions, with equilibria, relative equilibria and heteroclinic connections has provided the basic elements of the geometry of the turbulent flow and there is hope that it will eventually lead to approximation of the natural measure using a set of "regular" solutions.

1.2 Contribution of this thesis

The research undertaken here is a part and parcel of the common effort of a large community of scientists, engineers and mathematicians, working toward the grand goal of developing an effective dynamical theory of turbulent phenomena in spatially extended systems such as fluid flows, flame fronts and field theories. The literature is vast and bewildering. Let us start by a quote from an imaginary (but typical) paper: "We have demonstrated our method on the example of Kuramoto-Sivashinsky equation but it is completely general and applicable to any other PDE. Application to Navier-Stokes is left as an exercise to the reader."

While in practice the application of the method to more complicated problems turns out to be far from trivial, the exercise leads one to critically re-examine several steps along the way that the above quoted imaginary paper (profound as it might be) only glossed over. A rich, perhaps beautiful, and –surprisingly– not yet fully explored vein turns out to be the role continuous symmetries play in detailed dynamical explorations of 'turbulent' flows. They are the red thread through the journey undertaken in this thesis.

1.2.1 Kuramoto-Sivashinsky equation

The Kuramoto-Sivashinsky system in one spatial dimension

$$u_t = F(u) = -\tfrac{1}{2}(u^2)_x - u_{xx} - u_{xxxx}\,, \qquad x \in [-L/2, L/2] \tag{3}$$

has been derived in a variety of contexts (see Chapter 5) including the dynamics of reaction-diffusion systems and fluttering flame fronts, and has been studied extensively as one of the simplest systems that shares common features with the Navier-Stokes description of incompressible fluids. Like Navier-Stokes equations, it contains a term that pumps energy into the system (u_{xx}) and a term that dissipates it (u_{xxxx}). It is transitionally invariant under periodic boundary condition $u(x + L, t) = u(x, t)$ or in an unbounded domain $x \in (-\infty, \infty)$, a feature also present in many physical fluid flows. In refs. [14; 60; 58] dynamics was restricted to the space of antisymmetric functions $u(-x, t) = -u(x, t)$ by imposing boundary condition $u(-L/2, t) = u(L/2, t) = 0$, *cf.* Sect. 5.1 for more details, thus eliminating translational symmetry. Even though working in the antisymmetric subspace is mathematically and computationally convenient and the dynamics are far from trivial, many of the physically important phenomena, such as traveling waves are eliminated by this restriction. Traveling solutions, however, are present in most of the fluid simulations and experiments mentioned in Sect. 1.1 and ubiquitous in physics.

As soon as we relax the antisymmetric boundary conditions and choose to work with periodic boundaries, Kuramoto-Sivashinsky equation becomes invariant under the 1-d Lie group of $O(2)$ translations: if $u(x, t)$ is a solution, then $u(x + d, t)$ is an equivalent solution for any $-L/2 < d \leq L/2$. As a result, KS can have *traveling wave* or *relative equilibrium* solutions,

$$u(x, t) = u_o(x - ct) \tag{4}$$

where c the constant velocity of the wave and $u_o(x)$ its profile. Furthermore, it can have *modulated traveling wave* or *relative periodic orbit* solutions,

$$u(x + d, T + t) = u(x, t)\,, \tag{5}$$

where T the period and d a translation. Thus recurrence becomes relative: The periodic orbits that organized phase space in refs. [14; 60; 58] are now not the only generic compact solutions, we are also faced with relative periodic orbits, solutions that repeat up to a translation. They were already noted by Poincaré in his study of the 3-body problem [10; 79]. In PDEs they are also known as modulated traveling waves and they have been found and studied, for example in Kuramoto-Sivashinsky equation [7], Complex Ginzburg-Landau equation [62], and plane Couette flow [80]. A recent application of relative periodic orbits has been the discovery of "choreographies" of N-body problems [12; 11; 67].

The main purpose of this thesis will be to investigate the role played by relative equilibria (traveling waves) and relative periodic orbits in the geometry of spatially extended systems with continuous symmetry. Following on the earlier work, we concentrate on Kuramoto-Sivashinsky equation as it provides a simpler system for the illustration of key ideas than the technically much more demanding Navier-Stokes equations. Yet, in the spirit of the above quoted imaginary paper, we emphasize that we develop methods in a way that can be applicable in other PDEs. The choice of Kuramoto-Sivashinsky system size is such that the dynamics in the physical space looks nothing like "fully developed turbulence." Instead, the dynamics is dominated by *coherent structures*, that is localized, persistent structures. This is precisely the kind of dynamics in which statistical assumptions [34] fail

and which requires a dynamical systems description in the spirit of Hopf. In Chapter 5 we review Kuramoto-Sivashinsky equation in detail and in Chapter 7 we study its phase space, through equilibria, traveling waves, heteroclinic connections and relative periodic orbits, for a specific "box" size. In Appendix B –in a way of motivating the enterprize undertaken in the main body of the thesis– we describe our attempt to organize a set of 30,000 periodic orbits and relative periodic orbits computed by Davidchack [25] in the context of periodic orbit theory, without an understanding how these orbits are organized geometrically. Failure of this attempt leaves no option but to understand the geometry of phase space first, label the orbits, find missing ones, and then use cycle expansions. The first step in achieving this would be a "compactification" of the phase space by quotienting out the continuous symmetry, or "symmetry reduction."

1.2.2 Symmetry reduction

Taking it into account a symmetry of a physical system usually leads to simplification of the problem. Indeed, in linear theories, such as quantum mechanics, symmetry is often exploited through separation of variables. In Hamiltonian mechanics it leads to conserved quantities which can often be directly exploited. For instance in the central force problem conservation of angular momentum fixes the plane of motion. In general exploiting symmetry by identifying points in space or solutions related by a symmetry operation is the objective of *symmetry reduction*. The subject has a long history in Hamiltonian mechanics and for general systems and group actions it usually is rather technical and highly non-trivial, see for example refs. [66; 65; 18].

We motivate the need for symmetry reduction by a preview of the results in the case of 5-dimensional, SO(2)-symmetric Complex Lorenz equations that will be used as our illustrative example in Chapter 4. A quick comparison of Figure 10 and the continuous symmetry reduced Figure 14 counterpart should demonstrate the problem. Under continuous symmetry the "stretch and fold" mechanism that determines the topology of the attractor is hidden by the, dynamically irrelevant, motion in the group direction. More importantly the dynamics can be described by the one dimensional first return map of Figure 15. Eliminating time-translational invariance by means of a Poincaré section is familiar to the reader as a way of obtaining a discrete time map from a continuous time flow. In the presence of continuous symmetry one also needs to eliminate the less interesting linear group invariance by some means before one can obtain the return map of Figure 15.

Here we will concentrate on dissipative dynamical systems and high-dimensional truncations of PDEs. The main problems we are facing are: 1) the high dimensionality of phase space, 2) the structure of the phase space induced by the symmetry group action (see Sect. 2.1.1) which usually prevents carrying out reduction globally. High dimensionality does not allow us to use a very powerful tool in symmetry reduction, *Hilbert bases*. The idea is to form from the equivariant variables (that commute with the group action, see Sect. 2.1) polynomials invariant under the group action, and rewrite the dynamics in terms of these (see Sect. 2.3). Unfortunately, the determination of a Hilbert basis appears computationally prohibitive for phase-space dimensions larger than ten [13; 35]. Moreover, even if such a basis were available, rewriting the equation of motion in a basis of invariant polynomials appears impractical for high-dimensional flows. Here we shall circumvent these difficulties by solving the equations in the equivariant variables, but plotting the solutions in terms of the invariant variables.

A different approach to symmetry reduction of PDEs has been presented by Rowley and

Marsden [75], formulated in the context of Karhunen-Loève expansion, but also applicable to direct numerical simulations [74]. The method allows one to integrate a PDE defined in the *reduced space* along with a *reconstruction equation* that allows the dynamics in the original space to be recovered. As noted in ref. [75] the reconstruction equation can fail for reasons related to the structure of phase space under the group action, and one would be forced to cover the reduced space with local coordinate charts. As the latter procedure is not straightforward to implement and we do not want to sacrifice the ability to move back and forth between the initial and the reduced phase space while obtaining, to some extend, a global picture of the reduced dynamics, we will need to take a different path.

Our approach to symmetry reduction is centered around the method of moving frames of Cartan [8] that we present in the formulation of Fels and Olver [28] in Sect. 2.3.2. It allows the determination of (non-polynomial) invariants of the group action by a simple and efficient algorithm that works well in phase space dimension of order 100. Invariants generated for Complex Lorenz equations (see Sect. 4.1.2.2) and for Kuramoto-Sivashinsky equation (see Sect. 8.1) are singular in subsets of phase space, again due to the special structure of the phase space under the group action. We modify these invariants so that there is no singularity in regions of dynamical interest and visualize dynamics of invariant objects in reduced phase space by mapping solutions computed in the original space to this basis.

Visualization in reduced space provides insight in its geometry and facilitates the choice of local Poincaré sections as the first step in our attempt to describe the flow by iteration of setion-to-section maps. Choosing Poincaré sections on which the invariants determined by the moving frame method are not singular allows for a crucial simplification of the reduction process: it allows reduction through a linear transformation at any point on the Poincaré section, see Sect. 4.1.2.2. This simplification allows one to perform the reduction procedure for points of intersection of solutions with the Poincaré section very efficiently, even for very high dimensional spaces.

For Kuramoto-Sivashinsky equation construction of discrete time maps in reduced phase space is still a subject of ongoing work, see Chapter 9. Yet the reward of applying this procedure for visualization is that, when continuous symmetry is quotiented out, relative periodic orbits become periodic, traveling waves become equilibria, the dimensionality of their unstable manifolds is reduced by the dimension of the group and our understanding of the role solutions play is dramatically enhanced. For example, after symmetry reduction of Kuramoto-Sivashinsky flow we are able to visualize the unstable manifold of a traveling wave in a compact manner and connect it to the mechanisms associated to recurrence within the "chaotic attractor", see Chapter 8.

1.2.3 Updated version of this thesis

The Georgia Tech Ph.D. thesis is an educational project that has come to an end, but it is also an ongoing research project. Errors and omissions are certainly present in the official Georgia Tech submission. The author will make every effort to correct them, with the updated, pdf-hyperlinked, printer friendly version available in `ChaosBook.org`, under the link to theses. We recommend that the reader download this updated version.

CHAPTER II

THE ROLE OF SYMMETRY

In this chapter we provide a brief overview of the role of symmetries in differential equations, restricted to finite dimensional groups acting linearly and globally on $\mathbb{R}^n$. The subject of symmetries of dynamical systems is vast and covered in many monographs and review articles. We summarize the results from the literature that will be needed in applications to the problem at hand, referring the reader to the literature for proofs of well established results.

2.1 Symmetries of dynamical systems

We consider a system of ODEs of the form

$$\dot{x} = v(x, \lambda) \tag{6}$$

where $v : \mathbb{R}^n \times \mathbb{R}^r \to \mathbb{R}^n$ a C^∞ mapping. When not important we will suppress the r-dimensional vector of parameters λ in the notation.

Any compact Lie group acting on $\mathbb{R}^n$ can be identified with a subgroup of $\mathrm{O}(n)$, *cf.* for example ref. [41] for a sketch of the proof. Therefore, without loss of generality we will concentrate on subgroups $\Gamma \subseteq \mathrm{O}(n)$ in the following.

Definition 2.1 *We call a group element $\gamma \in \mathrm{O}(n)$ a symmetry of (6) if for every solution $x(t)$, $\gamma x(t)$ is also a solution.*

The question now arises on how to check for symmetries of (6) since we generally do not have knowledge of the set of solutions. Let $x(t)$ be a solution of 6. Then by Definition 2.1 $y(t) = \gamma x(t)$ is another solution and therefore satisfies (6):

$$\dot{y}(t) = v(y(t)) = v(\gamma x(t))\,.$$

On the other hand

$$\dot{y}(t) = \gamma \dot{x} = \gamma v(x(t))\,,$$

for any solution $x(t)$. Since solutions exist for any $x \in \mathbb{R}^n$ we are led to the following condition for γ to be a symmetry of (6):

$$v(\gamma x) = \gamma v(x) \tag{7}$$

for all $x \in \mathbb{R}^n$. We say that v *commutes* with γ or that v is γ-*equivariant*. When v commutes with all $\gamma \in \Gamma$ we say that v is Γ-equivariant. In physics literature the term *invariant* is most commonly used, mostly because in Hamiltonian systems symmetry is manifested as invariance of the Hamiltonian under the symmetry operation. Clearly the finite time flow $f^t(\gamma x_o)$ through γx_o satisfies the equivariance condition $f^t(\gamma x_o) = \gamma f^t(x_o)$ from definition of symmetry and uniqueness of solutions.

Example 2.2 *The vector field in Lorenz equations (36) is equivariant under the group* $\mathrm{Z}_2 \cong \mathrm{D}_1$ *acting on* $\mathbb{R}^3$ *by*

$$R(\pi)(x, y, z) = (-x, -y, z)\,.$$

Note that this transformation can be considered either as rotation by π *around the* z *axis (hence the group* Z_2*) or as reflection about the origin in a plane perpendicular to the* z*-axis (hence the group* D_1*.)*

Example 2.3 *The vector field in Complex Lorenz equations (50) is equivariant under the group* $\mathrm{SO}(2)$ *acting on* $\mathbb{R}^5 \cong \mathbb{C}^2 \times \mathbb{R}$ *by*

$$R(\theta)(x, y, z) = (e^{i\theta}x, e^{i\theta}y, z)\,, \quad \theta \in [0, 2\pi)\,. \tag{8}$$

Example 2.4 *Finally, the symmetry group of the Armbruster-Guckenheimer-Holmes flow*

$$\dot{z}_1 = \bar{z}_1 z_2 + z_1\left(\mu_1 + e_{11}|z_1|^2 + e_{12}|z_2|^2\right) \tag{9a}$$
$$\dot{z}_2 = \pm z_1^2 + z_2\left(\mu_2 + e_{21}|z_1|^2 + e_{22}|z_2|^2\right) \tag{9b}$$

is $\mathrm{O}(2)$ *acting by*

$$R(\theta)(z_1, z_2) = (e^{i\theta}z_1, e^{i2\theta}z_2)\,, \quad \theta \in [0, 2\pi)\,, \tag{10a}$$
$$\kappa(z_1, z_2) = (z_1^*, z_2^*)\,. \tag{10b}$$

where * denotes complex conjugation.

2.1.1 Phase space stratification

In order to understand the implications of equivariance for the solutions of (6) we first have to examine the way a compact Lie group acts on $\mathbb{R}^n$.

The *group orbit* of $x \in \mathbb{R}^n$ is the set

$$\Gamma x = \{\gamma x : \gamma \in \Gamma\}\,. \tag{11}$$

Definition 2.5 *The isotropy subgroup or stabilizer of* $x \in \mathcal{M}$ *as*

$$\Sigma_x = \{\gamma \in \Gamma : \gamma x = x\}\,. \tag{12}$$

Thus the isotropy subgroup describes the symmetries of a point x. Note that by Definition 2.5 the isotropy subgroup is the largest subgroup (in the sense of set inclusion, *cf.* (16)) that leaves x fixed.

Lemma 2.7 *Points on the same group orbit of* Γ *have conjugate isotropy subgroups:*

$$\Sigma_{\gamma x} = \gamma \Sigma_x \gamma^{-1}\,. \tag{13}$$

(See ref. [41] for the proof.) Thus we can characterize a group orbit by its *type*, defined as the conjugacy class of its isotropy subgroups.

Proposition 2.8 *Let* Γ *be a compact Lie group acting on* $\mathbb{R}^n$*. Then*

1. *If* Γ *is finite then* $|\Gamma| = |\Sigma_x||\Gamma x|$.

2. If Γ *is continuous then* $\dim \Gamma = \dim \Sigma_x + \dim \Gamma x$.

The proof can be found in ref. [41]. Here $|\,.\,|$ denotes the *order* of the group, that is the number of group elements. We note that $\dim \Gamma x = \dim(\Gamma/\Sigma_x)$, where the *coset space* of a subgroup Σ of Γ is defined as $\Gamma/\Sigma = \{\gamma\Sigma | \gamma \in \Gamma\}$. Also recall that the (left) *cosets* of Σ in Γ are the sets $\gamma\Sigma = \{\gamma\sigma | \sigma \in \Sigma\}$.

Therefore, when Γ is continuous each group orbit is a smooth compact manifold of dimension $\dim \Gamma x = \dim \Gamma - \dim \Sigma_x$. The union of orbits of the same type is called a *stratum* and is itself a smooth manifold. Thus $\mathbb{R}^n$ is stratified by the action of Γ into a disjoint union of strata $\mathcal{S}_i$ which are in an one to one correspondence to the group orbit types (*cf.* ref. [13] for proof). Note that in general the strata do not have the same dimension. There exists a unique stratum $\mathcal{S}_0$ of maximal dimension that is called *principal stratum* [35]. The principal stratum is open, dense and if Γ is connected then $\mathcal{S}_0$ is also connected [13].

Definition 2.9 *Let* Σ *be a subgroup of* Γ *acting on* $\mathbb{R}^n$. *The fixed-point subspace of* Σ, *denoted by* $Fix(\Sigma)$, *is the subspace of* $\mathbb{R}^n$ *containing all fixed points of* Σ:

$$Fix(\Sigma) = \{x \in \mathbb{R}^n \mid \sigma x = x\,,\ \forall \sigma \in \Sigma\}\,.$$

Fixed-point subspaces are invariant under equivariant dynamics. The following theorem applies:

Theorem 2.10 *Let* $f : \mathbb{R}^n \to \mathbb{R}^n$ *be* Γ*-equivariant and let* Σ *be a subgroup of* Γ. *Then*

$$f\left(Fix(\Sigma)\right) \subseteq Fix(\Sigma)\,.$$

This leads to:

Proposition 2.11 *Let* $x(t)$ *be a solution trajectory of an equivariant ODE. Then* $\Sigma_{x(t)} = \Sigma_{x(0)}$ *for all* t.

Proof can be found in ref. [41].

Let $A(x) = \frac{\partial v(x)}{\partial x}$ and use the chain rule:

$$A(\gamma x)\gamma = \gamma A(x)\,, \qquad \gamma \in \Gamma\,. \tag{14}$$

Then, for $\gamma \in \Sigma_x$ we have

$$A(x)\gamma = \gamma A(x)\,, \qquad \gamma \in \Sigma_x. \tag{15}$$

i.e.the stability matrix at x commutes with Σ_x.

We can define a partial ordering $\preceq$ on conjugacy classes of subgroups of Γ. Let $H = \{H_i\}$ and $K = \{K_j\}$ be two such conjugacy classes. Then

$$H \preceq K \Leftrightarrow H_i \subseteq K_j \tag{16}$$

for some representatives H_i, K_j. We refer to the partially ordered set that results from this ordering as the *subgroup lattice*.

Definition 2.12 *The isotropy lattice of* Γ *is the set of all conjugacy classes of isotropy subgroups partially ordered by* $\preceq$.

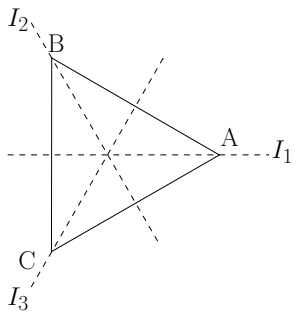

Figure 1: D_3 leaves the equilateral triangle setwise fixed. The reflection symmetry axes have been denoted I_i.

Definition 2.13 *Let Σ be a subgroup of Γ. The normalizer of Σ in Γ is $N(\Sigma) = \{\gamma \in \Gamma \,|\, \gamma\Sigma\gamma^{-1} = \Sigma\}$.*

Lemma 2.14 *The largest subgroup of Γ that acts in $\mathrm{Fix}\,(\Sigma)$ is $N(\Sigma)$.*

For proof *cf.* ref. [13].

Example 2.15 *Consider D_3, the symmetry group of the equilateral triangle Figure 1, acting on $\mathbb{R}^2 \cong \mathbb{C}$ by*

$$\zeta z = e^{i\frac{2\pi}{3}} z\,, \tag{17a}$$

$$\kappa z = \bar{z}\,. \tag{17b}$$

There are, up to conjugacy, three subgroups: $\mathbf{1} = \{e\}$, $\mathrm{D}_1(\kappa) = \{e\,, \kappa\}$, which is isomorphic to the subgroups generated by $\kappa\zeta$ and by $\kappa\zeta^2$, and $\mathrm{C}_3 = \{e, \zeta, \zeta^2\}$. The subgroup lattice is shown in Figure 2(a). There are three classes, each corresponding to a distinct geometrical operation: $\{e\}, \{\kappa, \kappa\zeta, \kappa\zeta^2\}$ and $\{\zeta, \zeta^2\}$.

Example 2.16 *We now examine how the vertex A of the triangle transforms under the action of D_3. Under ζ and ζ^2 it is mapped to the vertices B and C, respectively. Thus all vertices belong to the same group orbit and have conjugate isotropy subgroups, from Lemma 2.7. Under κ vertex A remains fixed. Thus the isotropy subgroup of point A is $\Sigma_A = \mathrm{D}_1(\kappa)$. By Lemma 2.7 we have $\Sigma_B = \zeta\,\mathrm{D}_1(\kappa)\,\zeta^{-1} = \mathrm{D}_1(\kappa\zeta)$ and $\Sigma_C = \zeta^{-1}\,\mathrm{D}_1(\kappa)\,\zeta = \mathrm{D}_1(\kappa\zeta^2)$. Next, note that $\mathrm{D}_1(\kappa)$ fixes any point on the symmetry axis I_1, while ζ and ζ^2 map it to I_2 and I_3, respectively. The origin is the only point fixed by any group operation, i.e. has isotropy subgroup D_3. Finally, any point that is not on one of the symmetry axes I_1, I_2, I_3 has trivial isotropy subgroup. Thus we arrive to the following conclusions:*

*The isotropy subgroups are: $\Sigma_{\{0\}} = \mathrm{D}_3$, $\Sigma_{I_1^*} = \mathrm{D}_1(\kappa) \simeq \Sigma_{I_2^*} \simeq \Sigma_{I_3^*}$, $\Sigma_{\mathbb{R}^2\backslash\{\cup I_i\}} = \mathbf{1}$, where $I_i^* = I_i\backslash\{0\}$. The fixed point subspaces of D_3, $\mathrm{D}_1(\kappa)$, $\mathrm{D}_1(\kappa\zeta)$ and $\mathrm{D}_1(\kappa\zeta^2)$ are the origin, I_1, I_2 and I_3, respectively. The fixed point subspace of C_3 is the origin but, since C_3 is a proper subgroup of D_3, it does not qualify as isotropy subgroup of the origin (*cf. *Definition 2.5.) Thus C_3 is not in the isotropy lattice of D_3 acting on $\mathbb{R}^2$,* cf. *Figure 2(b).*

There are three strata in correspondence with the orbit types (and with isotropy subgroups): the origin (type D_3), $\{\cup I_i^*\}$ (type $\mathrm{D}_1(\kappa)$), and the principal stratum $\mathbb{R}^2\backslash\{\cup I_i\}$ (type $\mathbf{1}$).

If we now consider a two dimensional system of ODEs equivariant under the action (17) of D_3 we can conclude immediately that the fixed-point subspaces are flow invariant by

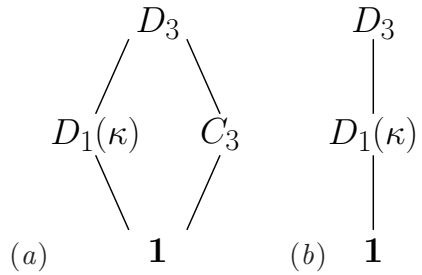

Figure 2: (a) D_3 subgroup lattice, (b) D_3 isotropy lattice

Proposition 2.11. Thus the origin has to be a fixed point of the flow. Moreover the principal stratum $\mathbb{R}^2\backslash\{\cup I_i\}$ is partitioned by the symmetry axes I_i that are flow invariant into six disjoined pieces on the same group orbit of D_3.

Example 2.17 *Consider $\Sigma = \mathrm{SO}(2)$ acting on $\mathbb{R}^5$ by*

$$x \mapsto R(\theta)x\,, \tag{18}$$

where

$$R(\theta) = \begin{pmatrix} \cos(\theta) & -\sin(\theta) & 0 & 0 & 0 \\ \sin(\theta) & \cos(\theta) & 0 & 0 & 0 \\ 0 & 0 & \cos(\theta) & -\sin(\theta) & 0 \\ 0 & 0 & \sin(\theta) & \cos(\theta) & 0 \\ 0 & 0 & 0 & 0 & 1 \end{pmatrix}, \quad \theta \in [0, 2\pi)\,. \tag{19}$$

Note that this is the same action as in (8) but now we do not make the identification $\mathbb{R}^5 \cong \mathbb{C}^2 \times \mathbb{R}$. As we will see in Chapter 4 the following have direct applications in symmetry reduction of Complex Lorenz equations. Choose coordinates x_1, x_2, y_1, y_2, z on $\mathbb{R}^5$, related to the complex coordinates of (8) by $x = x_1 + ix_2$, $y = y_1 + iy_2$. The fixed-point subspace of the action of $\mathrm{SO}(2)$ is the z-axis. The isotropy subgroup of the z-axis is thus $\mathrm{SO}(2)$, while the isotropy subgroup of $\mathcal{M}^* \equiv \mathbb{R}^5\backslash\{x_1 = x_2 = y_1 = y_2 = 0\}$ is the identity element.

Example 2.18 *Consider the action of $\mathrm{O}(2)$ on $\mathbb{C}^n$ by*

$$R(\theta)z_k = e^{ik\theta}z_k\,,\ \theta \in [0, 2\pi)\,, \tag{20}$$

$$\kappa z = \overline{z}\,,\ z = (z_1, \ldots z_n)\,, \tag{21}$$

where $z_k \in \mathbb{C}$. The subgroup lattice is drawn in Figure 3. The subgroup D_m, $m > 0$, of $\mathrm{O}(2)$ is generated by the reflection κ and a rotation $R_m \equiv R(2\pi/m)$. The cyclic subgroup C_q, $q > 0$ of $\mathrm{SO}(2)$ is generated by a discrete rotation R_q. If q divides m then we have the following subgroup classes ordering relations: $\mathrm{C}_q \prec \mathrm{C}_m \prec \mathrm{D}_m$ and $\mathrm{D}_q \prec \mathrm{D}_m$. Note that $\mathrm{C}_1 \cong \mathbf{1}$.

The fixed-point subspace of $\mathrm{O}(2)$ and $\mathrm{SO}(2)$ is the origin and thus $\mathrm{SO}(2)$ is not in the isotropy lattice. The fixed-point subspace of C_q is given by the condition

$$z_k = 0 \text{ unless } k = qj\,,\ j = 1, \ldots \lfloor n/q \rfloor \tag{22}$$

and is thus a $2\lfloor n/q \rfloor$-dimensional subspace (here we count real dimensions.) For the fixed-point subspace of D_q we have condition (22) and additionally that

$$Im(z_k) = 0 \text{ for } k = 1, \ldots, n\,. \tag{23}$$

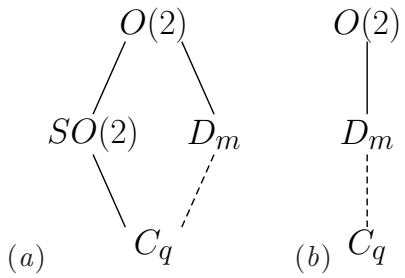

Figure 3: (a) O(2) subgroup lattice, (b) O(2) isotropy lattice for the action defined by (21). In both figures dashed lines indicate containment only when q divides m, while the relations $\mathrm{C}_q \prec \mathrm{C}_m$ and $\mathrm{D}_q \prec \mathrm{D}_m$ when q divides m are not drawn. For the isotropy lattice $m, q \leq n$.

Therefore $\mathrm{Fix}\left(\mathrm{D}_q\right)$ *is an* $\lfloor n/q \rfloor$*-dimensional subspace. Note that for* $q > n$ *condition (22) cannot be satisfied and all* z_k*'s have to be equal to zero. This implies that the fixed-point subspace of* D_q *and* C_q *for* $q > n$ *is the origin and as a result those subgroups are not in the isotropy lattice. Finally,* $\mathrm{Fix}\left(\mathbf{1}\right) = \mathbb{R}^n$.

Points on the group orbit of a point $x \in \mathrm{Fix}\left(\mathrm{D}_m\left(\kappa, R_m\right)\right)$ *have, by Lemma 2.7 conjugate isotropy subgroups:* $\Sigma_{R(\theta)x} = R(\theta)\mathrm{D}_m\left(\kappa, R_m\right)R(-\theta) \simeq \mathrm{D}_n\left(\kappa R(\theta), R_m\right)$. *The fixed-point subspace of* $\mathrm{D}_n\left(\kappa R(\theta), R_m\right)$ *is obtained by rotation* $R(\theta)$ *of* $\mathrm{Fix}\left(\mathrm{D}_m\left(\kappa, R_m\right)\right)$.

On the other hand $\mathrm{Fix}\left(\mathrm{C}_m\right)$ *is invariant as a set under the action of* $\mathrm{O}(2)$. *To understand this observe that for any* $0 \leq m \leq n$, $N(\mathrm{C}_m) = \mathrm{O}(2)$ *since* $\mathrm{SO}(2)$ *is abelian while* $\kappa \mathrm{C}_m \kappa^{-1} = \mathrm{C}_m$ *since* $\kappa R_{m/k} \kappa^{-1} = R_{-m/k} \in \mathrm{C}_m, \forall\, k = 1 \ldots m$. *Therefore* $\mathrm{O}(2)$ *acts on* $\mathrm{Fix}\left(\mathrm{C}_m\right)$, *i.e. the group orbit of any point on* $\mathrm{Fix}\left(\mathrm{C}_m\right)$ *remains on* $\mathrm{Fix}\left(\mathrm{C}_m\right)$. *On the other hand* $N(\mathrm{D}_m(\kappa, R_m)) = \mathrm{D}_m(\kappa, R_m)$ *and thus only* $\mathrm{D}_m(\kappa, R_m)$ *acts (trivially) on* $\mathrm{Fix}\left(\mathrm{D}_m(\kappa, R_m)\right)$.

It's interesting to note the way in which fixed-point subspaces are nested: if $\mathrm{D}_m \subset \mathrm{D}_q$ *then* $\mathrm{Fix}\left(\mathrm{D}_m\right) \supset \mathrm{Fix}\left(\mathrm{D}_q\right)$. *If* $\mathrm{C}_m \prec \mathrm{C}_q$ *then* $\mathrm{Fix}\left(\mathrm{C}_m\right) \supset \mathrm{Fix}\left(\mathrm{C}_q\right)$ *and finally if* $\mathrm{C}_m \subset \mathrm{D}_q$ *then* $\mathrm{Fix}\left(\mathrm{C}_m\right) \supset \mathrm{Fix}\left(\mathrm{D}_q\right)$.

A general procedure exists [35] to determine which subgroups in the subgroup lattice of a group Γ are isotropy subgroups when Γ acts faithfully on $\mathbb{R}^n$. For each subgroup K (or more precisely for each subgroup class represented by K) determine the dimension of the fixed-point subspace. Then we trace the subgroup lattice: For each subgroup K we compare $\dim(Fix(K))$ to $\dim(Fix(H))$ for every $H \subseteq \Gamma$ for which $K \subset H$. If $\dim(Fix(K)) = \dim(Fix(H))$ then K is not an isotropy subgroup. The determination of the dimension of the fixed-point subspace of a subgroup K can be done by means of the following trace formula if an explicit representation $\rho(K)$ of K is known or if one is able to determine the character of the representation by other means:

$$\dim(Fix(K)) = \frac{1}{|K|} \sum_{\kappa \in K} \mathrm{trace}\left(\rho(\kappa)\right). \tag{24}$$

2.1.2 Group action types

In this section we state some definitions of different types of group actions.

Definition 2.19 *A group* Γ *acts freely on* $\mathcal{M}$ *if all isotropy subgroups are trivial:* $\Sigma_x = \{e\}$ *for all* $x \in \mathcal{M}$. Γ *acts locally freely if all isotropy subgroups are discrete subgroups of* Γ.

Example 2.20 *The action (18) of* $\mathrm{SO}(2)$ *on* $\mathbb{R}^5$ *is not free (or even locally free), while the same action on* $\mathcal{M}^*$ *is free. If we do not restrict* θ *in* $[0, 2\pi)$ *then the group* $\mathbb{R}$ *acts locally freely on* $\mathcal{M}^*$ *since the isotropy subgroup is the discrete subgroup* $2\pi\mathbb{Z}$ *of integer multiples of* 2π.

Example 2.21 *The action (21) of* $\mathrm{O}(2)$ *is locally free on* $\mathbb{C}^n \setminus \{0\}$ *but not on* $\mathbb{C}^n$.

Definition 2.22 *A group* Γ *acts faithfully (or effectively) on* $\mathcal{M}$ *if and only if* $\bigcup_{x\in\mathcal{M}} \Sigma_x = \{e\}$.

An immediate consequence of Lemma 2.14 is that $N(\Sigma)/\Sigma$ acts faithfully on $\mathrm{Fix}\,(\Sigma)$.

Example 2.23 *The actions (18) of* $\mathrm{SO}(2)$ *and (21) of* $\mathrm{O}(2)$ *are faithful.*

Definition 2.24 *A group* Γ *acts semi-regularly on* $\mathcal{M}$ *if all its orbits have the same dimension. If in addition for each point* $x \in \mathcal{M}$ *there exists an arbitrarily small neighborhood* U *such that each orbit of* Γ *intersects* U *in a pathwise connected subset, then the group acts regularly.*

Example 2.25 *Action (18) of* $\mathrm{SO}(2)$ *is regular on* $\mathcal{M}^*$ *but not on* $\mathbb{R}^5$.

Example 2.26 *Since the action (21) of* $\mathrm{O}(2)$ *on* $\mathbb{C}^n \setminus \{0\}$ *is free it is also semi-regular. Indeed, from Proposition 2.8 all group orbits of points* $x \in \mathbb{C}^n \setminus \{0\}$ *are* 1*-dimensional.*

The group orbits of an effective and regular or semi-regular action of a Lie group Γ on a manifold $\mathcal{M}$ form a foliation of $\mathcal{M}$.

2.2 Symmetries of solutions

In the preceding section we concentrated on symmetries of the space on which a group acts. Solutions of a differential equation do not necessarily have the full symmetry group Γ of the differential equation. The discussion flows better if we start from the simplest solutions, equilibria, and then consider more complicated solutions.

2.2.1 Equilibria

An equilibrium with full symmetry lies in $\mathrm{Fix}\,(\Gamma)$, the orbit type is $\mathbf{1}$ and thus the multiplicity of the solution is one. Note that if $\dim \mathrm{Fix}\,(\Gamma) = 0$, since fixed-point subspaces are flow invariant, the solution has to be an equilibrium.

An equilibrium x with isotropy subgroup $\Sigma_x \subsetneq \Gamma$ has less than full symmetry. According to Proposition 2.8 this equilibrium with orbit type Γ/Σ_x does not come alone. If Γ is finite there are $|\Gamma|/|\Sigma_x|$ equilibria in the group orbit of Γ. If Γ is continuous then there is a, possibly disconnected, manifold of equilibria of dimension $\dim \Gamma - \dim \Sigma_x$ passing through x.

2.2.2 Periodic orbits

Let x_p be a periodic orbit of (6) with period T_p. Then, by equivariance, γx_p is another periodic orbit, for any $\gamma \in \Gamma$. From uniqueness of solutions x_p and γx_p are either identical or disjoined.

If they are identical we must have,

$$\gamma x_p(t+\theta) = x_p(t) \tag{25}$$

for some $\theta \in S^1 = [0, T]$. In Golubitsky and Stewart [40] $(\gamma, \theta) \in \Gamma \times S^1$ is called a *spatio-temporal symmetry* of the solution x_p. Spatio-temporal symmetries for which $\theta = 0$ are called *spatial* symmetries. The term spatial and spatio-temporal should not be confused with the terms used in the context of PDEs, here spatial refers to phase space. See Golubitsky and Stewart [40] for more details.

If the periodic solutions are disjoint their multiplicity (if Γ is finite), or the dimension of the manifold swept under the group action (if Γ is continuous) can be determined by application of Proposition 2.8 for any periodic point.

2.2.3 Relative equilibria

Let Γ be compact. A group orbit of a point x that is flow invariant is called a relative equilibrium. That is, there is dynamics only in the direction of the group action and in a frame moving along the group orbit with velocity given by the right hand side of (6) the relative equilibrium appears as an equilibrium. Alternatively we may view a relative equilibrium as a group invariant periodic orbit, satisfying

$$x(t) = \gamma_t x_0 \tag{26}$$

for a curve $\gamma_t \in \Gamma$.

Relative equilibria are a hallmark of systems with continuous symmetry. Unless a discrete subgroup enforces it, there is no reason we should expect not to have dynamics in the direction of group action and we expect to have relative equilibria. For the connection of this statement to the genericity of bifurcations with continuous symmetry see ref. [40].

2.2.4 Relative periodic orbits

For Γ compact, a relative periodic orbit is a trajectory satisfying the condition

$$x(t+T) = \gamma x(t)\,, \tag{27}$$

for all t and for some group element $\gamma \in \Gamma$ and period T. In ref. [56], Krupa proves that the closure of a relative periodic orbit is a torus and provides a bound for its dimension. Another way to view relative periodic orbits is as periodic orbits of the reduced dynamics, see Sect. 2.3 bellow. Therefore, unless there is a reason that enforces $v(t)$ in (6) to be orthogonal to the direction of the group action, one expects to find relative periodic orbits in systems with continuous symmetry for the same reasons one expects periodic orbits in generic dynamical systems with discrete or no symmetry.

2.3 Symmetry reduction

The purpose of symmetry reduction in differential equations is to project the dynamics to a space in which the symmetry group G acts trivially. Such a space is called *orbit space* because each group orbit of a point in original space is mapped to a single point in orbit space, or *quotient space* because the symmetry has been "divided out" or simply *reduced space*. If the original space is a manifold $\mathcal{M}$ it is then customary to write the quotient space as $\mathcal{M}/\Gamma$. The resulting dynamical system is called *image* of the original.

The stratification of $\mathcal{M}$ induced by the group action is carried over to the quotient space with each disconnected set in a stratum mapped to the same manifold in quotient space. Yet, a fundamental problem with symmetry reduction is that the orbit space is in general not a manifold. Unless the action of the group is free, group orbits do not have the same dimension and different strata are mapped to manifolds of different dimension. We will see this property of quotient space manifest itself in different ways depending on the reduction method but always introducing some singularity even though there is nothing singular about $\mathcal{M}$ or the flow of the dynamical system on it.

2.3.1 Hilbert basis approach

The most common approach to symmetry reduction is through the use of a Hilbert basis of invariant polynomials. One computes a (non-unique) basis of linearly independent polynomials, invariant under the action of the symmetry group (*cf.* ref. [35] for a discussion of methods) and either rewrites the dynamics in this basis or maps the solutions to the polynomials. We will describe how this approach works for the example of Complex Lorenz equations in Sect. 4.1. The reader is referred to the book of Gilmore and Lettelier [39] for a very detailed discussion of symmetry reduction. For the action (18) of SO(2) on $\mathbb{R}^5$ a Hilbert basis [39] is

$$\begin{aligned} u_1 &= x_1^2 + x_2^2 \,, \\ u_2 &= y_1^2 + y_2^2 \,, \\ u_3 &= x_1 y_2 - x_2 y_1 \,, \\ u_4 &= x_1 y_1 + x_2 y_2 \,, \\ u_5 &= z \,. \end{aligned} \tag{28}$$

The polynomials in a Hilbert basis are linearly independent, but functionally dependent through relation called *syzygies*. For polynomials (28) the syzygy is

$$u_1 u_2 - u_3^2 - u_4^2 = 0 \,. \tag{29}$$

When one takes syzygies into account in rewriting the dynamical system, singularities are introduced. Moreover when one *lifts* the dynamics from the quotient space $\mathcal{M}/G$ to the original space $\mathcal{M}$ the transformations have singularities at the fixed-point subspaces of the isotropy subgroups in $\mathcal{M}$, in the optimal case, *cf.* ref. [39]. Those singularities do not seem to restrict our ability to use invariant polynomials to obtain symmetry reduced projections of the dynamics as we will see in Chapter 4.

What restricts the utility of Hilbert basis methods is that the determination of a Hilbert basis becomes computationally prohibitive as the dimension of the system or of the group increases [35; 13] and typically computations are constrained to dimension smaller than ten. As our goal is to quotient continuous symmetries of high-dimensional flows, specifically those arising from truncations of the Kuramoto-Sivashinsky and Navier-Stokes flows and thus we need an efficient framework.

2.3.2 Moving frames

In this section we present the method of moving frames of Cartan [8] in the formulation of Fels and Olver [28; 29], also *cf.* ref. [70] for a pedagogical exposition and the proofs of theorems listed here. Its purpose is to generate functionally independent invariants for the

action of a group Γ on a manifold $\mathcal{M}$ under certain assumptions, and is not restricted to reduction problems.

In the following let Γ be r-dimensional and act on a n-dimensional manifold $\mathcal{M}$.

Definition 2.27 *A moving frame is a smooth Γ-equivariant mapping $\rho : \mathcal{M} \to \Gamma$.*

One distinguishes between left moving frames for which the equivariance condition is $\rho(\gamma x) = \gamma\rho(x)\,,\ x \in \mathcal{M}\,,\ \gamma \in \Gamma$ and right moving frames for which the equivariance condition is $\rho(\gamma x) = \rho(x)\gamma^{-1}\,,\ x \in \mathcal{M}\,,\ \gamma \in \Gamma$.

The following existence theorem for moving frames will be very important.

Theorem 2.28 *A moving frame exists in a neighborhood of a point $x \in \mathcal{M}$ if and only if Γ acts freely and regularly near x.*

For groups acting regularly we can define a slice for the group orbits.

Proposition 2.29 *Let Γ act regularly on a n-dimensional manifold $\mathcal{M}$ with r-dimensional orbits. Define a (local)* slice *to be an $(n-r)$-dimensional submanifold K of $\mathcal{M}$ such that K intersects each orbit transversally and at most once. If a Lie group Γ acts regularly on a manifold $\mathcal{M}$, then one can construct a local slice passing through any point $x \in \mathcal{M}$.*

Theorem 2.30 *Assume the conditions of Proposition 2.29 hold and let $K \subset \mathcal{M}$ be a slice. For $x \in \mathcal{M}$, let $\gamma = \rho(x)$ be the unique group element that maps x to the slice: $gx = \rho(x)x \in K$. Then $\rho : \mathcal{M} \to \Gamma$ is a right moving frame.*

A slice K can be defined by means of level sets of functions $K_i(x) = c_i$, where $x \in V$ and $i = 1, \ldots, r$. If the $K_i(x)$ coincide with the local coordinates x_i on the manifold V, i.e. $K_i(x) = x_i$, then we call K a *coordinate slice*.

Example 2.31 *Consider the standard action of* SO(2) *on* $\mathbb{R}^2$*:*

$$(x, y) \mapsto (x\cos\theta - y\sin\theta,\ x\sin\theta + y\cos\theta) \tag{30}$$

which is regular on $\mathbb{R}^2\backslash\{0\}$. Thus we can define a slice by, for instance, the positive y axis: $x = 0$, $y > 0$. We can now construct a moving frame as follows. We write out explicitly the group transformations:

$$\overline{x} = x\cos\theta - y\sin\theta\,, \tag{31a}$$

$$\overline{y} = x\sin\theta + y\cos\theta\,. \tag{31b}$$

Then set $\overline{x} = 0$ and solve (31a) for the group parameter to obtain the moving frame

$$\theta = \tan^{-1}\frac{x}{y} \tag{32}$$

which brings any point back to the slice.[1] *Substituting (32) in the remaining equation, we get the* SO(2)*-invariant expression*

$$\overline{y} = \sqrt{x^2 + y^2}\,. \tag{33}$$

[1] *Implementation note: Here it is important that* $\tan^{-1}$ *distinguishes quadrants on the (x, y) plane so that we get the correct geometric operation.*

The above *normalization* procedure for the computation of invariants applied in the example of SO(2) can be applied in much more general situations as follows. Assume Γ acts (locally) freely on $\mathcal{M}$ and thus Γ-orbits have the same dimension, say r, as Γ. Choose a coordinate slice $K = \{x_1 = c_1, \ldots, x_r = c_r\}$ defined by the first r coordinates (relabel coordinates as necessary). Introduce local coordinates $g = (g_1, \ldots, g_r)$ on Γ in the neighborhood of the identity. The group transformations are

$$\overline{x} = g \cdot x = w(g, x)\,. \tag{34}$$

Equating the first r components of the function w to the constants in the definition of the slice $K_i(x) = c_i$ yields the *normalization equations* for K:

$$\overline{x}_1 = w_1(g, x) = c_1, \ldots, \overline{x}_r = w_r(g, x) = c_r\,. \tag{35}$$

From the definition of slice and the Implicit Function Theorem the normalization equations (35) can always be solved for the group parameters in terms of x, yielding the moving frame associated with K: $g = \gamma(x)$. Substitution of the moving frame equation back in (34) will yield the $n - r$ *fundamental invariants*, in the sense that any other invariant can be expressed as a function of $\overline{x}_{r+1} \ldots \overline{x}_n$ and they are functionally independent. Thus they serve to distinguish orbits in the neighborhood of the slice, i.e. two points lie on the same group orbit if and only if all the fundamental invariants agree. For proof *cf.* refs. [28; 29].

CHAPTER III

DESYMMETRIZATON OF LORENZ EQUATIONS

This chapter is based on a series of examples developed for ChaosBook.org [20], in collaboration with Jonathan Halcrow and Predrag Cvitanović. Its intent is pedagogical: as a warmup to Kuramoto-Sivashinsky equation, which has both discrete and continuous symmetries, we carry out a *discrete* symmetry reduction of the 3-dimensional Lorenz flow, and illustrate in the process some of the key ideas in a rather simple setting.

We start with the full phase space and end with what the ultimate goal would be for the (yet unattained) Kuramoto-Sivashinsky and Navier-Stokes symmetry reductions, a 1-dimensional return map description of the dynamics. We explain why Lorenz equilibria are heteroclinically connected (it is not due to the symmetry), and how to generate all periodic orbits of Lorenz flow up to given length. This we do, in contrast to the rest of the thesis, without any group-theoretical jargon.

Even though no dynamical system has been studied more exhaustively than the Lorenz equations, this analysis is new. The desymmetrization follows Gilmore and Lettelier [39], but the key new idea is taken from Christiansen *et al.* [14]: the arc-length parametrization of the unstable manifold maintains the 1-to-1 relation of the *full* d-dimensional phase space dynamics and its 1-dimensional return-map representation, in contrast to 1-dimensional *projections* of the $(d-1)$-dimensional Poincaré section return maps previously deployed in the literature. In other words, to high accuracy *no information about the flow is lost* by its 1-dimensional return map description.

3.1 Lorenz strange attractor

Edward Lorenz arrived at the equation

$$\dot{x} = v(x) = \begin{bmatrix} \dot{x} \\ \dot{y} \\ \dot{z} \end{bmatrix} = \begin{bmatrix} \sigma(y-x) \\ \rho x - y - xz \\ xy - bz \end{bmatrix} \tag{36}$$

by a drastic simplification of the Rayleigh-Benard flow. Lorenz fixed $\sigma = 10$, $b = 8/3$, and varied the "Rayleigh number" ρ. For $0 < \rho < 1$ the equilibrium $\mathrm{E}_0 = (0,0,0)$ at the origin is attractive. At $\rho = 1$ it undergoes a pitchfork bifurcation into a pair of equilibria at

$$x_{\mathrm{E}_{1,2}} = (\pm\sqrt{b(\rho-1)}, \pm\sqrt{b(\rho-1)}, \rho-1)\,, \tag{37}$$

We shall not explore the Lorenz flow dependence on the ρ parameter in what follows, but here is a brief synopsis: the E_0 1–d unstable manifold closes into a homoclinic orbit at $\rho = 13.56\ldots$. Beyond that, an infinity of associated periodic orbits are generated, until $\rho = 24.74\ldots$, where $\mathrm{E}_{1,2}$ undergo a Hopf bifurcation.

All computations that follow will be performed for the Lorenz parameter choice $\sigma = 10, b = 8/3, \rho = 28$. For these parameter values the long-time dynamics is confined to the strange attractor depicted in Figure 4.

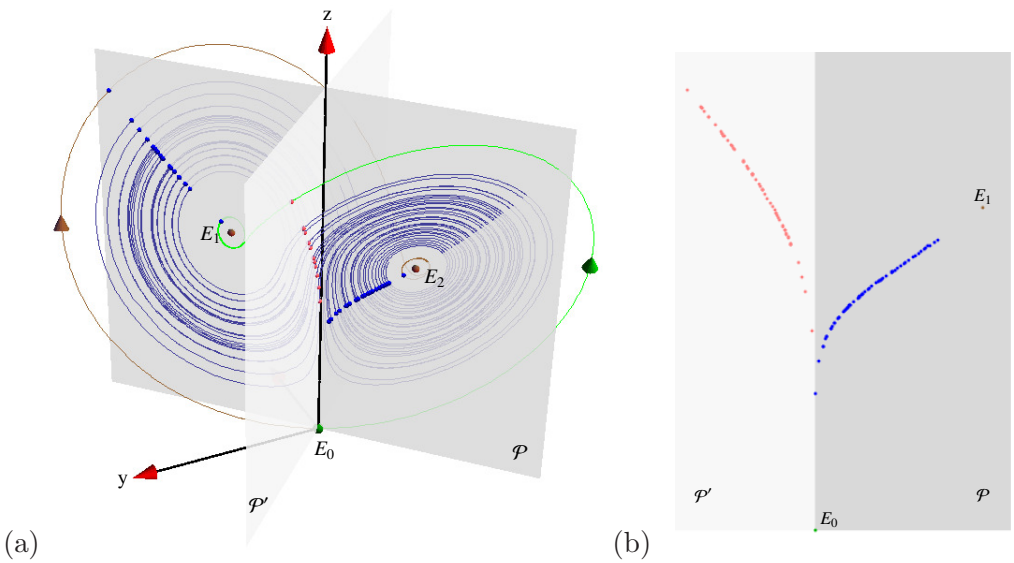

(a) (b)

Figure 4: (a) Lorenz flow cut by $y = x$ Poincaré section plane $\mathcal{P}$ through the z axis and both $\mathrm{E}_{1,2}$ equilibria. Points where flow pierces into section are marked by dots. To aid visualization of the flow near the E_0 equilibrium, the flow is cut by the second Poincaré section, $\mathcal{P}'$, through $y = -x$ and the z axis. (b) Poincaré sections $\mathcal{P}$ and $\mathcal{P}'$ laid side-by-side. The singular nature of these sections close to E_0 will be elucidated in Sect. 3.2.1 and Figure 7 (b).

3.2 Sections of Lorenz flow

The plane $\mathcal{P}$ fixed by the $x = y$ diagonal and the z-axis depicted in Figure 4 is a natural choice of a Poincaré section of the Lorenz flow, as it contains all three equilibria, $x_{\mathrm{E}_0} = (0, 0, 0)$ and the (37) pair $\mathrm{E}_{1,2}$. A section has to be supplemented with an orientation condition: here points where flow pierces *into* the section are marked by dots.

$\mathrm{E}_{1,2}$ are centers of out-spirals, and close to them the section is transverse to the flow. However, close to E_0 trajectories pass the z-axis either by crossing the section $\mathcal{P}$ or staying on the viewer's side. We are free to deploy as many sections as we wish: in order to capture the whole flow in this neighborhood we add the second Poincaré section, $\mathcal{P}'$, through the $y = -x$ diagonal and the z-axis. Together the two sections, Figure 4 (b), capture the whole flow near E_0. The dynamics on the sections appear very singular. We explain this singularity in Sect. 3.2.1, and postpone construction of a Poincaré return map to Sect. 3.4.

3.2.1 Stability of Lorenz flow equilibria

For the Lorenz flow (36) the stability matrix is

$$A_{Lor} = \begin{pmatrix} -\sigma & \sigma & 0 \\ \rho - z & -1 & x \\ y & x & -b \end{pmatrix} . \tag{38}$$

A glance at Figure 4 suggests that the flow is organized by its 3 equilibria, so let's have a closer look at their stable/unstable manifolds.

The E_0 equilibrium stability matrix (38) evaluated at $x_{\mathrm{E}_0} = (0, 0, 0)$ is block-diagonal. The z-axis is an eigenvector with a contracting eigenvalue $\lambda^{(2)} = -b$. From (44) it follows

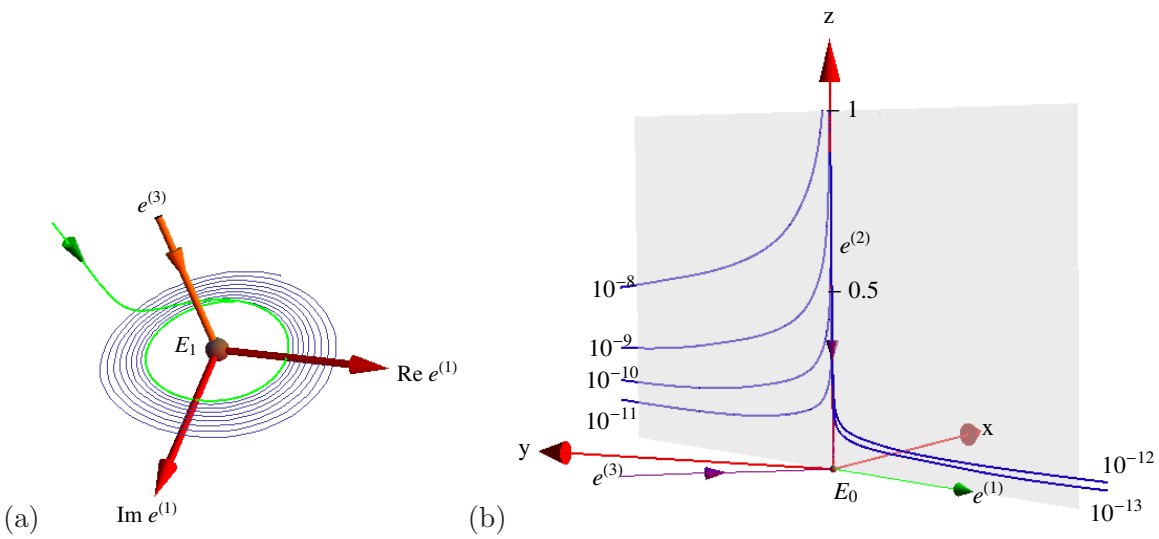

Figure 5: (a) Blow-up of the linearized Lorenz flow near E_1 equilibrium, see Figure 4 (a). The unstable eigenplane of E_1 is spanned by $\mathrm{Re}\,\mathbf{e}^{(1)}$ and $\mathrm{Im}\,\mathbf{e}^{(1)}$. The stable eigenvector $\mathbf{e}^{(3)}$. The descent of the E_0 unstable manifold (green) defines the innermost edge of the strange attractor. As it is clear from Figure 6 (a), it also defines its outermost edge. (b) Lorenz flow near the E_0 equilibrium: unstable eigenvector $\mathbf{e}^{(1)}$, stable eigenvectors $\mathbf{e}^{(2)}$, $\mathbf{e}^{(3)}$. Trajectories initiated at distances $10^{-8}\cdots 10^{-12}$, 10^{-13} away from the z-axis exit finite distance from E_0 along the $(\mathbf{e}^{(1)},\mathbf{e}^{(2)})$ eigenvectors plane. Due to the strong $\lambda^{(1)}$ expansion, the E_0 equilibrium is, for all practical purposes, unreachable, and the $\mathrm{E}_1 \to \mathrm{E}_0$ heteroclinic connection never observed in simulations such as Figure 4.

that all $[x,y]$ areas shrink at rate $-(\sigma+1)$. Indeed, the $[x,y]$ submatrix

$$A^- = \begin{pmatrix} -\sigma & \sigma \\ \rho & -1 \end{pmatrix} \tag{39}$$

has a real expanding/contracting eigenvalue pair $\lambda^{(1,3)} = -(\sigma+1)/2 \pm \sqrt{(\sigma-1)^2/4+\rho\sigma}$, with the right eigenvectors $\mathbf{e}^{(1)}$, $\mathbf{e}^{(3)}$ in the $[x,y]$ plane, given by (either) column of the projection operator

$$\mathbf{P}_i = \frac{A^- - \lambda^{(j)}\mathbf{1}}{\lambda^{(i)}-\lambda^{(j)}} = \frac{1}{\lambda^{(i)}-\lambda^{(j)}} \begin{pmatrix} -\sigma-\lambda^{(j)} & \sigma \\ \rho & -1-\lambda^{(j)} \end{pmatrix}, \qquad i \neq j \in \{1,3\}\,. \tag{40}$$

$\mathrm{E}_{1,2}$ equilibria have no symmetry, so their eigenvalues are given by the roots of a cubic equation, the secular determinant $\det(A-\lambda\mathbf{1})=0$:

$$\lambda^3 + \lambda^2(\sigma+b+1) + \lambda b(\sigma+\rho) + 2\sigma b(\rho-1) = 0\,. \tag{41}$$

For $\rho > 24.74$, $\mathrm{E}_{1,2}$ have one stable real eigenvalue and one unstable complex conjugate pair, leading to a spiral-out instability and the strange attractor depicted in Figure 4.

As all numerical plots of the Lorenz flow are here carried out for the Lorenz parameter choice $\sigma = 10, b = 8/3, \rho = 28$, we note the values of these eigenvalues for future reference,

$$\begin{array}{lrcl} \mathrm{E}_0: & (\lambda^{(1)},\lambda^{(2)},\lambda^{(3)}) & = & (\,11.83\,,\ -2.666,\ -22.83\,) \\ \mathrm{E}_1: & (\mu^{(1)} \pm i\,\omega^{(1)},\lambda^{(3)}) & = & (\,0.094 \pm i\,10.19,\ -13.85\,), \end{array} \tag{42}$$

as well as the rotation period $T_{\rm E_1} = 2\pi/\omega^{(1)}$ about $\rm E_1$, and the associated expansion/contraction multipliers $\Lambda^{(i)} = \exp(\mu^{(j)} T_{\rm E_1})$ per spiral-out turn:

$$T_{\rm E_1} = 0.6163\,, \qquad (\Lambda^{(1)}, \Lambda^{(3)}) = (\,1.060\,, 1.957 \times 10^{-4}\,)\,. \tag{43}$$

We learn that the typical turnover time scale in this problem is of order $T \approx T_{\rm E_1} \approx 1$ (and not, let us say, 1000, or 10^{-2}). Combined with the contraction rate (44), this tells us that the Lorenz flow strongly contracts phase space volumes, by factor of $\approx 10^{-4}$ per mean turnover time.

In the $\rm E_1$ neighborhood the unstable manifold trajectories slowly spiral out, with very small radial per-turn expansion multiplier $\Lambda^{(1)} \simeq 1.06$, and very strong contraction multiplier $\Lambda^{(3)} \simeq 10^{-4}$ onto the unstable manifold, Figure 5 (a). This contraction confines, for all practical purposes, the Lorenz attractor to a 2–*d* surface evident in the section Figure 4.

In the $x_{\rm E_0} = (0,0,0)$ equilibrium neighborhood the extremely strong $\lambda^{(3)} \simeq -23$ contraction along the $\mathbf{e}^{(3)}$ direction confines the hyperbolic dynamics near $\rm E_0$ to the plane spanned by the unstable eigenvector $\mathbf{e}^{(1)}$, with $\lambda^{(1)} \simeq 12$, and the slowest contraction rate eigenvector $\mathbf{e}^{(2)}$ along the z-axis, with $\lambda^{(2)} \simeq -3$. In this plane the strong expansion along $\mathbf{e}^{(1)}$ overwhelms the slow $\lambda^{(2)} \simeq -3$ contraction down the z-axis, making it extremely unlikely for a random trajectory to approach $\rm E_0$, Figure 5 (b). Thus linearization suffices to describe analytically the singular dip in the Poincaré sections of Figure 4, and the empirical scarcity of trajectories close to $\rm E_0$.

3.3 Lorenz flow: Global portrait

As the $\rm E_1$ unstable manifold spirals out, the strip that starts out in the section above $\rm E_1$ in Figure 4 cuts across the z-axis invariant subspace. This strip necessarily contains a heteroclinic orbit that hits the z-axis head on, and in infinite time (but exponentially fast) descends all the way to $\rm E_0$.

As in the neighborhood of the $\rm E_0$ equilibrium the dynamics is linear (see Figure 5 (a)), there is no need to integrate numerically the final segment of the heteroclinic connection - it is sufficient to bring a trajectory a small distance away from $\rm E_0$, continue analytically to a small distance beyond $\rm E_0$, then resume the numerical integration.

What happens next? Trajectories to the left of z-axis shoot off along the $\mathbf{e}^{(1)}$ direction, and those to the right along $-\mathbf{e}^{(1)}$. As along the $\mathbf{e}^{(1)}$ direction $xy > 0$, the nonlinear term in the $\dot{z}$ equation (36) bends both branches of the $\rm E_0$ unstable manifold $W^u(\rm E_0)$ upwards. Then ... - never mind. Best to postpone the completion of this narrative to Sect. 3.4, where the discrete symmetry of Lorenz flow will help us streamline the analysis. As we shall show, what we already know about the 3 equilibria and their stable/unstable manifolds suffices to completely pin down the topology of Lorenz flow.

3.3.1 Lorenz flow phase space contraction

The Lorenz flow is volume contracting,

$$\partial_i v_i = \sum_{i=1}^{3} \lambda^{(i)}(x,t) = -\sigma - b - 1\,, \tag{44}$$

at a constant, coordinate- and ρ-independent rate, set by Lorenz to $\partial_i v_i = -13.66$. As for periodic orbits and for long time averages there is no contraction/expansion along the flow,

$\lambda^{(\|)} = 0$, and the sum of $\lambda^{(i)}$ is constant by (44), there is only one independent exponent $\lambda^{(i)}$ to compute.

3.4 *Desymmetrization of the Lorenz flow*

The vector field in Lorenz equations (36) is equivariant under the action of cyclic group $\mathrm{D}_1 = \{e, R(1/2)\}$ acting on $\mathbb{R}^3$ by a π rotation about the z axis,

$$R(1/2)(x, y, z) = (-x, -y, z)\,.$$

Lorenz equation (36) is invariant under the action of order-2 group $\mathrm{D}_1 = \{e, R(1/2)\}$, where $R(1/2)$ is $[x, y]$-plane, constant z rotation by π about the z-axis:

$$(x, y, z) \to R(1/2)(x, y, z) = (-x, -y, z)\,. \tag{45}$$

$(R(1/2))^2 = 1$ condition decomposes the phase space into two linearly irreducible subspaces $\mathcal{M} = \mathcal{M}^+ \oplus \mathcal{M}^-$, the z-axis $\mathcal{M}^+$ and the $[x, y]$ plane $\mathcal{M}^-$, with projection operators onto the two subspaces given by

$$\mathbf{P}^+ = \frac{1}{2}(1 + R(1/2)) = \begin{pmatrix} 0 & 0 & 0 \\ 0 & 0 & 0 \\ 0 & 0 & 1 \end{pmatrix}, \quad \mathbf{P}^- = \frac{1}{2}(1 - R(1/2)) = \begin{pmatrix} 1 & 0 & 0 \\ 0 & 1 & 0 \\ 0 & 0 & 0 \end{pmatrix}. \tag{46}$$

As the flow is D_1-invariant, so is its linearization $\dot{x} = Ax$. Evaluated at E_0, A commutes with $R(1/2)$, and, as we have already seen in Sect. 3.2.1, the E_0 stability matrix decomposes into $[x, y]$ and z blocks.

The 1–d $\mathcal{M}^+$ subspace is the fixed-point subspace of D_1, with the z-axis points left *point-wise* invariant under the group action

$$\mathrm{Fix}(\mathrm{D}_1) = \{x \in \mathcal{M}^+ : \mathbf{g}\, x = x \text{ for } g \in \{e, R(1/2)\}\}\,. \tag{47}$$

However, a point $x(t)$ in $\mathrm{Fix}(\mathrm{D}_1)$ moves with time, but remains within $x(t) \subseteq \mathrm{Fix}(\mathrm{D}_1)$ for all times; the subspace $\mathcal{M}^+ = \mathrm{Fix}(\mathrm{D}_1)$ is *flow invariant*. In case at hand this jargon is a bit of an overkill: clearly for $(x, y) = (0, 0)$ the full phase space Lorenz equation (36) is reduced to the exponential contraction to the E_0 equilibrium,

$$\dot{z} = -b\, z\,. \tag{48}$$

However, for flows in higher-dimensional phase spaces the flow-invariant $\mathcal{M}^+$ subspace can itself be high-dimensional, with interesting dynamics of its own. Even in this simple case this subspace plays an important role as a topological obstruction, with the number of winds of a trajectory around it providing a natural symbolic dynamics.

The $\mathcal{M}^-$ subspace is, however, *not* flow-invariant, as the nonlinear terms $\dot{z} = xy - bz$ in the Lorenz equation (36) send all initial conditions within $\mathcal{M}^- = (x(0), y(0), 0)$ into the full, $z(t) \neq 0$ phase space $\mathcal{M}$. The $R(1/2)$ symmetry is nevertheless very useful.

By taking as a Poincaré section any $R(1/2)$-invariant, infinite-extent, non-self-intersecting surface that contains the z axis, the phase space is divided into a half-space fundamental domain $\tilde{\mathcal{M}} = \mathcal{M}/\mathrm{D}_1$ and its 180^o rotation $R(1/2)\tilde{\mathcal{M}}$. An example is afforded by the $\mathcal{P}$ plane section of the Lorenz flow in Figure 4. Take the fundamental domain $\tilde{\mathcal{M}}$ to be the half-space

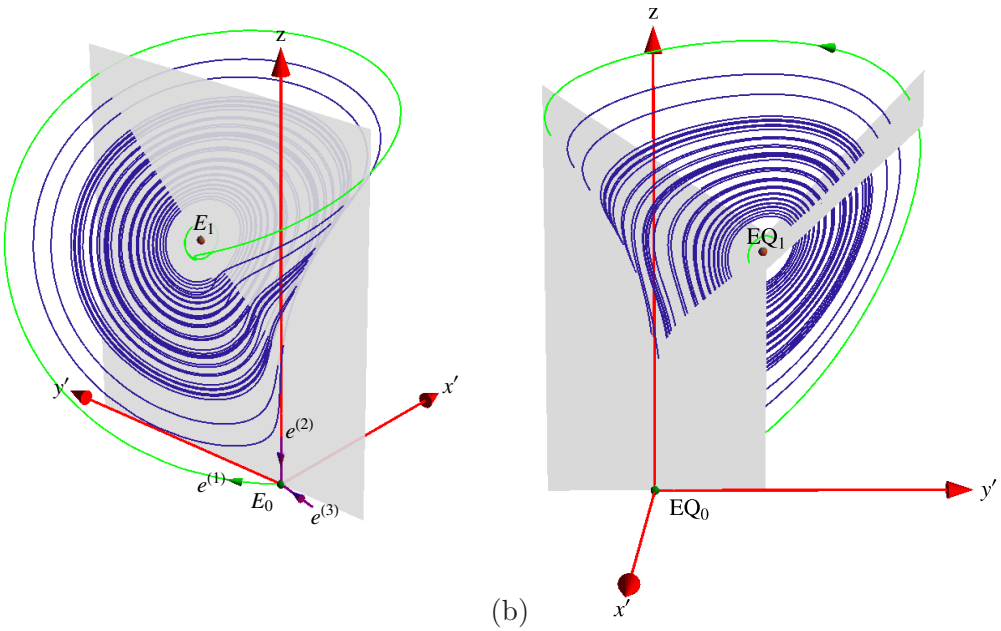

(a) (b)

Figure 6: Two views of the Lorenz attractor plotted in $[x', y', z]$, the doubled-polar angle coordinates (49), with points related by π-rotation in the $[x, y]$ plane identified. Stable eigenvectors of E_0: $\mathbf{e}^{(3)}$ and $\mathbf{e}^{(2)}$, along the z axis (48). Unstable manifold orbit $W^u(\mathrm{E}_0)$ (green) is a continuation of the unstable $\mathbf{e}^{(1)}$ of E_0.

between the viewer and $\mathcal{P}$. Then the full Lorenz flow is captured by re-injecting back into $\tilde{\mathcal{M}}$ any trajectory that exits it, by a rotation of π around the z axis.

As any such $R(1/2)$-invariant section does the job, a choice of a 'fundamental domain' is here largely mater of taste. For purposes of visualization it is convenient to make the double-cover nature of the full phase space by $\tilde{\mathcal{M}}$ explicit, through any phase space redefinition that maps a pair of points related by symmetry into a single point. In case at hand, this can be easily accomplished by expressing (x, y) in polar coordinates $(x, y) = (r\cos\theta, r\sin\theta)$, and then plotting the flow in the *'doubled-polar angle representation:'*

$$(x', y') = (r\cos 2\theta, r\sin 2\theta) = ((x^2 - y^2)/r, 2xy/r)\,, \tag{49}$$

as in Figure 6 (a). In contrast to the original D_1-equivariant coordinates $[x, y, z]$, the Lorenz flow expressed in the new coordinates $[x', y', z]$ is D_1-*invariant*, see Sect. 2.3. In this representation the $\tilde{\mathcal{M}} = \mathcal{M}/\mathrm{D}_1$ fundamental domain flow is a smooth, continuous flow, with (any choice of) the fundamental domain stretched out to seamlessly cover the entire $[x', y']$ plane.

We emphasize: such nonlinear coordinate transformations are *not* required to implement the symmetry quotienting $\mathcal{M}/\mathrm{D}_1$, unless there are computational gains in a nonlinear coordinate change suggested by the symmetry. We offer them here only as a visualization aid that might help the reader disentangle 2–d projections of higher-dimensional flows. All numerical calculations are usually carried in the initial, full phase space formulation of a flow, with symmetry-related points identified by *linear* symmetry transformations.

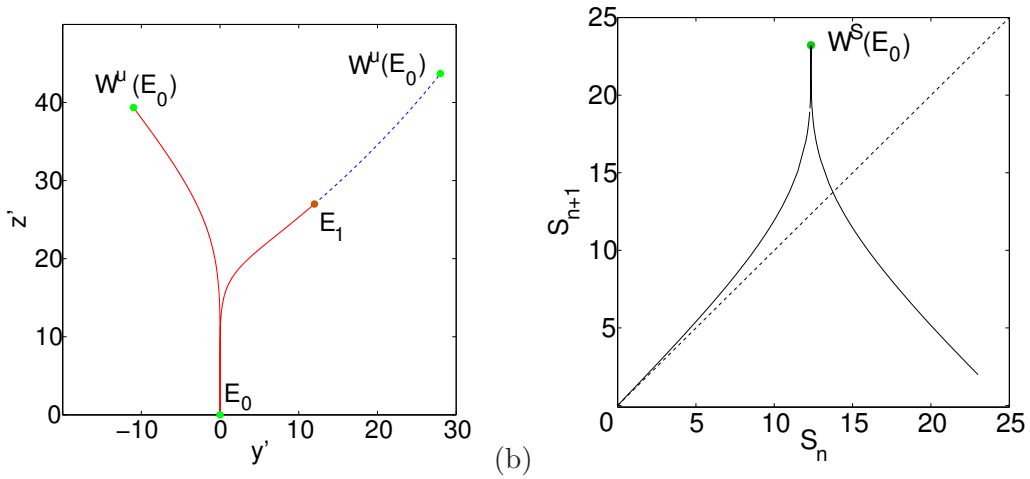

Figure 7: A Poincaré section of the Lorenz flow in the doubled-polar angle representation, Figure 6, given by the $[y', z]$ plane that contains the z-axis and the equilibrium E_1. x' axis points toward the viewer. (a) The Poincaré section of the Lorenz flow by the section plane; compare with Figure 4. Crossings *into* the section are marked red (solid) and crossings *out of* the section are marked blue (dashed). Outermost points of both in- and out-sections are given by the E_0 unstable manifold $W^u(\mathrm{E}_0)$ intersections. (b) The Poincaré return map $s_{n+1} = P(s_n)$ parameterized by Euclidean arclength s measured along the E_1 unstable manifold, from x_{E_1} to $W^u(\mathrm{E}_0)$ section point, uppermost right point of the blue segment in Figure 7 (b). The critical point (the 'crease') of the map is given by the section of the heteroclinic orbit $W^s(\mathrm{E}_0)$ that descends all the way to E_0, in infinite time and with infinite slope.

3.5 Periodic orbits of Lorenz flow

The relation between the full phase space periodic orbits, and the fundamental domain (49) reduced orbits of the Lorenz flow: Full phase space cycle pairs p, Rp map into a single cycle $\tilde{p}$ in the fundamental domain, and any self-dual cycle $p = Rp = \tilde{p}R\tilde{p}$ is a repeat of a $\tilde{p}$.

In this chapter we use Lorenz flows to motivate modeling of higher-dimensional flows by iteration of 1-dimensional maps. For these two flows the 1-dimensional maps capture essentially all of the higher-dimensional flow dynamics, both qualitatively and quantitatively. 1-dimensional maps suffice to explain the two key aspects of qualitative dynamics; *temporal ordering*, or *itinerary* with which a trajectory visits phase space regions, and the *spatial ordering* between trajectory points, which is the key to determining the admissibility of an orbit with a prescribed itinerary. In a generic dynamical system not every symbol sequence is realized as a dynamical trajectory; as one looks further and further, one discovers more and more rules which prohibit families of itineraries. For 1-dimensional "stretch & fold" maps the *kneading theory* provides the definitive answer as to which temporal itineraries are *admissible* as trajectories of the dynamical system.

3.6 Lorenz flow: Stretch & crease

We now deploy the symmetry of Lorenz flow to streamline and complete analysis of the Lorenz strange attractor commenced in Sect. 3.4. There we showed that the dihedral $D_1 = \{e, R\}$ symmetry identifies the two equilibria E_1 and E_2, and the traditional 'two-eared' Lorenz flow Figure 4 is replaced by the 'single-eared' flow of Figure 6. Furthermore,

symmetry identifies two sides of any plane through the z axis, replacing a full-space Poincaré section plane by a half-plane, and the two directions of a full-space eigenvector of E_0 by a one-sided eigenvector, see Figure 6 (a).

Example 3.3 explained the genesis of the x_{E_1} equilibrium unstable manifold, its orientation and thickness, its collision with the z-axis, and its heteroclinic connection to the $x_{E_0} = (0, 0, 0)$ equilibrium. All that remains is to describe how the E_0 neighborhood connects back to the E_1 unstable manifold. Figure 6 now shows clearly how the Lorenz dynamics is pieced together from the 2 equilibria and their unstable manifolds:

Having completed the descent to E_0, the infinitesimal neighborhood of the heteroclinic $E_1 \to E_0$ trajectory is ejected along the unstable manifold of E_0 and is re-injected into the unstable manifold of E_1. Both sides of the narrow strip enclosing the E_0 unstable manifold lie above it, and they get folded onto each other with a knife-edge crease (contracted exponentially for infinite time to the E_0 heteroclinic point), with the heteroclinic out-trajectory defining the outer edge of the strange attractor. This leads to the folding of the outer branch of the Lorenz strange attractor, illustrated in Figure 7 (b), with the outermost edge following the unstable manifold of E_0.

Now the stage is set for construction of Poincaré sections and associated Poincaré return maps. There are two natural choices; the section at E_0, lower part of Figure 7 (a), and the section (blue) above E_1. The first section, together with the blowup of the E_0 neighborhood, Figure 5 (b), illustrates clearly the scarcity of trajectories (vanishing natural measure) in the neighborhood of E_0. The flat section above E_1 (which is a smooth conjugacy by the flow of the knife-sharp section at E_0) is more convenient for our purposes. Its return map is given by Figure 7 (b).

The rest is straight sailing: to accuracy 10^{-4} the return map is unimodal, its critical point's forward trajectory yields the kneading sequence, and the admissible binary sequences, so any number of periodic points can be accurately determined from this 1-dimensional return map, and the 3–d cycles then verified by integrating the Lorenz differential equations (36), or further refined.

What have we learned from the the Lorenz 3-dimensional flow? If a flow is locally unstable but globally bounded, any open ball of initial points will be stretched out and then folded back. If the equilibria are hyperbolic, the trajectories will be attracted along some eigendirections and ejected along others. Hence qualitatively a typical trajectory will wander through phase space, being alternatively attracted into equilibria neighborhoods, and then ejected again. What is important is the motion along the unstable manifolds –that is where 1-dimensional maps come from.

CHAPTER IV

DESYMMETRIZATON OF LASER EQUATIONS

4.1 Complex Lorenz equations

Complex Lorenz equations were introduced by Gibbon and McGuinness [37] as a low-dimensional model of baroclinic instability in the atmosphere. As the name suggests they turned out to be a complex generalization of Lorenz equations:

$$\begin{aligned} \dot{x} &= -\sigma x + \sigma y \,, \\ \dot{y} &= (r - z)x - a y \,, \\ \dot{z} &= \frac{1}{2}\,(x y^* + x^* y) - b z \,, \end{aligned} \tag{50}$$

where now x, y are complex variables, z is real, while the parameters σ, b are real and $r = r_1 + i r_2$, $a = 1 - ie$ are complex. Ning and Haken [69] have shown that equations isomorphic to Complex Lorenz equations also appear as a truncation of Maxwell-Bloch equations describing a single mode, detuned, ring laser, but the authors choose $e + r_2 = 0$ so that a detuned stationary solution exists. Bakasov and Abraham [3] criticize this choice as being "degenerate" and show that one can use Complex Lorenz equations with $r_2 = 0$ and $e \neq 0$ to describe detuned lasers. From our point of view the choice of Ning and Haken leads to non-generic bifurcations as we now explain.

Complex Lorenz flow is equivariant under the action (8) of SO(2). We rewrite the system in real variables $x = x_1 + i\,x_2\,,\ y = y_1 + i\,x_2$ as

$$\begin{aligned} \dot{x}_1 &= -\sigma x_1 + \sigma y_1 \,, \\ \dot{x}_2 &= -\sigma x_2 + \sigma y_2 \,, \\ \dot{y}_1 &= (r_1 - z)x_1 - r_2 x_2 - y_1 - e y_2 \,, \\ \dot{y}_2 &= r_2 x_1 + (r_1 - z)x_2 + e y_1 - y_2 \,, \\ \dot{z} &= -b z + x_1 y_1 + x_2 y_2 \,. \end{aligned} \tag{51}$$

The stability matrix is

$$A_{CLe} = \begin{pmatrix} -\sigma & 0 & \sigma & 0 & 0 \\ 0 & -\sigma & 0 & -\sigma & 0 \\ r_1 - z & -r_2 & -1 & -e & -x_1 \\ r_2 & r_1 - z & e & -1 & -x_2 \\ y_1 & y_2 & x_1 & x_2 & -b \end{pmatrix} . \tag{52}$$

The origin is an equilibrium of (51) for any value of the parameters. As shown in ref. [32] it is stable for $0 < r_1 < r_{1c}$ and unstable for $r_{1c} < r_1$, where

$$r_{1c} = 1 + \frac{(e + r_2)(e - \sigma r_2)}{(\sigma + 1)^2} \,. \tag{53}$$

At bifurcation a pair of eigenvalues crosses the imaginary axis with imaginary part:

$$\omega_c = \frac{\sigma(e + r_2)}{\sigma + 1} \,. \tag{54}$$

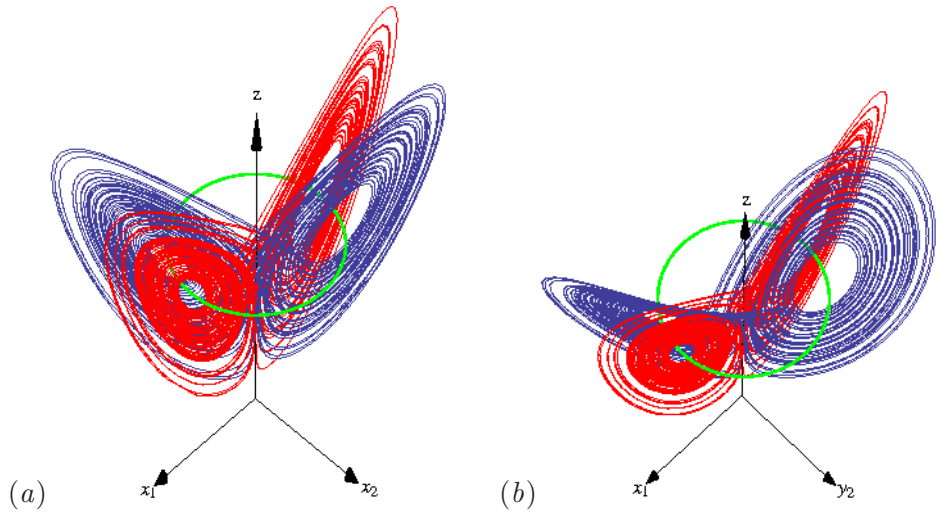

Figure 8: Two different projections of the Complex Lorenz equations dynamics (50) for $r_1 = 28$, $b = 8/3$, $\sigma = 10$, $a = 1$ and $e = r_2 = 0$. The dynamics in the real subspace U_0 and in $U_{5\pi/6}$ is shown in red, blue respectively. The green circle is the SO(2)-orbit of equilibrium E_1.

Thus we can expect that after a center manifold or Liapunov-Schmidt reduction one can apply the equivariant Hopf bifurcation theorem with SO(2) symmetry and verify the existence of a relative equilibrium after bifurcation. In ref. [32] the authors perform a direct bifurcation analysis and show that, for $e+r_2 \neq 0$, a Hopf cycle Q_1 is created which also turns out to be an SO(2)-orbit, i.e. a relative equilibrium. For $e + r_2 = 0$ the cycle degenerates to an SO(2)-orbit of equilibria, since $\omega_c = 0$ and the conditions of equivariant Hopf theorem do not apply.

The secondary bifurcation from the relative equilibrium is expected according to Krupa's theorem [56] to result in relative periodic orbits. In the non-generic case of an SO(2)-orbit of equilibria again according to Krupa [56] theorem, one gets bifurcation to periodic orbits. A secondary bifurcation has been studied in ref. [69]. Since we are interested in Complex Lorenz equations precisely for its symmetry properties we will concentrate on the case that results to generic bifurcations. Before we proceed with this, we briefly examine the special case $e = r_2 = 0$.

4.1.1 The $e = r_2 = 0$ case

When $e = r_2 = 0$ we immediately observe the real subspace $x_2 = y_2 = 0$ is flow invariant and the usual Lorenz equations are recovered. From equivariance, any subspace U_θ on the SO(2)-orbit of the real subspace is invariant as well, for example the imaginary subspace $x_1 = y_1 = 0$. The U_θ's are parameterized by the angle of SO(2) rotations with the restriction $\theta \in [0, \pi)$. We demonstrate the situation for the standard Lorenz equations parameters in Figure 8. A continuum of identical, disjoint "Lorenz mask" attractors exists.

Yet, we cannot choose all initial conditions in one of the flow invariant subspaces U_θ. Indeed, if we use the real subspace as reference we can choose coordinates (x_1, y_1, z, θ) for the subspace U of $\mathbb{R}^5$ foliated by the U_θ's, which makes it clear that this is a 4-dimensional subspace. Points that do not lie on U can be thought of as "mis-rotated": we start with a

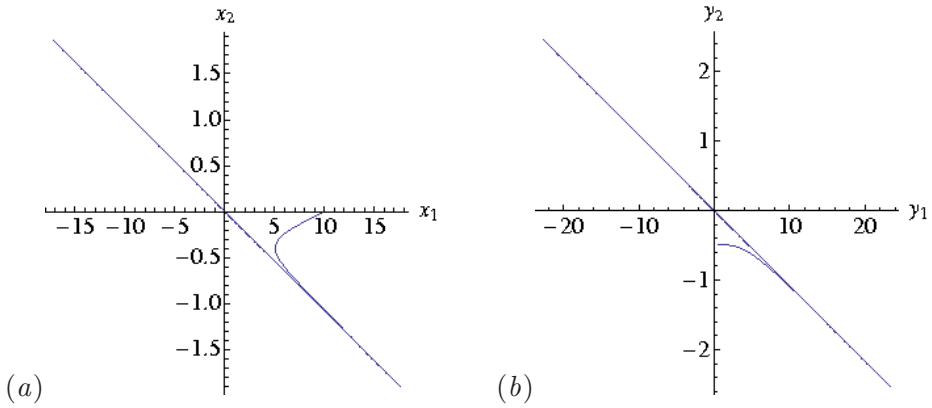

Figure 9: A trajectory of the Complex Lorenz equations dynamics for $r_1 = 28$, $b = 8/3$, $\sigma = 10$, $a = 1$ and $e = r_2 = 0$ with initial conditions on the complement of U in $\mathbb{R}^5$. (a) Projection on the complex x-plane, (b) Projection on the complex y-plane. The trajectory approaches some U_θ.

point on the real subspace and rotate by an angle θ on the (x_1, x_2)-plane and by an angle $\phi \neq \theta$ on the (y_1, y_2) plane. One then would like to know where the asymptotic dynamics for those initial conditions not in U end up. Since the only equilibria of the equations are the origin and the group orbit of equilibrium E_1, we get the hint that the asymptotic dynamics has to be governed by the stable and unstable manifolds of the same equilibria that govern dynamics in U. To see whether this is true we examine the inner product of the vector field at any point $a = (x_1, x_2, y_1, y_2, z)$ with the direction of rotations of the system

$$(\mathfrak{a}.a).v(a) = (r_1 - \sigma - z)\,(x_1 y_2 - x_2 y_1) - r_2\,(x_1 y_1 + x_2 y_2) - e\left(y_1^2 + y_2^2\right) \tag{55}$$

where we have used $\mathfrak{a}$, the Lie algebra generator of SO(2) and $v(a)$, the vector field in (51). We observe that for $e = r_2 = 0$ only $x_1 y_2 - x_2 y_1$ and z appear. By taking the time derivative of $x_1 y_2 - x_2 y_1$ and using (51) we can show that

$$\frac{d}{dt}\,(x_1 y_2 - x_2 y_1) = -(\sigma + 1)\,(x_1 y_2 - x_2 y_1) \tag{56}$$

and, since z is bounded, the inner product in (55) goes to zero as $t \to \infty$[1]. Thus, asymptotically the vector field along any trajectory becomes orthogonal to the direction of infinitesimal rotations and the dynamics approach one of the U_θ's. This is demonstrated in Figure 9.

4.1.2 The $e \neq 0,\ r_2 = 0$ case

In this section we turn to the "laser case" $e \neq 0$, $r_2 = 0$. We work with parameters $r_1 = 28$, $b = 8/3$, $\sigma = 10$, $a = 1$ that correspond to the standard Lorenz values and with detuning set to $e = 1/10$. Figure 10 illustrates the need to project dynamics on orbit space: Dynamics is organized by the interplay of the stable and unstable manifolds of equilibrium E_0 and relative equilibrium Q_1 but the dynamics along the direction of rotation blur the picture and the notion of recurrence becomes relative. We will present various approaches to orbit space reduction in the following sections.

[1] We cannot have $\sigma \leq -1$.

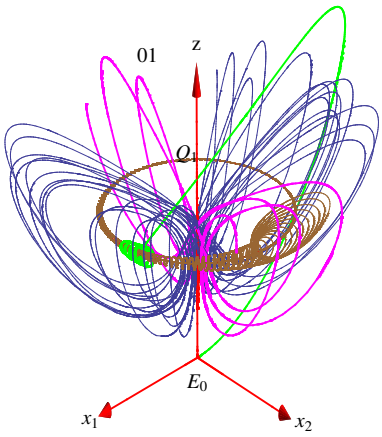

Figure 10: Phase space portrait of Complex Lorenz equations dynamics for $r_1 = 28$, $b = 8/3$, $\sigma = 10$, $a = 1\, e = 1/10$, $r_2 = 0$. Plotted are relative equilibrium Q_1 (red), its unstable manifold (brown), equilibrium E_0, a representative of its unstable manifold (green), 3 repetitions of relative periodic orbit "01"(magenta) and a generic orbit (blue).

To find the location of the relative equilibrium it is convenient to work on polar coordinates defined by $x = \rho_1 e^{i\phi_1}$, $y = \rho_2 e^{i\phi_2}$. Equations (50) with $r_2 = 0$ take the form

$$\begin{aligned}
\dot\rho_1 &= -\sigma\rho_1 + \sigma\rho_2\cos\Phi\,,\\
\dot\rho_2 &= -\rho_2 + \rho_1(r_1 - z)\cos\Phi\,,\\
\dot z &= -bz + \rho_1\rho_2\cos\Phi\,,\\
\dot\Phi &= -e - \frac{\sigma\rho_2\sin\Phi}{\rho_1} - \frac{\rho_1(r_1 - z)\sin\Phi}{\rho_2}\,,
\end{aligned} \tag{57}$$

where $\Phi = \phi_1 - \phi_2$ and the evolution equations for ϕ_1, ϕ_2 are given by

$$\begin{aligned}
\dot\phi_1 &= -\frac{\sigma\rho_2\sin\Phi}{\rho_1}\,,\\
\dot\phi_2 &= e + \frac{\rho_1(r_1 - z)\sin\Phi}{\rho_2}\,.
\end{aligned} \tag{58}$$

The condition for a relative equilibrium is that all time derivatives in (57) vanish from which we get

$$\begin{aligned}
z^{(1)} &= \frac{-e^2 + (r_1 - 1)(\sigma + 1)^2}{(\sigma + 1)^2}\,,\\
\rho_2^{(1)} &= \sqrt{b\,(e^2 + (\sigma + 1)^2)\,z^{(1)}}\,,\\
\rho_1^{(1)} &= \sqrt{bz^{(1)}}\,,\\
\Phi^{(1)} &= -\cos^{-1}\left(\frac{\sigma + 1}{\sqrt{e^2 + (\sigma + 1)^2}}\right)
\end{aligned} \tag{59}$$

Substituting in (58) we get $\dot\phi_1 = \dot\phi_2 = e\sigma/(1 + \sigma) \neq 0$ for $e \neq 0$ and thus we have indeed a relative equilibrium, not a group orbit of equilibria.

Calculation in polar coordinates ρ_1, ρ_2, Φ, z of stability eigenvalues for Q_1 for the set of parameters we use here yields

$$\mu_{1,2} \pm \omega_{1,2} = 0.0938 \pm 10.1945i,\ \lambda_3 = -11.0009,\ \lambda_4 = -13.8534\,. \tag{60}$$

4.1.2.1 Invariant Polynomials

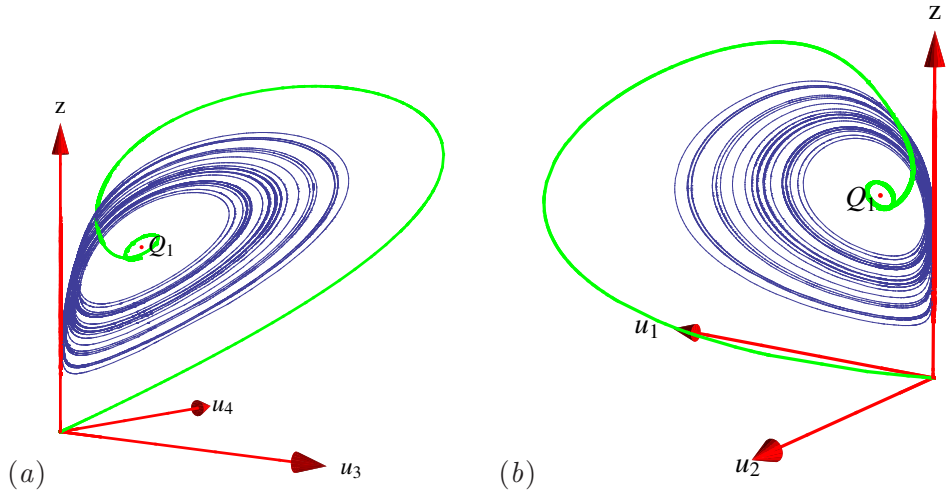

Figure 11: Phase space portraits of Complex Lorenz equations dynamics for $r_1 = 28$, $b = 8/3$, $\sigma = 10$, $a = 1$, $e = 1/10$, $r_2 = 0$ in orbit space. Projecting on invariant polynomials (28).

The first approach we try is by use of invariant polynomials (28), following Gilmore and Letellier [39] who compute invariant polynomials for the same action of SO(2) and use them for symmetry reduction of a system conjugate to Complex Lorenz equationss with $e = -r_2$. For visualization purposes, rather than rewritting the dynamics, we merelly map the orbits from original coordinates to u_i's, Figure 11. In most projections the folding mechanism is hidden since the dynamics is squeezed near the z-axis.

Nevertheless we can now easily identify a suitable Poincaré section, guided by the Lorenz equations example Chapter 3, as one that contains the z-axis and the relative equilibrium, here defined by the condition $u_1 = u_4$. Repeating the procedure followed in Sect. 3.6 we construct the first return map using as coordinate the Euclidean length along the intersection of the unstable manifold of Q_1 with the Poincaré surface of section, measured from Q_1, see Figure 12.

4.1.2.2 Moving frame

As the next choice we explore the invariants generated by the moving frame method. The action (18) of SO(2) on $\mathbb{R}^5$, is regular on $\mathbb{R}^5 \backslash \{x_1 = x_2 = y_1 = y_2 = 0\}$. Thus we can define a slice by, for instance $x_1 = 0$, $x_2 > 0$. We can now construct a moving frame for the action

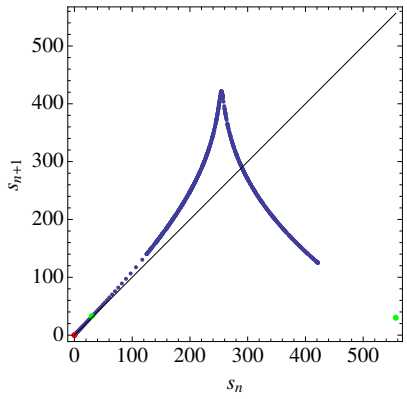

Figure 12: Return map to the Poincaré surface of section $u_1 = u_4$ for Complex Lorenz equations with $r_1 = 28$, $b = 8/3$, $\sigma = 10$, $a = 1$, $e = 1/10$, $r_2 = 0$, projecting on invariant polynomials (28). The return map coordinate is the Euclidean length along the Poincaré section of the unstable manifold of E_1.

(18) of SO(2) as follows. We write out explicitly the group transformations:

$$\overline{x}_1 = x_1 \cos\theta - x_2 \sin\theta\,, \tag{61a}$$
$$\overline{x}_2 = x_1 \sin\theta + x_2 \cos\theta\,, \tag{61b}$$
$$\overline{y}_1 = y_1 \cos\theta - y_2 \sin\theta\,, \tag{61c}$$
$$\overline{y}_2 = y_1 \sin\theta + y_2 \cos\theta\,, \tag{61d}$$
$$\overline{z} = z\,. \tag{61e}$$

Then set $\overline{x}_1 = 0$ and solve (61a) for the group parameter to obtain the moving frame

$$\theta = \tan^{-1}\frac{x_1}{x_2} \tag{62}$$

which brings any point back to the slice.[2] Substituting (62) in the remaining equations we get the invariants

$$\begin{aligned} \overline{x}_2 &= \sqrt{x_1^2 + x_2^2}\,, \\ \overline{y}_1 &= \frac{x_2 y_1 - x_1 y_2}{\sqrt{x_1^2 + x_2^2}}\,, \\ \overline{y}_2 &= \frac{x_1 y_1 + x_2 y_2}{\sqrt{x_1^2 + x_2^2}}\,. \end{aligned} \tag{63}$$

Note the relation to the invariant polynomials (28) and also that no syzygy is present.

On the other hand observe that the denominator is singular on the subspace U_S defined by $x_1 = x_2 = 0$ even though the group action is non-regular only in a subset of U_S, the z-axis $x_1 = x_2 = y_1 = y_2 = 0$. The transformations (63) can thus be characterized as non-optimal, in the sense that we have singularity in a proper superset of Fix (SO(2)). The reason the transformations fail on U_S and not only on the z-axis can be traced back to the way we

[2]Implementation note: Here it is important that $\tan^{-1}$ distinguishes quadrants on the (x_1, x_2) so the transformation results to the correct geometric interpretation.

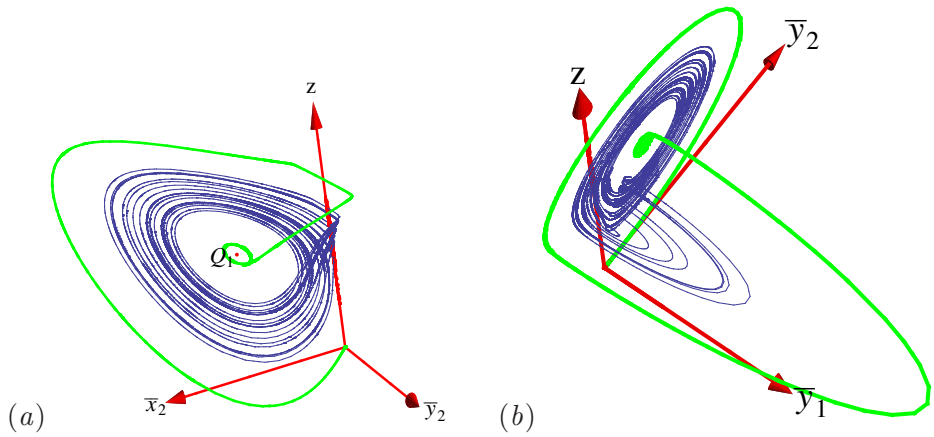

Figure 13: Phase space portraits of Complex Lorenz equations dynamics for $r_1 = 28$, $b = 8/3$, $\sigma = 10$, $a = 1$, $e = 1/10$, $r_2 = 0$ in orbit space. Projecting on invariants given in (63).

construct them. The action of the group can be thought of as a direct sum of irreducible actions and the corresponding invariant (irreducible) subspaces are the (x_1, x_2) and (y_1, y_2) planes. The fact the group acts on each irreducible subspace (that is, it leaves it invariant as a set) implies that we could define a moving frame in any one of them independently and the singular subspace would only depend on the points on which the action is not regular on this irreducible subspace. By choosing an angle in the (x_1, x_2) irreducible subspace as the moving frame map, the singular set is the point $x_1 = x_2 = 0$ in this irreducible subspace, since the group action is not regular, or alternatively, a polar angle is not defined at that point. Going back to the full 5-dimensional space the singular set of the transformations is still given by $x_1 = x_2 = 0$.

The projections in Figure 13 reveal more about the topology of the attractor but also present large "jumps." Note that the invariants (63) are related to the invariant polynomials (28) by division by $\sqrt{x_1^2 + x_2^2}$ (except the one that is not present.) This is the reason we get more clear dynamics: All invariants have the same "dimensions" as the original coordinates. At the same time division by $\sqrt{x_1^2 + x_2^2}$ causes the jumps in the $\overline{y}$ components whenever the magnitude of x comes close to zero. The fact that we do not go through $x = 0$ is coincidental and specific to the problem at hand.

The problem is mostly aesthetical in the present case, but for Kuramoto-Sivashinsky system it will be important to prevent the denominator from vanishing. We observe that generic dynamics cannot enter $\mathrm{Fix}\,(\mathrm{SO}(2))$, i.e. the z-axis, since fixed-point subspaces are flow invariant. Since SO(2) representation in the Complex Lorenz equations example is a direct sum of irreducible representations we cannot take more than one irreducible subspace into account when setting up the normalization equations, at least not in a convenient way. We can however restore democracy between modes and extend validity of the transformations to any point where the group acts freely, by modifying the invariants

as follows:

$$\begin{aligned}
\overline{x}_2 &= (x_1^2 + x_2^2)/r\,, \\
\overline{y}_1 &= -(x_2 y_1 - x_1 y_2)/r\,, \\
\overline{y}_2 &= (x_1 y_1 + x_2 y_2)/r\,, \\
\overline{z} &= z\,, \\
r &= \sqrt{x_1^2 + x_2^2 + y_1^2 + y_2^2}\,.
\end{aligned} \tag{64}$$

This set of invariants lacks a geometric interpretation but results in much cleaner phase portraits, *cf.* Figure 14.

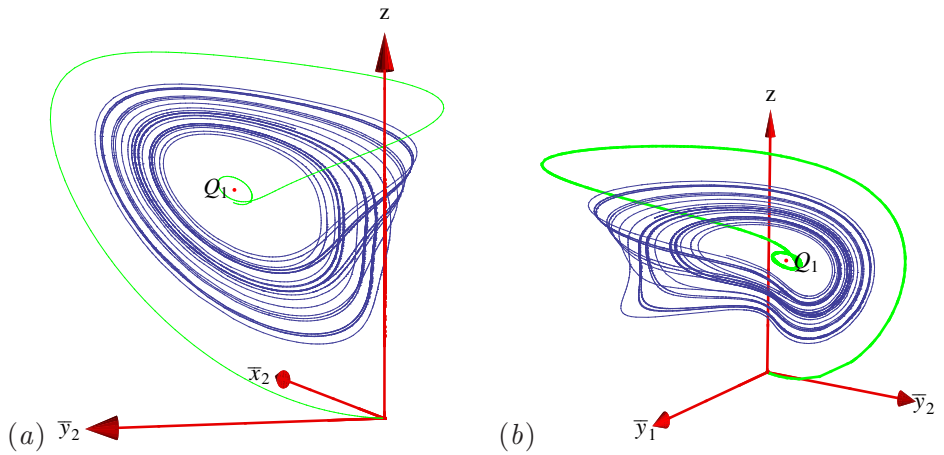

Figure 14: Phase space portraits of Complex Lorenz equations dynamics for $r_1 = 28$, $b = 8/3$, $\sigma = 10$, $a = 1$, $e = 1/10$, $r_2 = 0$ in orbit space. Projecting on invariants given in (64).

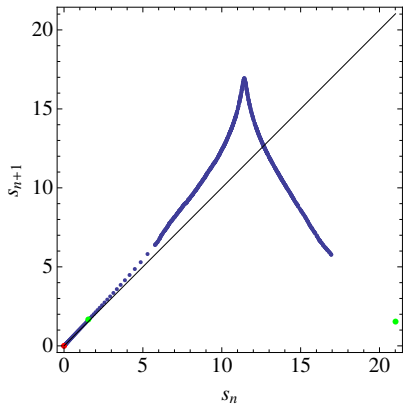

Figure 15: Return map to the Poincaré surface of section $\overline{x}_2 = \overline{y}_2$ for Complex Lorenz equations with $r_1 = 28$, $b = 8/3$, $\sigma = 10$, $a = 1$, $e = 1/10$, $r_2 = 0$, projecting on invariants given in (64). The return map coordinate is the Euclidean length along the Poincaré section of the unstable manifold of E_1.

4.1.2.3 A geometric approach

Even though the computation of invariants with the method of the moving frames is efficient, it is still computationaly prohibitive for very high dimensional flows. We will demonstrate in the example of Complex Lorenz equations how one can use the geometric interpretation of the moving coframe method along with the restriction of the dynamics to a Poincaré section to simply and effectively perform continuous symmetry reduction in high-dimensional flows.

We have noted that SO(2) acts regularly and freely on $X^* = \mathbb{R}^5 \backslash \{x_1 = x_2 = y_1 = y_2 = 0\}$ and thus we are guaranteed to find the fundamental invariants by the method of moving frames if we restrict attention to X^*. Nevertheless the transformations (63) obtained by the moving frame method are singular in the subspace $x_1 = x_2 = 0$. Therefore we would like to ensure that we apply our reduction procedure only on points away from this subspace. A way to achieve this is by a judicious choice of Poincaré section in original space, i.e. before reduction. Since we are ultimatelly interested in reducing the dynamics to a Poincaré return map this is enough for our purposes. Of course locating a Poincaré section is a non-trivial task but as we will see in the following, for the procedure to work we will have to reduce the candidate Poincaré sections to those that are invariant (as a set) under the group action. Furthermore we already have gained the insight from the simpler Lorenz equations problem that a good choice of section is one that passes through the equilibria that organize the flow. Here we are naturally led to choose a section that passes through the relative equilibrium Q_1 such as the section $\mathcal{P}$ defined by $\overline{x}_2 - \overline{y}_2 = 0$ in the variables of (63) or by $x_1^2 + x_2^2 - (x_1 y_1 + x_2 y_2) = 0$ in original space and a suitable orientation condition so that trajectories intersect the section away from $x_1 = x_2 = 0$ subspace. Here the orientation condition has be chosen so that trajectories intersect $\mathcal{P}$ moving from the "outside" of the section in Figure 16 to the "inside". Since $\mathcal{P}$ has been defined by a condition in invariant variables (63) it turns out to be SO(2)-invariant in the full space. Therefore the group orbit of any point on $\mathcal{P}$ lies on $\mathcal{P}$. In Figure 16 the group orbits of the points of intersection of relative periodic orbit "01" have been visualized as circles on $\mathcal{P}$.

The next step is to choose a representative out of each group orbit by means of a section $\mathcal{K}$ that intersects each group orbit exactly once. The existense of a section is guaranteed since a slice as in Proposition 2.29 exists, this was the whole point of restricting the problem to a Poincaré section on which the group *acts* freely. Here we choose $x_1 = 0$ for $\mathcal{K}$. Geometrically this is equivalent to rotating each point of intersection on $\mathcal{K}$ by an appropriate angle so that it lies on $\mathcal{K}$, exactly as prescribed by the moving frame (62). This rotation, a linear operation for any given point, can be applied efficiently even in high dimensional space when the rotation group representation is a direct sum of irreducible representations, as is frequently the case with truncations of PDEs. Of course, the transformation is still non-linear through the dependence on the angle and equivalent to the explicit transformations (63).

Implementing symmetry reduction in any of the above ways, the reward is the same: The dynamics are reduced to a return map to the Poincaré section, which due to the very strong contraction is approximately 1-dimensional. The dynamics on the Poincaré section are parametrized by the Euclidean distance of points along the unstable manifold, as we did for the Lorenz example. The return map is unimodal and allows for systematic determination of all cycles of a given length. Here we were able to determine all cycles up to length 7, using the return map of Figure 15 to generate guesses, and the multiple-shooting algorithm of Sect. 6.3.1 to refine them to machine accuracy.

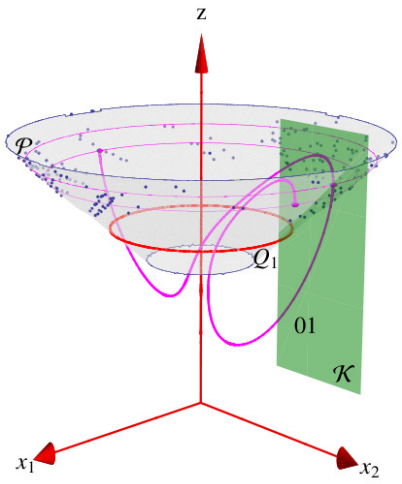

Figure 16: Use of Poincaré surface of section $\mathcal{P}$ and slice $\mathcal{K}$ for symmetry reduction of Complex Lorenz equations dynamics with $r_1 = 28$, $b = 8/3$, $\sigma = 10$, $a = 1$, $e = 1/10$, $r_2 = 0$. Group orbits of the points of intersection of relative periodic orbit "01" have been visualized as circles.

4.1.3 Stability of relative equilibria

In the moving frame method the reduced phase space is identified (at least locally) with the slice $\mathcal{K}$. This provides a means of calculating stability of relative equilibriain reduced phase space. Assume that, as was the case for Complex Lorenz equations, the slice is orthogonal to the group action for any x on $\mathcal{K}$. We observe that for the point x_o on relative equilibrium Q_1 that lies on the slice $\mathcal{K}$ we can decompose $v(x)$ in (6) in a part $v_{\shortparallel}$ parallel to the group action and a part $v_\perp$ on the slice

$$v(x_o) = v_{\shortparallel}(x_o) + v_\perp(x_o)\,. \tag{65}$$

To compute stability eigenvalues of relative equilibrium we only need to consider the linearization of $v_\perp$ which is identified with v in reduced space. It is convenient to introduce the operator

$$\mathbf{P}^\perp = \mathbf{1} - \frac{(\mathfrak{a}.x)\otimes(\mathfrak{a}.x)}{(\mathfrak{a}.x)^2} \tag{66}$$

that projects a vector to the slice. Then for the stability matrix M_{ij} we have

$$\begin{aligned} M_{ij} &\equiv \frac{\partial}{\partial x_j}(\mathbf{P}^\perp.v)_i \\ &= \frac{\partial}{\partial x_j}(P^\perp_{in}v_n) \\ &= P^\perp_{in}\frac{\partial v_n}{\partial x_j} + \frac{\partial P^\perp_{in}}{\partial x_j}v_n \end{aligned} \tag{67}$$

Now

$$\begin{aligned} P^{\perp}_{in} &= \delta_{in} - \frac{(\mathfrak{a}.x)_i(\mathfrak{a}.x)_n}{(\mathfrak{a}.x)^2} \\ &= \delta_{in} - \frac{\mathfrak{a}_{iq}.x_q\mathfrak{a}_{n\ell}.x_\ell}{(\mathfrak{a}.x)^2} \end{aligned} \tag{68}$$

and

$$\begin{aligned} \frac{\partial P^{\perp}_{in}}{\partial x_j} &= -\frac{\partial}{\partial x_j}\left(\frac{\mathfrak{a}_{iq}.x_q\mathfrak{a}_{n\ell}.x_\ell}{(\mathfrak{a}.x)^2}\right) \\ &= -\left(\frac{\mathfrak{a}_{iq}\delta_{jq}\mathfrak{a}_{n\ell}x_\ell}{(\mathfrak{a}.x)^2} + \frac{\mathfrak{a}_{iq}x_q\mathfrak{a}_{n\ell}\delta_{j\ell}}{(\mathfrak{a}.x)^2} - \frac{\mathfrak{a}_{iq}x_q\mathfrak{a}_{n\ell}x_\ell}{(\mathfrak{a}.x)^4}\frac{\partial}{\partial x_j}(\mathfrak{a}.x)^2\right) \\ &= -\left(\frac{\mathfrak{a}_{ij}\mathfrak{a}_{n\ell}x_\ell}{(\mathfrak{a}.x)^2} + \frac{\mathfrak{a}_{iq}x_q\mathfrak{a}_{nj}}{(\mathfrak{a}.x)^2} - 2\frac{\mathfrak{a}_{iq}x_q\mathfrak{a}_{n\ell}x_\ell}{(\mathfrak{a}.x)^4}\mathfrak{a}_{mj}\mathfrak{a}_{mp}x_p\right) \\ &= -\frac{1}{(\mathfrak{a}.x)^2}\left(\mathfrak{a}_{n\ell}x_\ell\left(\mathfrak{a}_{ij} - \frac{\mathfrak{a}_{iq}x_q}{(\mathfrak{a}.x)^2}\mathfrak{a}_{mj}\mathfrak{a}_{mp}x_p\right) + \mathfrak{a}_{iq}x_q\left(\mathfrak{a}_{nj} - \frac{\mathfrak{a}_{n\ell}x_\ell}{(\mathfrak{a}.x)^2}\mathfrak{a}_{mj}\mathfrak{a}_{mp}x_p\right)\right) \\ &= -\frac{1}{(\mathfrak{a}.x)^2}\left(\mathfrak{a}_{n\ell}x_\ell\left(\delta_{im} - \frac{\mathfrak{a}_{iq}x_q}{(\mathfrak{a}.x)^2}\mathfrak{a}_{mp}x_p\right)\mathfrak{a}_{mj} + \mathfrak{a}_{iq}x_q\left(\delta_{nm} - \frac{\mathfrak{a}_{n\ell}x_\ell}{(\mathfrak{a}.x)^2}\mathfrak{a}_{mp}x_p\right)\mathfrak{a}_{mj}\right) \\ &= -\frac{1}{(\mathfrak{a}.x)^2}\left(\mathfrak{a}_{n\ell}x_\ell P^{\perp}_{im}\mathfrak{a}_{mj} + \mathfrak{a}_{iq}x_q P^{\perp}_{nm}\mathfrak{a}_{mj}\right) \end{aligned} \tag{69}$$

Therefore (67) takes the form

$$M_{ij} = P^{\perp}_{in}\frac{\partial v_n}{\partial x_j} - \frac{1}{(\mathfrak{a}.x)^2}\left(\mathfrak{a}_{n\ell}x_\ell P^{\perp}_{im}\mathfrak{a}_{mj} + \mathfrak{a}_{iq}x_q P^{\perp}_{nm}\mathfrak{a}_{mj}\right)v_n \tag{70}$$

or in matrix form

$$\mathbf{M} = \mathbf{P}^{\perp}\mathbf{A} - \frac{1}{(\mathfrak{a}.x)^2}\left([v.(\mathfrak{a}.x)]\left(\mathbf{P}^{\perp}\mathfrak{a}\right) + (\mathfrak{a}.x)\otimes\left[v.\left(\mathbf{P}^{\perp}\mathfrak{a}\right)\right]\right) \tag{71}$$

where $A_{ij} = \frac{\partial v_i}{\partial x_j}$. This expression allows to calculate stability of relative equilibria working in the equivariant variables, without explicit knowledge of the form the differential assumes in reduced space. Applying (71) for relative equilibrium Q_1 of Complex Lorenz equations we obtain the same eigenvalues (60) we computed in polar coordinates along with a zero eigenvalue due to the fact that we still work in the equivariant variables.

4.1.4 Integration on the slice

If we replace our differential equations (6) with the system

$$\frac{dx}{dt} = \mathbf{P}^{\perp}v(x)\,, \tag{72}$$

solutions will stay on the slice $\mathcal{K}$ for any initial condition on $\mathcal{K}$ as there is no component of $\mathbf{P}^{\perp}v(x)$ in the direction of the continuous symmetry.

For Complex Lorenz equations a trajectory of (72) on the unstable manifold of Q_1 is shown in Figure 17. Our claim that the trajectory will stay on the slice is not verified by this figure, even though this could be attributed to numerical issues.

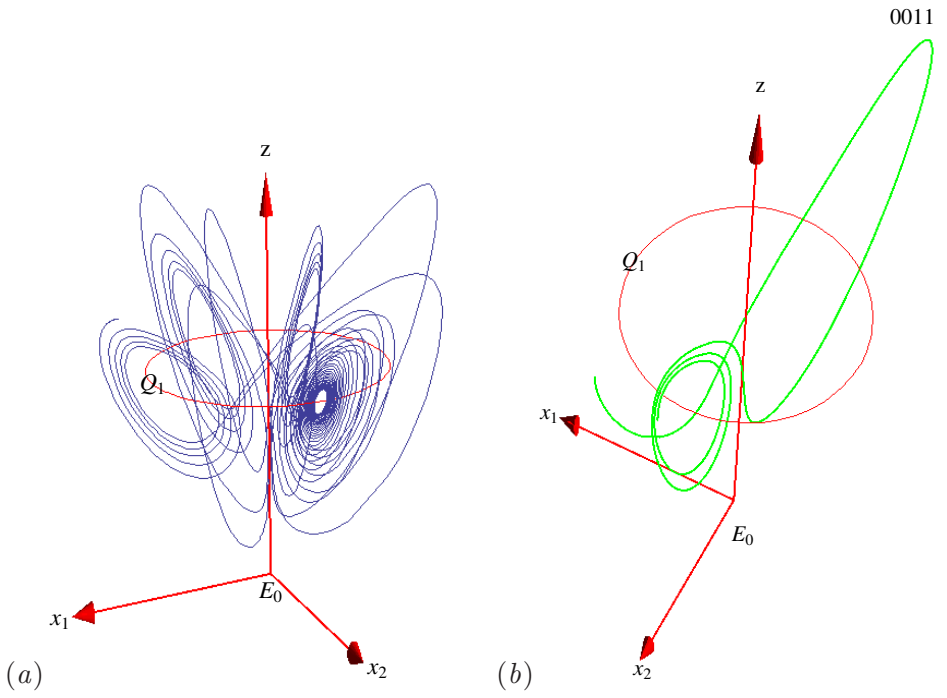

Figure 17: Attempt to restrict Complex Lorenz equations dynamics on the slice $\mathcal{K}$ through (72). (a) A trajectory initiated on the unstable manifold of Q_1, (b) relative periodic orbit "0011" ($r_1 = 28$, $b = 8/3$, $\sigma = 10$, $a = 1$, $e = 1/10$, $r_2 = 0$).

In figure Figure 18 we evaluate the accuracy of integration of (72) by integrating initial conditions for several relative periodic orbits both in phase space and on the section and compute the distance $|\overline{x}(t) - \overline{x^{\perp}}(t)|$ in invariant variables (64) (the norm is Euclidean). The distance does not grow exponentially indicating that numerical solution of (72) is accurate.

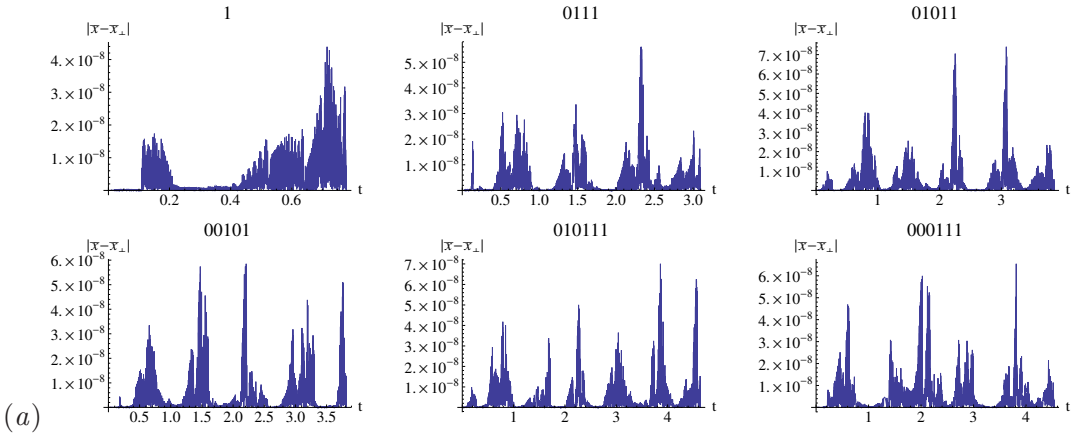

(a)

Figure 18: Distance of $x^{\perp}(t)$ to $x(t)$ in invariant variables(64) for selected relative periodic orbits of Complex Lorenz equations ($r_1 = 28$, $b = 8/3$, $\sigma = 10$, $a = 1$, $e = 1/10$, $r_2 = 0$).

CHAPTER V

KURAMOTO-SIVASHINSKY SYSTEM

5.1 Kuramoto-Sivashinsky equation

The Kuramoto-Sivashinsky [henceforth KS] system was derived by Kuramoto and Tsuzuki [57] as a phase equation for reaction-diffusion systems described by Complex Ginzburg-Landau equation and independently by Sivashinsky [77] to describe instabilities in laminar flame fronts. It also appears in a variety of contexts including thin falling films and interfacial instabilities between concurrent viscous fluids [4; 61]. Our motivation for its study is that it is one of the simplest nonlinear PDEs that exhibit features reminiscent of fluid turbulence and thus it is a convenient system to test new ideas.

In the formulation adopted here, the time evolution of the 'flame front velocity' $u = u(x,t)$ is given by

$$u_t = F(u) = -\tfrac{1}{2}(u^2)_x - u_{xx} - u_{xxxx}\,, \qquad x \in [-L/2, L/2]\,, \tag{73}$$

with appropriate boundary conditions, as discussed in Sect. 5.1.1. Here $t \geq 0$ is the time, and x is the spatial coordinate. The subscripts x and t denote partial derivatives with respect to x and t.

5.1.1 Boundary conditions and system size

Ideally we would like to work in a system of infinite spatial extend, i.e. in the limit $L \to \infty$. Although solutions of KS equations in this limit have appeared, *cf.* for example refs. [48; 30], it is more convenient, both computationally and theoretically, to work with periodic boundary conditions

$$u(x,t) = u(x+L,t)\,, \tag{74}$$

and this is the usual choice in the literature and the one followed in this thesis. Justification of this choice will be given in Sect. 5.1.2, in conjunction with the discussion of the symmetries of the system.

Another common choice of boundary conditions is

$$u(0,t) = u(L,t) = 0\,, \tag{75}$$

which restricts the system to the subspace of odd functions. This choice will also be discussed in Sect. 5.1.2.

In what follows we shall state results of all calculations either in units of the system size L or the 'dimensionless system size' $\tilde{L} = L/2\pi$. All numerical results presented in this thesis are for $\tilde{L} = 22/2\pi = 3.5014\ldots$, unless otherwise noted. The system size leads to a system that is just "turbulent" enough to have interesting dynamics, *cf.* Sect. 7.1, while being still rather tractable and can be used as a test bed for continuous symmetry reduction and a dynamical systems approach, see also Sect. 5.1.3.

5.1.2 Symmetries of Kuramoto-Sivashinsky system

In an unbounded domain, $x \in (-\infty, \infty)$, KS equation is equivariant under the action of the non-compact Euclidean group E(1): If $u(x,t)$ is a solution, then $\tau(\ell)\, u(x,t) = u(x+\ell,t)$ is an equivalent solution for any shift $\ell \in \mathbb{R}$, as is the reflection ('parity' or 'inversion') κ defined by

$$\kappa\, u(x) = -u(-x)\,. \tag{76}$$

Imposing periodic boundary conditions we restrict attention to the subspace $[-L, L]$ in which only the compact subgroup O(2) of E(1) acts by:

$$\tau_{\ell/L}\, u(x,t) = u(x+\ell,t)\,, \qquad \ell \in [-L/2, L/2] \tag{77}$$

and reflections (76). Here we use subscript notation for shifts to differentiate with the case of E(1). Moreover, we only consider perturbations within this subspace, i.e. we do not consider subharmonic perturbations. The system size L affects the representation of O(2), *cf.* Sect. 5.1.4. Reflection generates the dihedral subgroup $\mathrm{D}_1 = \{1, \kappa\}$ of O(2). Boundary conditions (75) restrict the system to $\mathrm{Fix}\,(\mathrm{D}_1)$ and thus in that case symmetry D_1 is impossed to all solutions. To avoid technical difficulties associated with the action of O(2) on an infinite dimensional space we will discuss the isotropy subgroups of O(2) in Sect. 5.1.6, after we truncate (79) to finite order.

The KS equation is also Galilean invariant: if $u(x,t)$ is a solution, then $u(x-ct,t) - c$, with c an arbitrary constant speed, is also a solution. As one can verify by integrating (73) with respect to x over the periodic domain $[-L/2, L/2]$ the quantity $\int_{-L/2}^{L/2} u\, dx$ is conserved and we can, without loss of generality, set it equal to zero. This corresponds to the choice $c = 0$, therefore eliminating Galilean invariance.

5.1.3 Why $L = 22$ on periodic domain?

For Kuramoto-Sivashinsky system with periodic boundary conditions one expects to find traveling wave (relative equilibrium) and modulated amplitude traveling wave (relative periodic orbit) solutions, exactly the kind of solutions that we set out to understand and organize. Indeed, a very detailed bifurcation study of such solutions for Kuramoto-Sivashinsky equation has been carried out by Brown and Kevrekidis [7], see discussion in Sect. 5.1.8. In our work the emphasis is on working with a specific system size, with specific boundary conditions, and determining and labeling all unstable periodic and relative periodic solutions (up to a given topological length). A bifurcation analysis is not practical for such a task as global bifurcations that lead to creation and disappearance of (relative) periodic orbits are hard to track. Therefore one needs to understand the geometry of phase space in order to detect and organize the compact solutions systematically.

The Kuramoto-Sivashinsky system of size $L = 22$ appears amenable to such a geometric study, yet it provides new challenges. As we will see in Chapter 7, many of the invariant objects (equilibria, relative equilibria, periodic orbits, relative periodic orbits) have more than one unstable eigendirections, a situation that has not been dealt with in previous Kuramoto-Sivashinsky equation studies in terms of periodic orbits [14; 58; 60], and which very often occurs in the studies of plane Couette flow [38; 45; 46; 44]. Nevertheless, the system is not large enough to exhibit many unstable, essentially non-separated (quasi-continuous) eigenvalues. Systems with quasi-continuous spectra are known as *spatio-temporally chaotic* in the sense that they are disordered both in space and in time [64] and a dynamical description of such systems presents many more challenges than we would like to be faced

with while we try for the first time to understand the organization of a flow in terms of (modulated) traveling wave solutions. The $L = 22$ system remains within reach of a dynamical description, see Chapters 7 and 8, while offering valuable insight on how to deal with other, larger, more turbulent or realistic systems.

5.1.4 Fourier space

O(2) equivariance makes it convenient to work in Fourier space,

$$u(x,t) = \sum_{k=-\infty}^{+\infty} a_k(t) e^{ikx/\tilde{L}} , \tag{78}$$

with the 1-dimensional PDE (73) replaced by an infinite set of ODEs for the complex Fourier coefficients $a_k(t)$:

$$\dot{a}_k = v_k(a) = (q_k^2 - q_k^4)\, a_k - i\frac{q_k}{2} \sum_{m=-\infty}^{+\infty} a_m a_{k-m} , \tag{79}$$

where $q_k = k/\tilde{L}$. Since $u(x,t)$ is real,

$$a_k = a_{-k}^* , \tag{80}$$

and we can replace the sum by a $k > 0$ sum. Note that $\dot{a}_0 = 0$ in (79) as a result of Galilean invariance and a_0 is a conserved quantity fixed to $a_0 = 0$ by the condition $\int_{-L/2}^{L/2} u\, dx$=0. In the Fourier basis O(2) acts absolutely irreducibly on each complex plane $(\mathrm{Re}\,(\mathrm{a_k}), \mathrm{Im}\,(\mathrm{a_k}))$ and the linear part of (79) is conveniently diagonalized. Indeed, the translation operator action on the Fourier coefficients (78), represented here by a complex valued vector $a = \{a_k \in \mathbb{C} \,|\, k = 1, 2, \ldots\}$, is given by

$$\tau_{\ell/L}\, a = \mathbf{g}(\ell)\, a , \tag{81}$$

where $\mathbf{g}(\ell) = \mathrm{diag}(e^{iq_k \ell})$ is a complex valued diagonal matrix, which amounts to the k-th mode complex plane rotation by an angle $k\,\ell/\tilde{L}$. The reflection acts on the Fourier coefficients by complex conjugation and a change of sign,

$$\kappa\, a = -a^* . \tag{82}$$

5.1.5 Truncation

Dynamical phase space representation of a PDE is ∞-dimensional, but the KS flow is strongly contracting and its non-wondering set, and, within it, the set of invariant solutions investigated here, is embedded into a finite-dimensional inertial manifold [31] in a non-trivial, nonlinear way. The existence of an inertial manifold for Kuramoto-Sivashinsky equationwith both odd and periodic boundary conditions has been proved and several bounds for its dimension have been found, *cf.* ref. [50] and references therein. The best current bound in dimension of inertial manifold for KS equation with periodic boundary condition is, to the author's knowledge, given in refs. [73; 50]: $O(L^{2.46})$ for $L \in [2\pi, 6\pi]$.

The fact that the asymptotic dynamics lies on a finite dimensional manifold justifies truncation of the infinite tower of equations (79) to finite order N. According to the bound $O(L^{2.46}) \simeq 2000$ for $L = 22$ and we would expect to need even more Fourier modes, since the

Fourier basis is not directly connected to coordinates on the inertial manifold of KSe and would therefore be less optimal than an approach that approximates such coordinates, for example [52; 51]. Nevertheless such a bound seems rather inflated compared to numerical simulations of the asymptotic dynamics that typically require $O(10)-O(100)$ Fourier modes. In practice we keep $16 \leq N \leq 128$ Fourier modes in numerical simulations and check the robustness of the results against increase of N.

5.1.6 Isotropy lattice and invariant subspaces

Let N be the number of Fourier modes retained in (79) and observe that the action of $O(2)$ on $\mathbb{R}^N$ by (81) and (82) is, up to the minus sign in (82), identical to the action (21) of O(2) on $\mathbb{C}^N$ studied in Sect. 2.1.1. The isotropy lattice remains unchanged but fixed-point subspaces of the dihedral subgroups are affected. Fixed-point subspaces of C_q, given by the condition

$$a_k = 0 \text{ unless } k = qj\,,\ j = 1, \ldots \lfloor n/q \rfloor\,, \tag{83}$$

remain unchanged but the fixed-point subspaces of the dihedral subgroups $\mathrm{Fix}\,(\mathrm{D}_m)$ are now given by the conditions

$$a_k = 0 \text{ unless } k = mj\,,\ j = 1, \ldots \lfloor n/m \rfloor\,, \tag{84}$$

$$\mathrm{Re}\,(\mathrm{a_k}) = 0 \text{ for } \mathrm{k} = 1, \ldots, \mathrm{n}\,. \tag{85}$$

In relation to physical space we observe that $\mathrm{Fix}\,(\mathrm{D}_1)$ is the subspace of antisymmetric functions $Re(z_k) = 0$, $\forall k$ or $u(-x) = -u(x)$ while for the action (21) the corresponding subspace would be that of symmetric functions.

5.1.7 Equilibria and their bifurcations

Equilibria (or the steady solutions) are the fixed profile time-invariant solutions,

$$u(x,t) = u_q(x)\,. \tag{86}$$

Due to the translational symmetry, the KS system also allows for relative equilibria (traveling waves, rotating waves), characterized by a fixed profile $u_q(x)$ moving with constant speed c, i.e.

$$u(x,t) = u_q(x - ct)\,. \tag{87}$$

Here suffix $_q$ labels a particular invariant solution. Because of the reflection symmetry (76), the relative equilibria come in counter-traveling pairs $u_q(x-ct)$, $-u_q(-x+ct)$.

The relative equilibrium condition for the Kuramoto-Sivashinsky PDE (73) is the ODE

$$\tfrac{1}{2}(u^2)_x + u_{xx} + u_{xxxx} = c\,u_x \tag{88}$$

which can be analyzed as a dynamical system in its own right. Integrating once we get

$$\tfrac{1}{2}u^2 - cu + u_x + u_{xxx} = E\,. \tag{89}$$

This equation can be interpreted as a 3-dimensional dynamical system with spatial coordinate x playing the role of 'time,' and the integration constant E can be interpreted as 'energy,' see Sect. 5.2 and Figure 19.

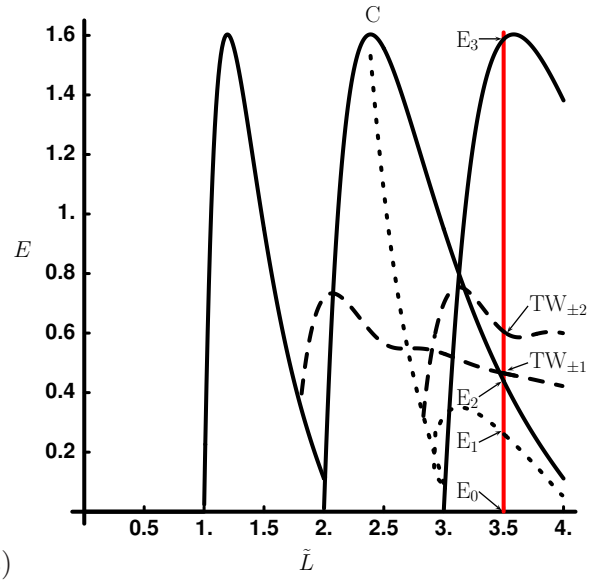

(a)

Figure 19: The energy (102) of the equilibria and relative equilibria that exist up to $L = 22$, $\tilde{L} = 3.5014\ldots$, plotted as a function of the system size $\tilde{L} = L/2\pi$ (additional equilibria, not present at $L = 22$ are given in ref. [42]). Solid curves denote n-cell solutions E_2 and E_3, dotted curves the GLMRT equilibrium E_1, and dashed curves the relative equilibria $TW_{\pm1}$ and $TW_{\pm2}$. The parameter α of refs. [55; 42] is related to the system size by $\tilde{L} = \sqrt{\alpha/4}$.

In the Fourier representation the relative equilibria time dependence is

$$a_k(t)e^{-itcq_k} = a_k(0)\,. \tag{90}$$

Differentiating with respect to time, we obtain the Fourier space version of the relative equilibrium condition (88),

$$v_k(a) - iq_k c a_k = 0\,, \tag{91}$$

which we solve for (time independent) a_k and c, see Chapter 7.

In a periodic box of size L both equilibria and relative equilibria are periodic solutions embedded in 3-d space, conveniently represented as loops in (u, u_x, u_{xx}) space, see Figure 21 (d). In this representation the continuous translation symmetry is automatic – a rotation in the $[0, L]$ periodic domain only moves the points along the loop. For an equilibrium the points are stationary in time; for relative equilibrium they move in time, but in either case, the loop remains invariant. Unfortunately this visualization has not helped our understanding of Kuramoto-Sivashinsky equation state space.

The equilibria and relative equilibria of KS equation and their bifurcations have been the object of extensive study and a literature survey cannot be exhaustive. The results of relevance for this thesis can be found in refs. [68; 72; 42; 55; 2]. Although these results were obtained by direct bifurcation analysis rather than with methods of equivariant bifurcation theory, the relation of bifurcations to O(2) symmetry has been recognized in the literature particularly in refs. [55; 2]. The relation of the bifurcations found numerically (and in some cases analytically) in ref. [55] to the predictions of equivariant bifurcation theory is discussed in Krupa [56] but without explicit calculations. In this section we describe some

of the elementary and well known bifurcations in KS equation from the point of view of equivariant bifurcation theory.

Since the origin (u(x,t)=0 in physical space) is the fixed-point subspace of O(2) it is, by Proposition 2.11, flow invariant and thus an equilibrium. From commutation relation (15) we conclude that the linear stability matrix (see Sect. 6.2) $A(0)$ and the representation of the symmetry group O(2) share a complete set of eigenvectors, the Fourier modes. Moreover, since O(2) acts absolutely irreducibly on each Fourier plane $A(0)$ is diagonal (in real Fourier basis) with eigenvalues $\lambda_0^{(k)} = (q_k^2 - q_k^4)$, from (79). For $L < 2\pi$ the origin is linearly stable and due to the hyperviscous damping u_{xxxx} it is the global attractor [55]. At $L = 2\pi$ the origin loses stability and due to the diagonal form of $A(0)$ the kernel of the linearization is immediately seen to be the $k = 1$ irreducible subspace. Taking into account the orthogonality of the Fourier basis, the Lyapunov-Schmidt reduction [40] is automatic and we can work in the $k = 1$ subspace (*cf.* "Restriction Lemma" in ref. [55] for technical details). In this subspace all requirements of Equivariant Branching Lemma [40] are satisfied: O(2) acts absolutely irreducibly, $v_1(a)$ is equivariant (Lyapunov-Schmidt reduction respects symmetry), the eigenvalue crossing condition holds $\frac{d}{dL}\lambda_0^{(1)}(2\pi) \neq 0$, and finally D_1 is an axial subgroup since $\mathrm{Fix}\,(\mathrm{D}_1)$ is the imaginary axis in the complex a_1 plane. Therefore there is a unique solution branch of equilibria in $\mathrm{Fix}\,(\mathrm{D}_1)$, i.e. with symmetry D_1. This is known as the unimodal branch in the literature. The stability of the bifurcating equilibrium can not be determined from symmetry arguments and one has to take into account the evolution equations (79). The unimodal equilibrium is stable at bifurcation [55]. Under the action of τ we get a continuous family of equilibria for any equilibrium in D_1.

The bifurcation scenario repeats itself each time $L = 2\pi k$: The k'th mode eigenvector of the origin looses stability and an equilibrium with symmetry D_k is born, giving rise to the k-modal branch. The Lyapunov-Schmidt reduction and application of Equivariant branching lemma carries through in exactly the same way. In ref. [55] the observation is made that one can get the k-modal branch from the unimodal through the substitution $u(x) \mapsto u(kx)$ and therefore the k-modal branches are called k-fold replications of the unimodal branch, *cf.* also ref. [56]. Note that the k-modal branch with $k > 1$ "inherits" the unstable directions of the origin and thus are born unstable at the bifurcation. In ref. [42] states in the k-modal branch are called k-cell states. Condition (85) implies that in these states only the Fourier modes a_j where j is a multiple of k are non zero. Each k-modal branch merges with the $2k$-modal branch, see Figure 19 and refs. [55; 42]. Note that, according to Example 2.18, $\mathrm{Fix}\,(\mathrm{D}_1) \supset \mathrm{Fix}\,(\mathrm{D}_k)$ for all k, so all unimodal equilibria are antisymmetric.

The replication observed in primary bifurcations is not carried to the secondary bifurcations that are much richer. From here on we only consider bifurcations that play a role in the dynamics for our system size, $L = 22$, see Figure 19. The E_2 and E_3 indicated in that diagram belong in the bimodal and trimodal branches, respectively.

The 1-cell state loses stability and bifurcates to a branch of stable relative equilibria, which later on becomes unstable through a Hopf bifurcation [55; 42]. This is the branch indicated as $\mathrm{TW}_{\pm 1}$ in Figure 19. Since relative equilibria are not in $\mathrm{Fix}\,(\mathrm{D}_1)$ and they are invariant, as a set, under translations (81), they have to come in copies under the action of D_1. The sign in $\mathrm{TW}_{\pm 1}$ indicates direction of rotation, see (87).

At point C in Figure 19 the 2-cell state bifurcates to a type of equilibrium solution found by La Quey, Mahajan, Rutherford and Tang [72] and generalized by Greene and Kim who refer to them as GLMRT equilibria. In ref. [55] this branch of solutions is refered to as bi-tri branch as it is later on terminated at the trimodal branch. Bi-tri equilibria live in

Fix (D_1) and have components in all Fourier modes. At the point where the bi-tri branch meets the trimodal branch a new branch is born that is still in Fix (D_1). This is seen as a continuation of the bi-tri branch in ref. [55]. The equilibrium labeled E_1 in Figure 19 is in this branch.

Finally the relative equilibrium that is labeled $TW_{\pm 2}$ belongs to a branch bifurcating from the bi-tri branch in a Hopf bifurcation. Once again the relative equilibria come in D_1 related, counter-traveling pairs.

5.1.8 Relative periodic orbits and periodic orbits

As a result of invariance under $\tau_{\ell/L}$, KS equation can have relative periodic orbit solutions with a profile $u_p(x)$, period T_p, and a nonzero shift ℓ_p

$$\tau_{\ell_p/L} u(x, T_p) = u(x + \ell_p, T_p) = u(x, 0) = u_p(x)\,. \tag{92}$$

Relative periodic orbits (92) are periodic in $v_p = \ell_p/T_p$ co-rotating frame (see Figure 34), but in the stationary frame their trajectories are quasiperiodic. Due to the reflection symmetry (76) of KS equation, every relative periodic orbit $u_p(x)$ with shift ℓ_p has a symmetric partner $-u_p(-x)$ with shift $-\ell_p$. In Fourier space we have:

$$\mathbf{g}(\ell_p) f^{T_p}(a_p) - a_p = 0\,, \tag{93}$$

with $\mathbf{g}$ as in (81).

KS equation can also have periodic solutions characterized by a profile $u_p(x)$, and period T_p. In terms of symmetry it is easier to think of them in (truncated) Fourier space. For any discrete[1] subgroup in the isotropy lattice we can have periodic solutions with spatial symmetry D_k or C_k. For all γ in D_k or C_k.

$$\gamma a_p(t) = a_p(t)\,, \qquad \forall t \in [0, T_p]\,. \tag{94}$$

Such a solution lives in Fix (D_k) of Fix (C_k). The periodic orbits found in refs. [14; 60], for example, are all in Fix (D_1), as a result of restricting the dynamics to that subspace by the choice of antisymmetric boundary conditions. In our case, for $L = 22$, the dynamics in Fix (D_1) are dominated by attracting (within the subspace) heteroclinic connections and thus we have no periodic orbits of this type, or in any other of the Fix (D_k) subspaces, see Chapter 7. Moreover spatial symmetries have to be in the isotropy lattice, see Chapter 3 of ref. [40] so there are no more possibilities for orbits with just spatial symmetry.

The second type of periodic orbits would have spatio-temporal symmetry with spatial part a discrete subgroup in the isotropy lattice $\Sigma_{a_p(t)} = D_k$ or C_k and trivial spatial symmetry. Yet, due to algebraic restrictions on possible spatio-temporal symmetries, see Chapter 3 of ref. [40], the spatial part has to be cyclic and thus we are left with D_1 and C_k as our possibilities. For our system size, $L = 22$, we have found no periodic orbits with isotropy subgroup C_k, see Chapter 7. We have found periodic orbits with isotropy subgroup D_1, period $\mathcal{T}_p$, which satisfy

$$\kappa a(t + T_p) = a(t)\,, \tag{95}$$

where $T_p = \mathcal{T}_p/2$ by the relation $\kappa^2 = e$. We choose to label those periodic orbits with the half-period T_p because this will be the period in the $O(2)$-reduced space, where the segment

[1] Recall from Example 2.18 that O(2) fixes the origin, so we cannot have periodic orbits with spatial symmetry O(2).

of the orbit for time $[T_p, \mathcal{T}_p]$ is a repeat of the *prime* segment for $[0, T_p]$. Thus we will refer to those orbits as pre-periodic of period T_p. Periodic orbits (95) live in the principal stratum and thus their group orbit under translations (81) is a manifold of equivalent solutions. Returning to physical space we have

$$\kappa u(x+\ell, T_p) = -u(-x-\ell, T_p) = u(x+\ell, 0) = u_p(x)\,, \tag{96}$$

the family of equivalent solutions parameterized by ℓ (as the choice of the reflection point is arbitrary, the shift can take any value in $-L/2 < \ell \leq L/2$). Such pre-periodic orbits are a hallmark of any dynamical system with a discrete symmetry, where they have a natural interpretation as periodic orbits in the fundamental domain [22; 20].

Brown and Kevrekidis [7] study bifurcations branches of relative periodic orbits for a wide range of system sizes L for Kuramoto-Sivashinsky equation. For our system size they identify two relative periodic orbit branches. They are created when either a heteroclinic cycle (see Chapter 7) or relative equilibrium becomes unstable, see also refs. [56; 1; 2]. In ref. [7] partially hyperbolic invariant tori are also found for larger systems, see Chapter 9.

5.2 Energy transfer rates

In physical settings where the observation times are much longer than the dynamical 'turnover' and Lyapunov times (statistical mechanics, quantum physics, turbulence) periodic orbit theory [20] provides highly accurate predictions of measurable long-time averages such as the dissipation and the turbulent drag [38]. Physical predictions have to be independent of a particular choice of ODE representation of the PDE under consideration and, most importantly, invariant under all symmetries of the dynamics. In this section we discuss a set of such physical observables for the 1-d KS invariant under reflections and translations. They offer a representation of dynamics in which the symmetries are explicitly quotiented out. We shall use these observable in Sect. 7.2 in order to visualize a set of solutions on these coordinates. They implement symmetry reduction, but their utility, as we will see in Sect. 7.2, has been limited.

The space average of a function $a = a(x,t) = a(u(x,t))$ on the interval L,

$$\langle a \rangle = \frac{1}{L} \oint dx\; a(x,t)\,, \tag{97}$$

is in general time dependent. Its mean value is given by the time average

$$\overline{a} = \lim_{t\to\infty} \frac{1}{t} \int_0^t d\tau\; \langle a \rangle = \lim_{t\to\infty} \frac{1}{t} \int_0^t \frac{1}{L} \oint d\tau\, dx\, a(x,\tau)\,. \tag{98}$$

The mean value of $a = a(u_q) \equiv a_q$ evaluated on q equilibrium or relative equilibrium $u(x,t) = u_q(x - ct)$ is

$$\overline{a}_q = \langle a \rangle_q = a_q\,. \tag{99}$$

Evaluation of the infinite time average (98) on a function of a periodic orbit or relative periodic orbit $u_p(x,t) = u_p(x, t+T_p)$ requires only a single T_p traversal,

$$\overline{a}_p = \frac{1}{T_p} \int_0^{T_p} d\tau\; \langle a \rangle\;. \tag{100}$$

Equation (73) can be written as

$$u_t = -V_x\,, \qquad V(x,t) = \tfrac{1}{2}u^2 + u_x + u_{xxx}\,. \tag{101}$$

If u is 'flame-front velocity' then E, defined in (89), can be interpreted as the mean energy density. So, even though KS is a phenomenological small-amplitude equation, the time-dependent quantity

$$E = \frac{1}{L}\oint dx\, V(x,t) = \frac{1}{L}\oint dx\, \frac{u^2}{2} \tag{102}$$

has a physical interpretation [42] as the average 'energy' density of the flame front. This analogy to the mean kinetic energy density for the Navier-Stokes motivates what follows.

The energy (102) is intrinsic to the flow, independent of the particular ODE basis set chosen to represent the PDE. However, as the Fourier amplitudes are eigenvectors of the translation operator, in the Fourier space the energy is a diagonalized quadratic norm,

$$E = \sum_{k=-\infty}^{\infty} E_k\,, \qquad E_k = \tfrac{1}{2}|a_k|^2\,, \tag{103}$$

and explicitly invariant term by term under translations (81) and reflections (76).

Take time derivative of the energy density (102), substitute (73) and integrate by parts. Total derivatives vanish by the spatial periodicity on the L domain:

$$\begin{aligned} \dot{E} &= \langle u_t\, u\rangle = -\left\langle \left(u^2/2 + u\, u_x + u\, u_{xxx}\right)_x u\right\rangle \\ &= \left\langle u_x\, u^2/2 + {u_x}^2 + u_x\, u_{xxx}\right\rangle . \end{aligned} \tag{104}$$

The first term in (104) vanishes by integration by parts, $3\left\langle u_x\, u^2\right\rangle = \left\langle (u^3)_x\right\rangle = 0$, and integrating the third term by parts yet again one gets [42] that the energy variation is

$$\dot{E} = P - D\,, \qquad P = \left\langle {u_x}^2\right\rangle , \quad D = \left\langle {u_{xx}}^2\right\rangle . \tag{105}$$

The power P pumped in by anti-diffusion u_{xx} is balanced by the energy dissipation rate D due hyper-viscosity u_{xxxx} in the KS equation (73).

The time averaged energy density $\overline{E}$ computed on a typical orbit goes to a constant, so the expectation values (106) of drive and dissipation exactly balance each out:

$$\overline{\dot{E}} = \lim_{t\to\infty}\frac{1}{t}\int_0^t d\tau\, \dot{E} = \overline{P} - \overline{D} = 0\,. \tag{106}$$

In particular, the equilibria and relative equilibria fall onto the diagonal in Figure 32, and so do time averages computed on periodic orbits and relative periodic orbits:

$$\overline{E}_p = \frac{1}{T_p}\int_0^{T_p} d\tau\, E(\tau)\,, \qquad \overline{P}_p = \frac{1}{T_p}\int_0^{T_p} d\tau\, P(\tau) = \overline{D}_p\,. \tag{107}$$

In the Fourier basis (103) the conservation of energy on average takes form

$$0 = \sum_{k=-\infty}^{\infty} (q_k^2 - q_k^4)\,\overline{E}_k\,, \qquad E_k(t) = \tfrac{1}{2}|a_k(t)|^2\,. \tag{108}$$

The large k convergence of this series is insensitive to the system size L; $\overline{E_k}$ have to decrease much faster than q_k^{-4}. Deviation of E_k from this bound for small k determines the active modes. For equilibria the L-independent bound on E is given by Michaelson [68]. The best current bound [36; 6] on the long-time limit of E as a function of the system size L scales as $E \propto L^2$.

One can go on constructing similar quantities in order to obtain a symmetry invariant basis for the system by considering higher moments. Yet, the procedure is tedious and the physical significance of higher moments unclear so we will not pursue this further. We will nevertheless use the E, P and D basis for visualization in Chapter 7 to emphasize both its utility as a readily available symmetry invariant representation and its limitations and need for a better basis.

CHAPTER VI

SIMULATING THE KURAMOTO-SIVASHINSKY SYSTEM

6.1 Numerical integration

Truncating the infinite tower of equations (79) by setting $a_k = 0$ for $k > N$ allows one to numerically integrate it. There are three technical issues that need some attention in order to accurately and efficiently simulate Kuramoto-Sivashinsky: evaluation of the nonlinear part, number of modes retained and stiffness.

6.1.1 Pseudospectral method

The linear part of Kuramoto-Sivashinsky equation is conveniently diagonal in the Fourier basis, see (79). The nonlinear part can be evaluated directly from the finite order truncation of (79), see Sect. 6.2 for an implementation. By using a pseudo-spectral method though, one can take advantage of the efficiency of the Fast Fourier Transform in evaluating the nonlinear part. For Kuramoto-Sivashinsky equation this is done by applying a discrete Fourier transform to (73) and taking into account that the Fourier operator is linear so that we can rewrite (79) in the following way

$$\dot{a}_k = (q_k^2 - q_k^4)\, a_k - i\frac{q_k}{2}\mathcal{F}\left[\left(\mathcal{F}^{-1}\left[a\right]\right)^2\right]_k , \tag{109}$$

where $\mathcal{F}$ is the discrete Fourier transform,

$$a_k = \mathcal{F}[u]_k = \sum_{n=0}^{N-1} u(x_n) e^{-iq_k x_n} , \qquad u(x_n) = \mathcal{F}^{-1}[a]_n = \frac{1}{N}\sum_{k=0}^{N-1} a_k e^{iq_k x_n} , \tag{110}$$

with $x_n = 2\pi\tilde{L}n/N$ and $a_{N-k} = a_k^*$ from the reality condition (80) and thus calculation of the discrete Fourier transform involves $N-1$ real variables.

Since we have set $a_0 = 0$ to eliminate Galilean invariance and the modes with $k < 0$ are redundant from (80), we can evaluate then nonlinear part in (79) in $N/2-1$ complex variables. The operation would correspond to multiplication of a real $(N-2)\times(N-2)$ matrix by a $N-2$-dimensional vector, while calculating just the forward Fourier transform would require the multiplication of a $(N-1)\times(N-1)$ matrix by a $N-1$-dimensional vector. In any case the operation count is $\mathrm{O}(N^2)$, but with the pseudo-spectral method we need two of them. The power of the pseudo-spectral method lies in the existence of the Fast Fourier Transform (FFT) algorithm that performs the discrete Fourier transform in $\mathrm{O}(Nlog_2N)$ operations therefore providing substantial performance advantage to the pseudo-spectral method. The FFT algorithm has been rediscovered many times, apparently starting with Gauss, see ref. [71] for references and a presentation of the algorithm. In our implementation we have used the FFTW package ref. [33].

6.1.2 Stiffness

The second issue one has to deal with in integrating (79) is due to the linear part. The term k^4 that appears in the linear part means that the timescales on which the first and the N'th

mode evolve is very different even for N of the order of 10. This is termed stiffness, see ref. [71] for a nice discussion. In practice, unless taken care of by the integration method, it forces us to follow the evolution of the equation in the fastest time-scale in order to maintain stability of the integration routine, thus imposing an impractically small stepsize. There are different approaches to dealing with stiffness, see ref. [53] for a comparison of algorithms that can be used to integrate stiff PDEs.

The algorithm that we have found very efficient and accurate in our numerical explorations is Exponential Time Differencing with fourth order Runge-Kutta timesteping (ETDRK4) introduced in ref. [16] and further developed in ref. [53], which we have followed in our implementation. The essence of the method is that it treats the linear and nonlinear part separately, applying an integrating factor to the linear part to eliminate the effect of stiffness.

As the method requires the computation of prefactors that depend on the linear part of the equation, we found it inconvenient to implement an adaptive stepsize control. Instead, we check the results of integration against decreasing the timestep, especially the robustness of relative periodic and periodic orbits found in Chapter 7.

6.1.3 Truncation

Another decision one has to make is how many modes to retain in (109). One has to keep in mind that we want accurate solutions to the original PDE, we do not just consider a truncation to finite N on its own right. Due to the hyperviscous damping u_{xxxx}, long time solutions of KS equation are smooth, a_k drop off fast with k, and truncations of (79) to $16 \leq N \leq 128$ terms yield accurate solutions for system sizes considered here. Robustness of the long-time dynamics of KS as a function of the number of Fourier modes kept in truncations of (79) is, however, a subtle issue. Adding an extra mode to a truncation of the system introduces a small perturbation in the space of dynamical systems. However, due to the lack of structural stability both as a function of truncations N, and the system size $\tilde{L}$, a small variation in a system parameter can (and often will) throw the dynamics into a different asymptotic state. For example, asymptotic attractor which appears to be chaotic in a N-dimensional phase space truncation can collapse into an attractive cycle for $(N+1)$-dimensions. Therefore we always evaluate the robustness of our results by increasing the number of modes. For instance, when we compute an unstable periodic orbit we check that its period and stability eigenvalues remain within the desired accuracy when recomputed in a higher-dimensional truncation.

For system size $L = 22$ all results presented here were computed using a 128-point spatial discretization, corresponding to $N = 64$ complex Fourier modes (with $a_0 = 0$ though). Note that going back and forth in Fourier and physical space in (109) one has to worry about the effect of aliasing on the results of the integration. Since our computations are relatively cheap we circumvent this difficulty by keeping enough modes so that at least half of the modes remain close to zero during a calculation. We also confirm our results against direct evaluation of the truncation of (79), see Sect. 6.2.

6.2 Calculating stability of equilibria

To calculate stability of equilibrium, the matrix

$$A(a_q) = \left.\frac{\partial v}{\partial a}\right|_{a=a_q} \tag{111}$$

has to be evaluated, either numerically or analytically. In Kuramoto-Sivashinsky we can obtain $A(a_q)$ efficiently for numerical purposes by using the linearity of the Fourier transform, as we did to get (109), see ref. [21].

In what follows we derive an analytical expression for it, as one might find it useful for the study of bifurcation problems, or, in our case, to cross-check the results of the pseudo-spectral method. To do so, we have to split Kuramoto-Sivashinsky equation into real and imaginary parts. Truncating the infinite tower of equations (79) by setting $a_k = 0$ for $k > N$, using the identity (80) and splitting the resulting equations into real and imaginary part by setting $a_k = b_k + ic_k$, we have

$$\begin{aligned}
\dot{b}_k &= q_k^2\left(1-q_k^2\right) b_k \\
&\quad + \frac{q_k}{2}\left(\sum_{m=1}^{k-1} c_m b_{k-m} + \sum_{m=k+1}^{N} c_m b_{m-k} - \sum_{m=1}^{N-k} c_m b_{k+m}\right) \\
&\quad + \frac{q_k}{2}\left(\sum_{m=1}^{k-1} b_m c_{k-m} - \sum_{m=k+1}^{N} b_m c_{m-k} + \sum_{m=1}^{N-k} b_m c_{k+m}\right)
\end{aligned} \tag{112}$$

$$\begin{aligned}
\dot{c}_k &= q_k^2\left(1-q_k^2\right) c_k \\
&\quad + \frac{q_k}{2}\left(\sum_{m=1}^{k-1} c_m c_{k-m} - \sum_{m=k+1}^{N} c_m c_{m-k} - \sum_{m=1}^{N-k} c_m c_{k+m}\right) \\
&\quad - \frac{q_k}{2}\left(\sum_{m=1}^{k-1} b_m b_{k-m} + \sum_{m=k+1}^{N} b_m b_{m-k} + \sum_{m=1}^{N-k} b_m b_{k+m}\right)
\end{aligned} \tag{113}$$

where now only terms c_k, b_k with $0 < k < N$ appear. Observe that

$$\sum_{m=1}^{N-k} c_m b_{k+m} = \sum_{m=k+1}^{N} b_m c_{m-k}\,, \tag{114}$$

etc. and thus (112) and (113) simplify to

$$\begin{aligned}
\dot{b}_k &= q_k^2\left(1-q_k^2\right) b_k \\
&\quad + \frac{q_k}{2}\left(\sum_{m=1}^{k-1} c_m b_{k-m} - 2\sum_{m=1}^{N-k} c_m b_{k+m}\right) \\
&\quad + \frac{q_k}{2}\left(\sum_{m=1}^{k-1} b_m c_{k-m} + 2\sum_{m=1}^{N-k} b_m c_{k+m}\right)
\end{aligned} \tag{115}$$

$$\begin{aligned}
\dot{c}_k &= q_k^2\left(1-q_k^2\right) c_k \\
&\quad + \frac{q_k}{2}\left(\sum_{m=1}^{k-1} c_m c_{k-m} - 2\sum_{m=1}^{N-k} c_m c_{k+m}\right) \\
&\quad - \frac{q_k}{2}\left(\sum_{m=1}^{k-1} b_m b_{k-m} + 2\sum_{m=1}^{N-k} b_m b_{k+m}\right)\,.
\end{aligned} \tag{116}$$

As discussed in Sect. 6.1.1 such expressions are not as efficient as using a pseudo-spectral implementation, but we use them for comparison purposes, to detect possible issues in our pseudo-spectral integrator due to aliasing or the FFT implementation.

To calculate the matrix $A_{ij}(a) \equiv \frac{\partial v_i(x)}{\partial x_j}$ we need to consider the four matrices $\frac{\partial \dot{b}_k}{\partial b_j}$, $\frac{\partial \dot{b}_k}{\partial c_j}$, $\frac{\partial \dot{c}_k}{\partial b_j}$, $\frac{\partial \dot{c}_k}{\partial c_j}$. We begin with

$$\frac{\partial \dot{c}_k}{\partial c_j} = q_k^2 \left(1 - q_k^2\right) \delta_{kj} - \frac{q_k}{2} \frac{\partial}{\partial c_j} \left(\sum_{m=1}^{k-1} c_m c_{k-m} - 2 \sum_{m=1}^{N-k} c_m c_{k+m} \right) . \tag{117}$$

Conceder the second term:

$$\begin{aligned} -\frac{q_k}{2} \frac{\partial}{\partial c_j} \left(\sum_{m=1}^{k-1} c_m c_{k-m} - 2 \sum_{m=1}^{N-k} c_m c_{k+m} \right) &= -\frac{q_k}{2} \sum_{m=1}^{k-1} \left(\delta_{m,j} c_{k-m} + c_m \delta_{k-m,j}\right) \\ &\quad + q_k \sum_{m=1}^{N-k} \left(\delta_{m,j} c_{k+m} + c_m \delta_{k+m,j}\right) \end{aligned} \tag{118}$$

We need to consider two cases separately:

- $k \leq j$

$$\begin{aligned} -\frac{q_k}{2} \frac{\partial}{\partial c_j} \left(\sum_{m=1}^{k-1} c_m c_{k-m} - 2 \sum_{m=1}^{N-k} c_m c_{k+m} \right) &= -\frac{q_k}{2}(0+0) + q_k(c_{k+j} + c_{j-k}) \\ &= q_k(c_{k+j} - c_{k-j}) \end{aligned} \tag{119}$$

- $k > j$

$$\begin{aligned} -\frac{q_k}{2} \frac{\partial}{\partial c_j} \left(\sum_{m=1}^{k-1} c_m c_{k-m} - 2 \sum_{m=1}^{N-k} c_m c_{k+m} \right) &= -\frac{q_k}{2}(c_{k-j} + c_{k-j}) + q_k(c_{k+j} + 0) \\ &= q_k(c_{k+j} - c_{k-j}) \end{aligned} \tag{120}$$

and thus

$$\frac{\partial \dot{c}_k}{\partial c_j} = q_k^2 \left(1 - q_k^2\right) + q_k(c_{k+j} - c_{k-j}) \tag{121}$$

Following the above procedure

$$\frac{\partial \dot{c}_k}{\partial b_j} = q_k(b_{k+j} + b_{k-j}) , \tag{122}$$

$$\frac{\partial \dot{b}_k}{\partial b_j} = q_k^2 \left(1 - q_k^2\right) \delta_{kj} - q_k(c_{k+j} + c_{k-j}) , \tag{123}$$

$$\frac{\partial \dot{b}_k}{\partial c_j} = q_k(b_{k+j} - b_{k-j}) . \tag{124}$$

6.3 Shooting for relative periodic orbits

In this section we describe how we obtain relative periodic orbits from initial guesses for points on them. This is by no means the only or the most efficient method, but it is easy to implement and suffices to find the Kuramoto-Sivashinsky orbits in Sect. 7.1. A different approach that does not need auxiliary conditions is given in refs. [21; 17], and yet another one that is designed to be compatible with the continuation package AUTO, is given in ref. [7]. For an introduction to methods for locating periodic orbits a good place to start is ref. [20]. The formulation of the auxiliary conditions for the multiple-shooting method presented here draws from ref. [80]. Here we will present the one-parameter Lie group case. The generalization to multi-parameter groups and other systems is straightforward.

6.3.1 Multipoint shooting for relative periodic orbits

Assume that we have an initial guess for a relative periodic orbit of period T_p and phase shift ϕ_p. Let the guess be given as N initial conditions x_i, $i = 1 \dots N$ for each segment of the relative periodic orbit, along with the flight times T_i, such that $\sum_i^N T_i = T_p$, and the phase shift ϕ_p. For the true relative periodic orbit we have

$$\begin{aligned} f^{\tilde{T}_i}(\tilde{x}_i) &= \tilde{x}_{i+1}\,, \ i = 1, \dots N-1, \\ R(\tilde{\phi}_p) f^{\tilde{T}_N}(\tilde{x}_N) &= \tilde{x}_1\,. \end{aligned} \tag{125}$$

Assuming that our guess is in the linear neighborh of the relative periodic orbit we can Taylor expand (125) around the guess to linear order in the small quantities $\Delta x_i = \tilde{x}_i - x_i$, $\Delta T_i = \tilde{T}_i - T_i$, $\Delta\phi_p = \tilde{\phi}_p - \phi_p$ to get

$$\begin{aligned} J^{T_i}(x_i)\Delta x_i + v_{T_i}\Delta T_i - \Delta x_{i+1} &= x_{i+1} - f^{T_i}(x_i) \\ R(\phi_p)J^{T_N}(x_N)\Delta x_N + R(\phi_p)v_{T_N}\Delta T_N + \mathfrak{a}R(\phi_p)f^{T_N}(x_N)\Delta\phi - \Delta x_1 &= x_1 - R(\phi_p)f^{T_N}(x_N)\,, \end{aligned} \tag{126}$$

where v_{T_i} denotes v evaluated at $f^{T_i}(x_i)$, $\mathfrak{a}$ denotes the generator of the group and the matrix

$$J^t(x_i) = \frac{\partial f^t(x_i)}{\partial x} \tag{127}$$

is evaluated by integrating, along with the flow, the equation

$$\dot{J}^t = AJ^t\,, \tag{128}$$

with initial condition $J^0 = \mathbf{1}$. Interpreting Δx_i, ΔT_i, $\Delta\phi_p$ as corrections to our guess solution we iteratively improve our approximation of $\tilde{x}_p$. To exclude variations along the two unit eigendirections of $R(\tilde{\phi}_p)J^{\tilde{T}_p}(\tilde{x})$ we impose the conditions

$$v(x_i)\cdot\Delta x_i = 0\,, \tag{129}$$

$$(\mathfrak{a}x_N)\cdot\Delta x_N = 0\,. \tag{130}$$

Conditions (129) ensures that the correction will be transverse to the eigendirection associated with time translational invariance, while condition (129) prohibits correction

along the direction of infinitesimal group action. In matrix form we have the system

$$
\left(\begin{array}{cccc|c|c}
\mathbf{J}^{T_1}(x_1) & \mathbf{-1} & & & v_{T_1} & \\
 & \ddots & & & \ddots & \\
 & & \mathbf{-1} & & & \\
 & & \mathbf{J}^{T_i}(x_i) & \mathbf{-1} & v_{T_i} & \\
 & & & \ddots & \ddots & \\
 & & & \mathbf{-1} & & \\
\mathbf{-1} & & & R(\phi_p)\mathbf{J}^{T_N}(x_N) & R(\phi_p)v_{T_N} & \mathfrak{a}R(\phi_p)f^{T_N}(x_N) \\
\hline
v(x_1) & & & & & \\
 & \ddots & & & & \\
 & & v(x_i) & & & \\
 & & & \ddots & & \\
 & & & & v(x_N) & \\
\hline
 & & & \mathfrak{a}x_N & &
\end{array}\right)
\left(\begin{array}{c}
\Delta x_1 \\ \vdots \\ \Delta x_i \\ \vdots \\ \Delta x_N \\ \Delta T_1 \\ \vdots \\ \Delta T_i \\ \vdots \\ \Delta T_N \\ \Delta\phi
\end{array}\right)
$$

$$
= \left(\begin{array}{c}
x_2 - f^{T_1}(x_1) \\ \vdots \\ x_{i+1} - f^{T_i}(x_i) \\ \vdots \\ x_1 - R(\phi_p)f^{T_N}(x_N) \\ 0 \\ \\ \\ \vdots \\ \\ \\ 0
\end{array}\right).
$$

Solving this linear system and iterating the procedure we refine the initial guess to desired accuracy, provided the initial guess is sufficiently close to the true solution. If we are in the linear neighborh of the solution we are guarranted to find it. In practice we can increase the chances of convergence by taking more segments along the orbit. The limit of $N \to \infty$ leads one to consider variational methods, see for example refs. [78; 59].

By setting $N = 1$ in (126) we observe that we have to interprete $R(\phi_p)J^{T_p}(x_p)$ as the fundamental matrix for relative periodic orbits, with eigenvalues playing the role of Floquet multipliers.

CHAPTER VII

KURAMOTO-SIVASHINSKY PHASE SPACE

In this chapter we explore numerically the phase space of the Kuramoto-Sivashinsky system for $L = 22$ system size. The results presented are a collaborative effort with P. Cvitanović and R.L. Davidchack [21].

7.1 Geometry of $L = 22$ phase space

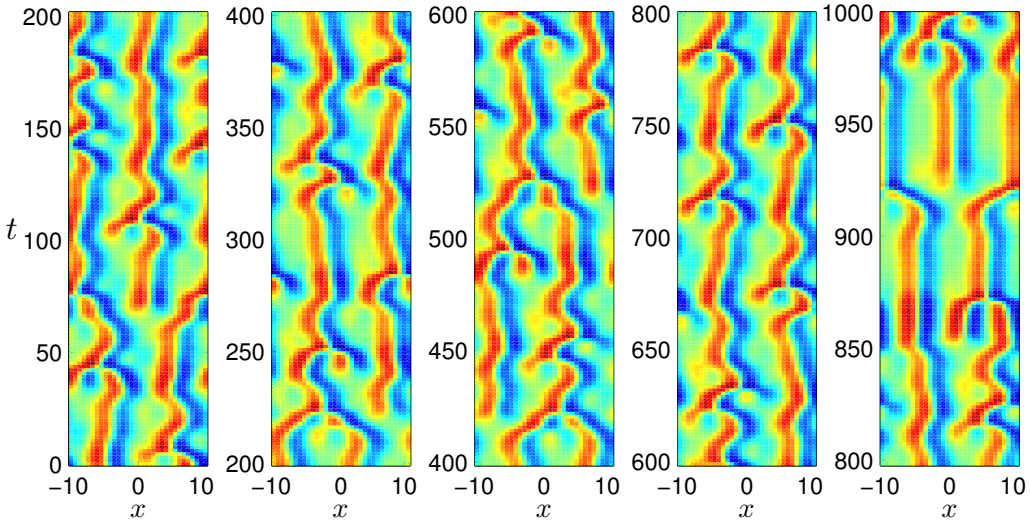

Figure 20: A typical chaotic orbit of the Kuramoto-Sivashinsky flow, system size $L = 22$.

We now turn to exploring Hopf's vision numerically, on a specific Kuramoto-Sivashinsky system of size $L = 22$. For this system size the competition between states with wavenumbers 2 and 3 leads to the empirically observed 'sustained turbulence.' A typical long orbit is shown in Figure 20.

Because of the strong k^4 contraction, for a small system size one expects that the long-time dynamics is confined to low-dimensional inertial manifold. Indeed, numerically the leading Lyapunov exponents of the $L = 22$ chaotic attractor are

$$(\lambda_i) = (0.048, 0, 0, -0.003, -0.189, -0.256, -0.290, \cdots)\,,$$

so the chaotic dynamics mostly takes place close to a 4-dimensional manifold, with strong contraction in other dimensions. The two zero exponents are due to the time [43] and space translational symmetries of the Kuramoto-Sivashinsky equation, and it was shown in refs. [14; 60] that within particular curvilinear coordinate frames, the dynamics on the attractor can sometimes be reduced to local 1- or 2-dimensional maps. Hence a relatively small number of Fourier modes, typically 128 used in numerical calculations presented here, suffices to obtain numerically accurate (within 10^{-5}) invariant solutions.

We next investigate the properties of equilibria and relative equilibria and determine numerically a large set of the short periods relative periodic orbits for KS in a periodic cell of size $L = 22$.

7.1.1 Equilibria and relative equilibria

In addition to the trivial equilibrium $u = 0$ (denoted E_0), we find three equilibria with dominant wavenumber k (denoted E_k) for $k = 1, 2, 3$. All equilibria, shown in Fig. 21, are symmetric with respect to the reflection symmetry (76). In addition, E_2 and E_3 are symmetric with respect to translation (77), by $L/2$ and $L/3$, respectively. E_2 and E_3 essentially lie, respectively, in the 2^{nd} and 3^{rd} Fourier component complex plane, with small $k = 2j$, $k = 3j$ harmonics deformations.

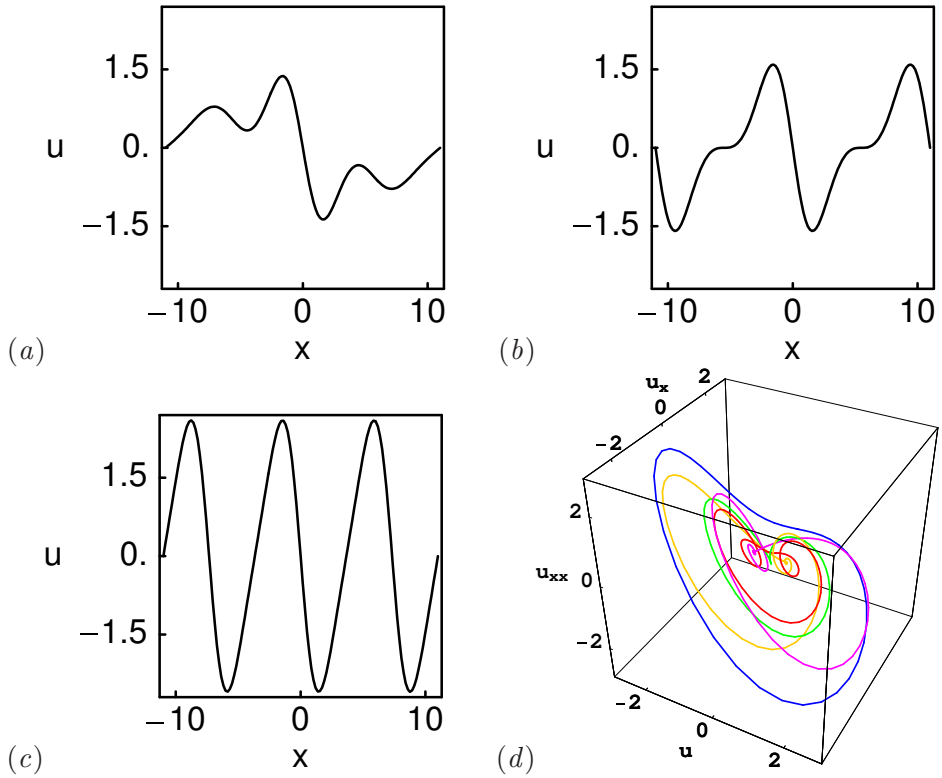

Figure 21: (a) E_1, (b) E_2, and (c) E_3 equilibria. The E_0 equilibrium is the $u(x) = 0$ solution. (d) (u, u_x, u_{xx}) representation of (red) E_1, (green) E_2, (blue) E_3 equilibria, (purple) TW_{+1}, and (orange) TW_{-1} relative equilibria. $L = 22$ system size.

The stability of the equilibria is characterized by the eigenvalues $\lambda^{(j)}$ of the stability matrix. The leading 10 eigenvalues for each equilibrium are listed in Table 1. We have computed (available upon request) the corresponding eigenvectors as well. As an equilibrium with $\mathrm{Re}\,\lambda_j > 0$ is unstable in the direction of the corresponding eigenvector $\mathbf{e}^{(j)}$, the eigenvectors provide flow-intrinsic (PDE discretization independent) coordinates which we use for visualization of unstable manifolds and homo/heteroclinic connections between equilibria.

The eigenvalues of E_0 are determined by the linear part of the KS equation (79): $\lambda_k =$

$(k/\tilde{L})^2-(k/\tilde{L})^4$. For $L = 22$, there are three pairs of unstable eigenvalues, corresponding, in decreasing order, to three unstable modes $k = 2, 3$, and 1. For each mode, the corresponding eigenvectors lie in the plane spanned by Re a_k and Im a_k. Table 1 lists the symmetries of the eigenvectors of equilibria E_1 to E_3.

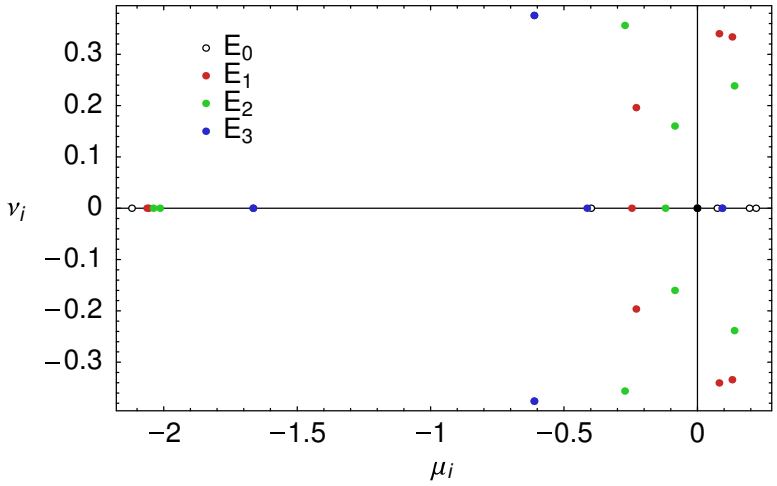

Figure 22: Leading equilibrium stability eigenvalues, $L = 22$ system size.

Consistent with the bifurcation diagram of Figure 19, we find two pairs of relative equilibria (87) with velocities $c = \pm 0.73699$ and ± 0.34954 which we label $TW_{\pm 1}$ and $TW_{\pm 2}$, for 'traveling waves.' The profiles of the two relative equilibria and their time evolution with eventual decay into the chaotic attractor are shown in Figure 23. The leading eigenvalues of $TW_{\pm 1}$ and $TW_{\pm 2}$ are listed in Table 1; those with $\mu > -2.5$ are also plotted in Figure 22.

Table 2 lists equilibrium energy E, the local Poincaré section return time T, radially expanding Floquet multiplier Λ_e, and the least contracting Floquet multiplier Λ_c for all $L = 22$ equilibria and relative equilibria. The return time $T = 2\pi/\omega^{(e)}$ is given by the imaginary part of the leading complex eigenvalue of a given equilibrium or relative equilibrium, the expansion multiplier per one turn of the most unstable spiral-out by $\Lambda_e \approx \exp(\mu^{(e)}T)$, and the contraction rate along the slowest contracting stable eigendirection by $\Lambda_c \approx \exp(\mu^{(c)}T)$. We learn that the shortest 'turn-over' time is $\approx 10-20$, and that if there exist horseshoe sets of unstable periodic orbits associated with these equilibria, they have unstable multipliers of order of $\Lambda_e \sim 5-10$, and that they are surprisingly thin in the folding direction, with contracting multipliers of order of 10^{-2}, as also observed in ref. [60].

7.1.1.1 Unstable manifolds of equilibria and their heteroclinic connections

As shown in Table 1, the E_1 equilibrium has two unstable planes within which the solutions are spiralling out (i.e., two pairs of complex conjugate eigenvalues). The E_2 has one such plane, while the E_3 has two real positive degenerate eigenvalues, so the solutions are moving radially away from the equilibrium within the plane spanned by the corresponding eigenvectors.

To construct an invariant manifold containing solutions corresponding to the pair of unstable complex conjugate eigenvalues, $\lambda = \mu \pm i\omega$, $\mu > 0$, we start with a set of initial

Table 1: Leading eigenvalues $\lambda^{(j)} = \mu^{(j)} \pm i\omega^{(j)}$ and symmetries of the corresponding eigenvectors of KS equilibria and relative equilibria for $L = 22$ system size. We have used as our reference states the ones that lie within the antisymmetric subspace $\mathrm{Fix}\,(\mathrm{D}_1)$, and also listed the symmetries of the $L/4$ translated ones.

E_1	$\mu^{(j)}$	$\omega^{(j)}$	Symmetry	$\tau_{1/4}\mathrm{E}_n$ Symmetry
$\lambda^{(1,2)}$	0.1308	0.3341	-	-
$\lambda^{(3,4)}$	0.0824	0.3402	$\mathrm{Fix}\,(\mathrm{D}_1)$	$\tau_{1/4}\mathrm{Fix}\,(\mathrm{D}_1)$
$\lambda^{(5)}$	0		-	-
$\lambda^{(6,7)}$	−0.2287	0.1963	$\mathrm{Fix}\,(\mathrm{D}_1)$	$\tau_{1/4}\mathrm{Fix}\,(\mathrm{D}_1)$
$\lambda^{(8)}$	−0.2455		-	-
$\lambda^{(9)}$	−2.0554		$\mathrm{Fix}\,(\mathrm{D}_1)$	$\tau_{1/4}\mathrm{Fix}\,(\mathrm{D}_1)$
$\lambda^{(10)}$	−2.0619		-	-
E_2				
$\lambda^{(1,2)}$	0.1390	0.2384	$\mathrm{Fix}\,(\mathrm{D}_1)$	$\tau_{1/4}\mathrm{Fix}\,(\mathrm{D}_1)$
$\lambda^{(3)}$	0		$\tau_{1/2}$	$\tau_{1/2}$
$\lambda^{(4,5)}$	−0.0840	0.1602	$\tau_{1/4}\mathrm{Fix}\,(\mathrm{D}_1)$	$\mathrm{Fix}\,(\mathrm{D}_1)$
$\lambda^{(6)}$	−0.1194		$\tau_{1/2}$	$\tau_{1/2}$
$\lambda^{(7,8)}$	−0.2711	0.3563	$\mathrm{Fix}\,(\mathrm{D}_1)\,,\ \tau_{1/4}\mathrm{Fix}\,(\mathrm{D}_1)\,,\ \tau_{1/2}$	$\mathrm{Fix}\,(\mathrm{D}_1)\,,\ \tau_{1/4}\mathrm{Fix}\,(\mathrm{D}_1)\,,\ \tau_{1/2}$
$\lambda^{(9)}$	−2.0130		$\tau_{1/4}\mathrm{Fix}\,(\mathrm{D}_1)$	$\mathrm{Fix}\,(\mathrm{D}_1)$
$\lambda^{(10)}$	−2.0378		$\mathrm{Fix}\,(\mathrm{D}_1)$	$\tau_{1/4}\mathrm{Fix}\,(\mathrm{D}_1)$
E_3				
$\lambda^{(1)}$	0.0933		$\mathrm{Fix}\,(\mathrm{D}_1)$	$\tau_{1/4}\mathrm{Fix}\,(\mathrm{D}_1)$
$\lambda^{(2)}$	0.0933		-	-
$\lambda^{(3)}$	0		$\tau_{1/3}$	$\tau_{1/3}$
$\lambda^{(4)}$	−0.4128		$\mathrm{Fix}\,(\mathrm{D}_1)\,,\ \tau_{1/3}$	$\tau_{1/4}\mathrm{Fix}\,(\mathrm{D}_1)\,,\ \tau_{1/3}$
$\lambda^{(5,6)}$	−0.6108	0.3759	$\mathrm{Fix}\,(\mathrm{D}_1)$	$\tau_{1/4}\mathrm{Fix}\,(\mathrm{D}_1)$
$\lambda^{(7,8)}$	−0.6108	0.3759	-	-
$\lambda^{(9)}$	−1.6641		-	-
$\lambda^{(10)}$	−1.6641		$\mathrm{Fix}\,(\mathrm{D}_1)$	$\tau_{1/4}\mathrm{Fix}\,(\mathrm{D}_1)$
$\mathrm{TW}_{\pm 1}$				
$\lambda^{(1,2)}$	0.1156	0.8173	-	-
$\lambda^{(3,4)}$	0.0337	0.4189	-	-
$\lambda^{(5)}$	0		-	-
$\lambda^{(6)}$	−0.2457		-	-
$\lambda^{(7,8)}$	−0.3213	0.9813	-	-
$\mathrm{TW}_{\pm 2}$				
$\lambda^{(1)}$	0.3370		-	-
$\lambda^{(2)}$	0		-	-
$\lambda^{(3,4)}$	−0.0096	0.6288	-	-
$\lambda^{(5,6)}$	−0.2619	0.5591	-	-
$\lambda^{(7,8)}$	−0.3067	0.0725	-	-

conditions near equilibrium E_k,

$$a(0) = a_{\mathrm{E}_k} + \epsilon\, \exp(\delta)\mathbf{e}^{(j)}\,, \tag{131}$$

where δ takes the set of values uniformly distributed in the interval $[0, 2\pi\mu/\omega]$, $\mathbf{e}^{(j)}$ is a unit vector in the unstable plane, and $\epsilon > 0$ is small.

The manifold starting within the first unstable plane of E_1, with eigenvalues $0.1308 \pm$

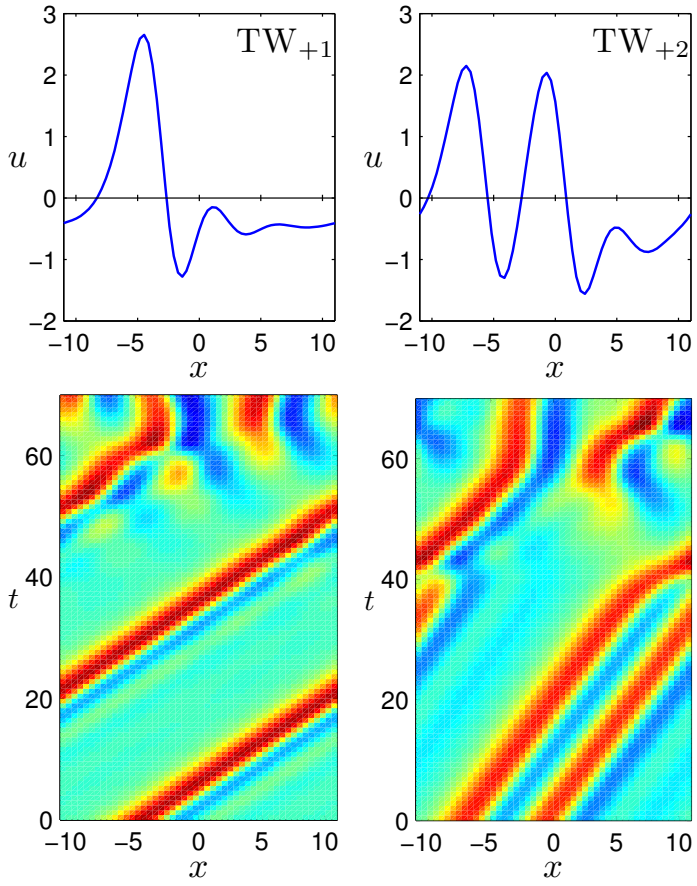

Figure 23: Relative equilibria: TW_{+1} with velocity $c = 0.737$ and TW_{+2} with velocity $c = 0.350$. The upper panels show the relative equilibria profiles. The lower panels show evolution of slightly perturbed relative equilibria and their decay into generic turbulence. Each relative equilibrium has a reflection symmetric partner related by $u(x) \to -u(-x)$ travelling with velocity $-c$.

Table 2: Properties of equilibria and relative equilibria that determine the system dynamics in their vicinity. T is characteristic time scale of the dynamics, Λ_e and Λ_c are the leading expansion and contraction rates, and E is the energy (102).

	E	T	Λ_e	Λ_c
E_1	0.2609	18.81	4.79	0.04
E_2	0.4382	26.35	5.99	0.03
E_3	1.5876	10.71	9.92	0.01
$\mathrm{TW}_{\pm 1}$	0.4649			
$\mathrm{TW}_{\pm 2}$	0.6048			

$i\,0.3341$, is shown in Figure 24. It appears to fall directly into the chaotic attractor. The behavior of the manifold starting within the second unstable plane of E_1, eigenvalues $0.0824 \pm i\,0.3402$, is remarkably different: as can be seen in Figure 25, almost all orbits within

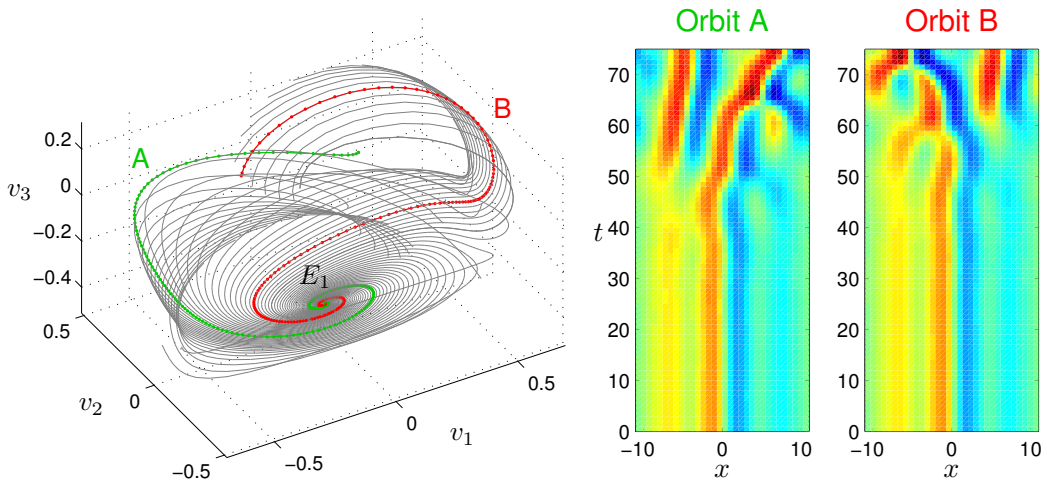

Figure 24: The left panel shows the unstable manifold of equilibrium E_1 starting within the plane corresponding to the first pair of unstable eigenvalues. The coordinate axes v_1, v_2, and v_3 are constructed from vectors Re $\mathbf{e}^{(1)}$, Im $\mathbf{e}^{(1)}$, and Re $\mathbf{e}^{(6)}$ by Gram-Schmidt orthogonalization. The right panel shows spatial representation of two orbits A and B. The change of color from blue to red indicates increasing values of $u(x)$.

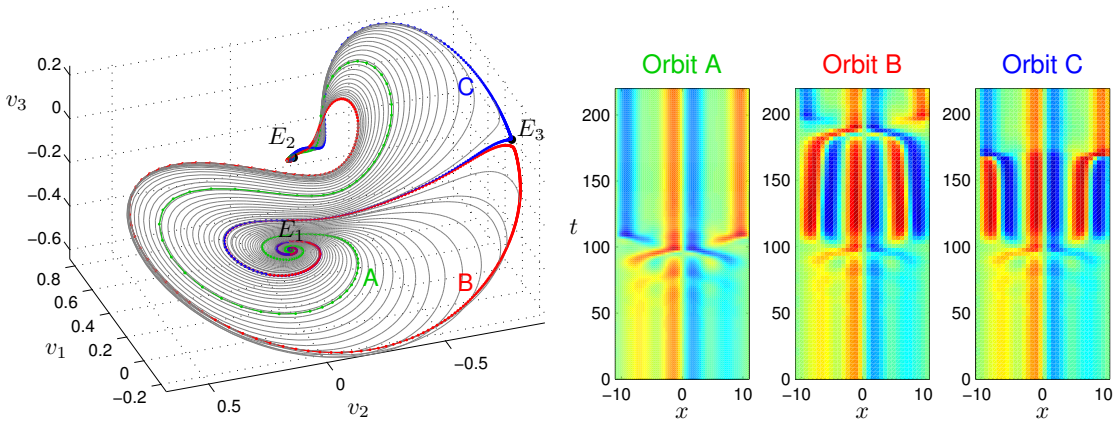

Figure 25: The left panel shows the unstable manifold of equilibrium E_1 starting within the plane corresponding to the second pair of unstable eigenvalues. The coordinate axes v_1, v_2, and v_3 are constructed from vectors Re $\mathbf{e}^{(3)}$, Im $\mathbf{e}^{(3)}$, and Re $\mathbf{e}^{(6)}$ by Gram-Schmidt orthogonalization. The right panel shows spatial representation of three orbits. Orbits B and C pass close to the equilibrium E_3.

the manifold converge to the equilibrium E_2. The manifold also contains a heteroclinic connection from E_1 to E_3, and is bordered by the $\lambda^{(1)}$-eigendirection unstable manifold of E_3.

The two-dimensional unstable manifold of E_2 is shown in Figure 26. All orbits within the manifold converge to E_2 shifted by $L/4$. So this manifold can be viewed as a homoclinic connection. It also contains a pair of heteroclinic connections from E_2 to E_3.

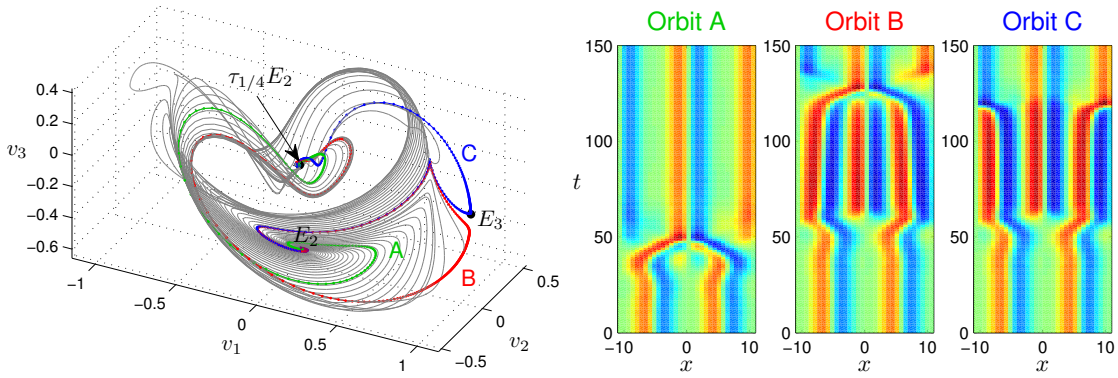

Figure 26: The left panel shows the two-dimensional unstable manifold of equilibrium E_2. The coordinate axes v_1, v_2, and v_3 are constructed from vectors Re $\mathbf{e}^{(1)}$, Im $\mathbf{e}^{(1)}$, and $\mathbf{e}^{(7)}$ by Gram-Schmidt orthogonalization. The right panel shows spatial representation of three orbits. Orbits B and C pass close to the equilibrium E_3. See Figure 27 for a different visualization.

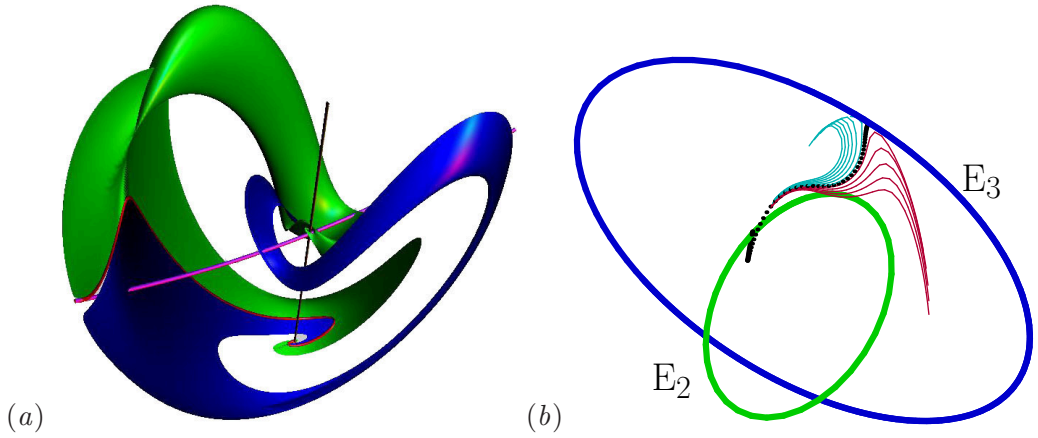

Figure 27: (a) (blue/green) The unstable manifold of E_2 equilibrium. (black line) The circle of E_2 equilibria related by the translation invariance. (purple line) The circle of E_3 equilibria. (red) The heteroclinic connection from the E_2 equilibrium to the E_3 equilibrium splits the manifold into two parts, colored (blue) and (green). See Figure 26 for a different visualization. (b) E_2 equilibrium to E_3 equilibrium heteroclinic connection. Here we omit the unstable manifold of E_2, keeping only a few neighboring trajectories in order to indicate the unstable manifold of E_3. The E_2 and E_3 families of equilibria arising from the continuous translational symmetry of KS on a periodic domain are indicated by the two circles.

The equilibrium E_3 has a pair of real unstable eigenvalues equal to each other. Therefore, within the plane spanned by the corresponding eigenvectors, the orbits move radially away from the equilibrium. In order to trace out the unstable manifold, we start with a set of initial conditions within the unstable plane

$$a(0) = a_{\mathrm{E}_3} + \epsilon(v_1 \cos\phi + v_2 \sin\phi)\,, \quad \phi \in [0, 2\pi]\,, \tag{132}$$

where v_1 and v_2 are orthonormal vectors within the plane spanned by the two unstable eigenvectors, seeded as in (131). The unstable manifold of E_3 is shown in Figure 28. The 3-fold symmetry of the manifold is related to the symmetry of E_3 with respect to translation by $L/3$. The manifold contains heteroclinic orbits connecting E_3 to three different points of the circle of equilibria E_2 translated set of solutions. Note also that the segments of orbits B and C between E_3 and E_2 in Figures 25 and 26 represent the same heteroclinic connections as orbits B and C in Figure 28.

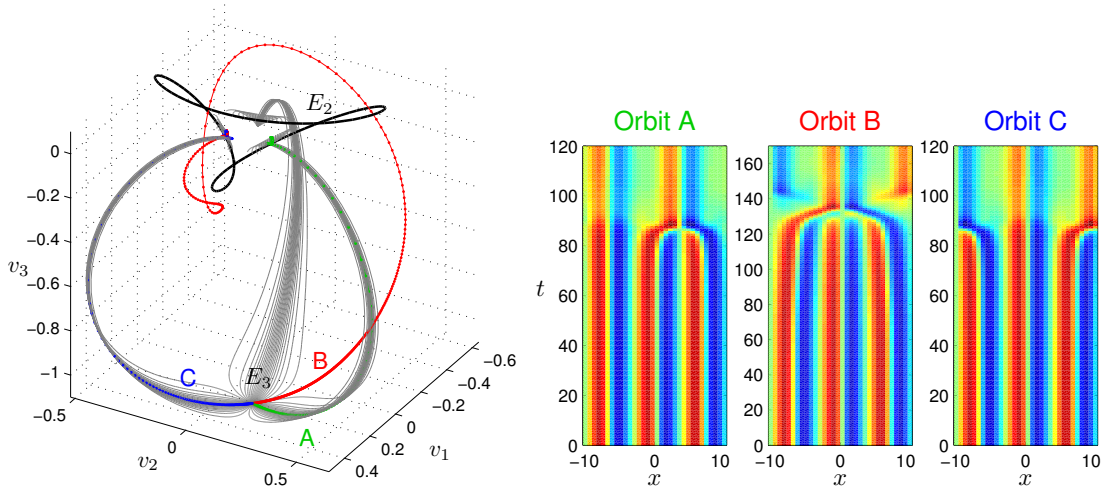

Figure 28: The left panel shows the two-dimensional unstable manifold of equilibrium E_3. The coordinate axes v_1, v_2, and v_3 are constructed from vectors $\mathbf{e}^{(1)}$, $\mathbf{e}^{(2)}$, and $\mathbf{e}^{(4)}$ by Gram-Schmidt orthogonalization. The black line shows a family of E_2 equilibria related by translational symmetry. The right panel shows spatial representation of three orbits. Orbits B and C are two different heteroclinic orbits connecting E_3 to the same point on the E_2 line.

An understanding of the ubiquity of heteroclinic connections in KSe, as opposed to their non-genericity in a general high-dimensional system, is provided in ref. [55]. For our system size there are exactly two representatives of the E_2 family that lie in the intersection of $\mathrm{Fix}\,(D_1)$ and $\tau_{1/4}\mathrm{Fix}\,(D_1)$ related to each other by an $L/4$ shift. Denote them by E_2 and $\tau_{1/4}E_2$ respectively. The unstable eigenplane of E_2 lies on $\mathrm{Fix}\,(D_1)$ while that of $\tau_{1/4}E_2$ lies on $\tau_{1/4}\mathrm{Fix}\,(D_1)$, *cf.* Table 1. The E_3 family members that live in $\mathrm{Fix}\,(D_1)$ have one of their unstable eigenvectors (the one related to the heteroclinic connection to E_2 family) on $\mathrm{Fix}\,(D_1)$, while the other does not lie on the symmetry-invariant subspace. Similarly, for the E_1 family we observe that the equilibria in $\mathrm{Fix}\,(D_1)$ have an unstable plane on $\mathrm{Fix}\,(D_1)$ (again related to the heteroclinic connection) and a second one with no symmetry. Thus $\tau_{1/4}E_2$ appears as a sink on $\mathrm{Fix}\,(D_1)$, while all other equilibria appear as sources. This explains the heteroclinic connections from E_1 , E_2 and E_3 to $\tau_{1/4}E_2$. By equivariance the dynamics within $\tau_{1/4}\mathrm{Fix}\,(D_1)$ must look the same and taking into account Table 1 we understand that within $\tau_{1/4}\mathrm{Fix}\,(D_1)$ we have connections from $\tau_{1/4}E_2$ (and members of E_1 and E_3 families) to E_2 and the formation of a heteroclinic loop. Due to the translational invariance of KS there is a heteroclinic loop for any two points of the E_2 family related by an $L/4$-shift.

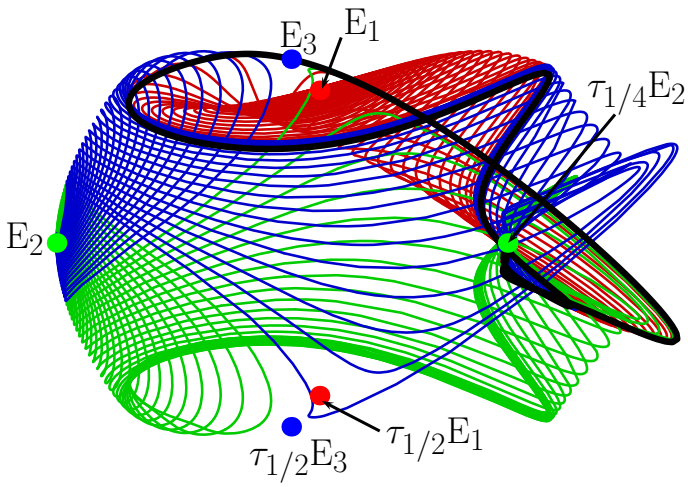

Figure 29: Heteroclinic connections on Fix (D$_1$): (red) The unstable manifold of E$_1$ equilibrium. (blue/green) The unstable manifold of E$_2$ equilibrium. (black) Heteroclinic connections from E$_3$ equilibrium to $\tau_{1/4}$E$_2$ equilibrium. The unstable manifolds of $\tau_{1/2}$E$_1$ and $\tau_{1/2}$E$_2$ have been ommited for clarity. Projection from 128 dimensions onto the plane given by the vectors E$_2 - \tau_{1/4}$E$_2$ and E$_3 - \tau_{1/2}$E$_3$.

7.1.2 Relative periodic orbits

The relative periodic orbits satisfy the condition (92) $u(x + \ell_p, T_p) = u(x, 0)$, where T_p is the period and ℓ_p the phase shift. We have limited our search to orbits with $T_p < 200$ and found over 300 relative periodic orbits with $\ell_p > 0$. Each relative periodic orbit with phase shift $\ell_p \neq 0$ has a reflection symmetric partner $u_p(x) \to -u_p(-x)$ with phase shift $-\ell_p$.

The search has not been exhaustive, and there are likely to be more orbits with $T_p < 200$. However, the orbits we have found provide a representative sample of typical periodic and relative periodic orbits and approximate well the chaotic attractor (since they were located using seeds obtained from close returns within the chaotic dynamics).

Figure 30 (a) shows the relative periodic orbits in the plane (T, ℓ). Not much is learned from such plot other than that for longer periods the relative periodic orbits are scattered over the whole (T, ℓ) plane.

The stability of the orbits is determined by their Floquet exponents, defined as

$$s_j = \mu^{(j)}/T_p\,, \tag{133}$$

where $\Lambda_j = e^{\mu^{(j)} \pm i\omega^{(j)}}$ are the eigenvalues of the fundamental matrix $\mathbf{g}(\ell_p)J(a_p, T_p)$ (see sec 6.3.1).

As was already the case for the Lyapunov exponents discussed in Sect. 7.1, for all periodic and relative periodic orbits we have found, only four Floquet exponents are dynamically relevant, with the remaining ones indicating strong contraction towards the 4-dimensional manifold containing the chaotic attractor. Out of the four leading exponents, two equal zero, due to the time and space translational invariance of the orbits. Of the remaining two, one is always positive, while the second one is either positive or negative.

The scatter of the largest Floquet exponents of periodic and relative periodic orbits is shown in Figure 30 (b). In this case some tendency of accumulation toward the largest

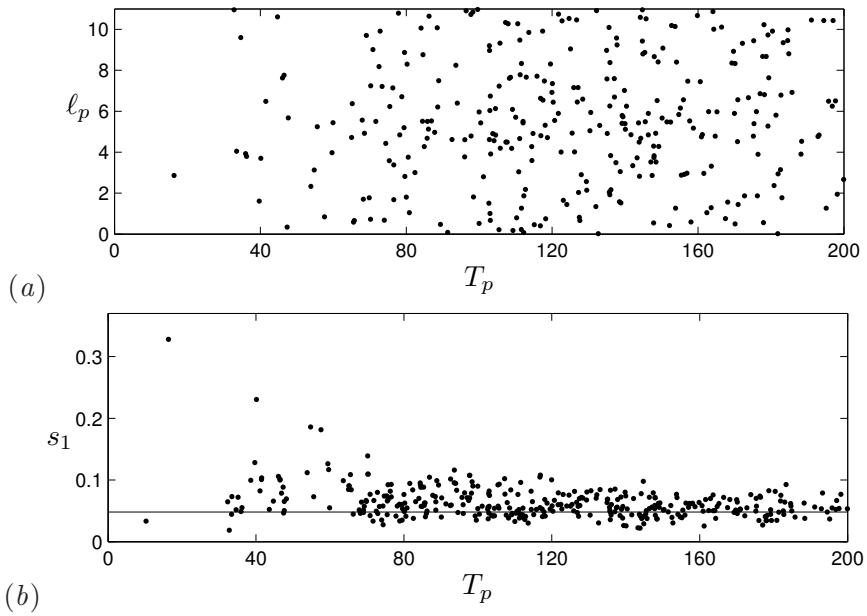

Figure 30: (a) All relative periodic orbits of Kuramoto-Sivashinsky system determined here, with periods T_p and shifts $\ell_p > 0$. (b) The largest Floquet exponents (133) of all relative periodic orbits and pre-periodic orbits with reflection. The horizontal line at 0.048 indicates the numerical value of the largest Lyapunov exponent of the chaotic attractor.

Floquet exponent 0.048 of the chaotic attractor can be noted. This, however, is in part an artifact of initializing the relative periodic orbit searches by near recurrences in long-time phase space trajectories.

The small period relative periodic orbits outline the coarse structure of the chaotic attractor, while the longer period relative periodic orbits resolve the finer details of the dynamics. The first four orbits with the shortest periods we have found are shown in Figure 31(*a-d*). The shortest relative periodic orbit with $T_p = 16.4$ is also the most unstable, with one positive Floquet exponent equal 0.328. The other short orbits are less unstable, with the largest Floquet exponent in the range 0.018 – 0.073, typical of the long time attractor average.

We have found relative periodic orbits which stay close to the unstable manifold of E_2. As is illustrated in Figure 31(*e-h*), all such orbits have shift $\ell_p \approx L/4$, similar to the shift of orbits within the unstable manifold of E_2, which start at E_2 and converge to $\tau_{1/4}E_2$ (see Figure 26). This observation suggests that the 'cage' of unstable manifolds of equilibria plays an important role in organizing the chaotic dynamics of the Kuramoto-Sivashinsky equation. Yet they do not tell the whole story. As we will see in Chapter 8 the unstable manifolds of the relative equilibria play an important role as well.

7.1.3 Pre-periodic orbits

As discussed in Sect. 5.1.8, a relative periodic orbit will be periodic, i.e., $\ell_p = 0$, if it either **(a)** lives within the $\mathrm{Fix}\,(\mathrm{D}_1)$ antisymmetric subspace, $-u(-x,0) = u(x,0)$, or **(b)** returns to its reflection after a period: $u(x,T_p) = -u(-x,0)$, and is thus periodic with period $2T_p$. The dynamics of Kuramoto-Sivashinsky system in the antisymmetric subspace and periodic

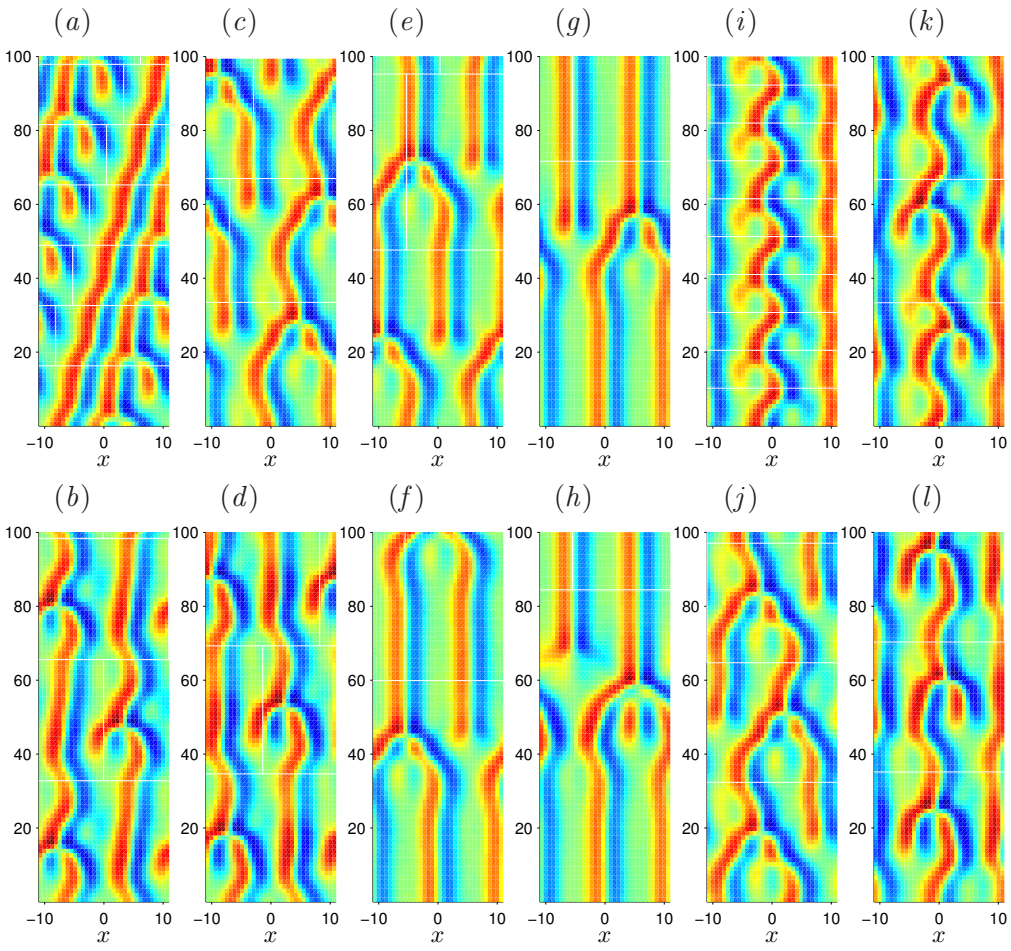

Figure 31: Selected relative periodic and pre-periodic orbits of Kuramoto-Sivashinsky system with $L = 22$: (a) $T_p = 16.3$, $\ell_p = 2.86$; (b) $T_p = 32.8$, $\ell_p = 10.96$; (c) $T_p = 33.5$, $\ell_p = 4.04$; (d) $T_p = 34.6$, $\ell_p = 9.60$; (e) $T_p = 47.6$, $\ell_p = 5.68$; (f) $T_p = 59.9$, $\ell_p = 5.44$; (g) $T_p = 71.7$, $\ell_p = 5.503$; (h) $T_p = 84.4$, $\ell_p = 5.513$; (i) $T_p = 10.3$; (j) $T_p = 32.4$; (k) $T_p = 33.4$; (l) $T_p = 35.2$. Horizontal and vertical white lines indicate periodicity and phase shift of the orbits, respectively.

orbits with symmetry **(a)** have been investigated previously [14; 58; 60]. The KS equation with $L = 22$ does not have any periodic orbits of this type.

As discussed in Sect. 5.1.8 the only periodic orbits that we found for the system have isotropy subgroup D_1. We have found over 50 pre-periodic orbits with $T_p < 100$ which possess the symmetry of type **(b)**. Some of the shortest such orbits we have found are shown in Figure 31(*i-l*). Several were found as repeats of pre-periodic orbits during searches for relative periodic orbits with non-zero shifts, while most have been found as solutions of the pre-periodic orbit condition (96) with reflection, which takes form

$$-\mathbf{g}(-\ell)a^*(T_p) = a(0)\,. \tag{134}$$

in the Fourier space representation (compare it to the condition (93) for relative periodic orbits).

7.2 *Energy transfer rates*

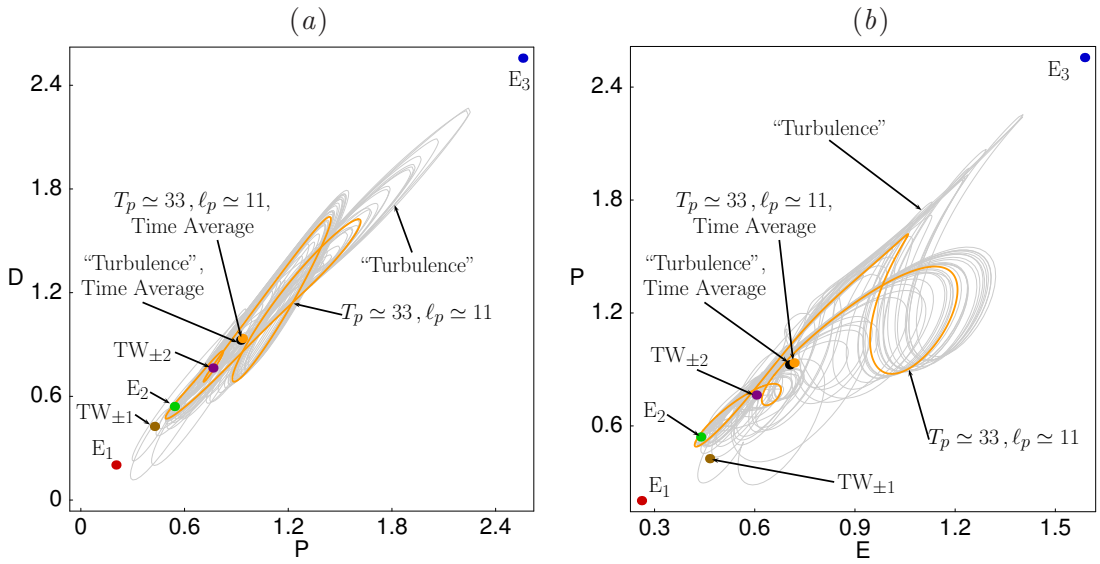

Figure 32: (a) Power input P *vs.* dissipation rate D (b) energy E *vs.* power input P, for several equilibria and relative equilibria, a relative periodic orbit, and a typical 'turbulent' long-time trajectory. System size $L = 22$.

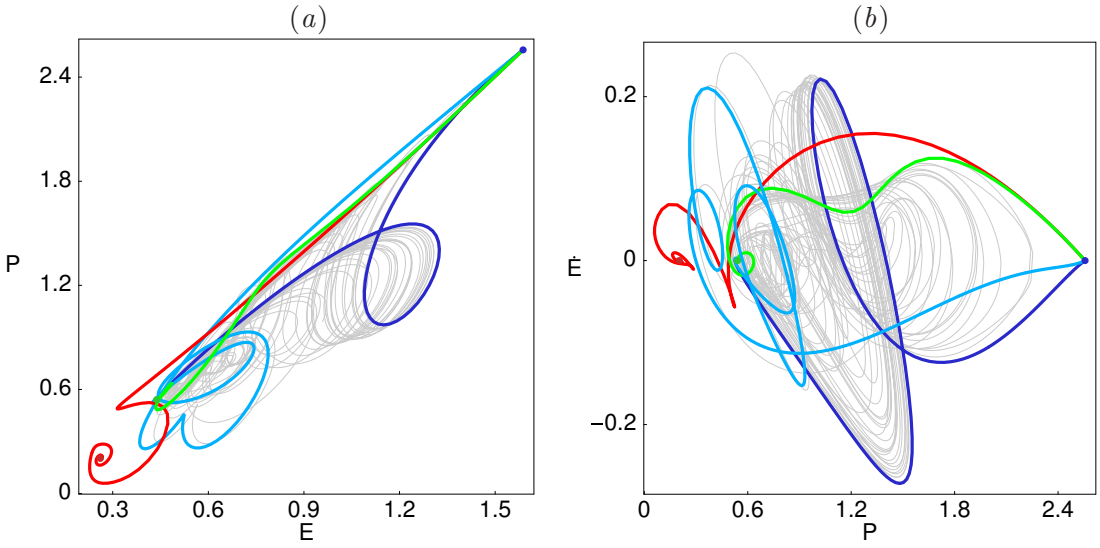

Figure 33: Two projections of the $(E, P, \dot{E})$ representation of the flow. E_1 (red), E_2 (green), E_3 (blue), heteroclinic connections from E_2 to E_3 (green), from E_1 to E_3 (red) and from E_3 to E_2 (shades of blue), superimposed over a generic long-time 'turbulent' trajectory (grey). System size $L = 22$.

In Figure 32 we plot (105), the time-dependent $\dot{E}$ in the power input P *vs.* dissipation rate D plane, for $L = 22$ equilibria and relative equilibria, a selected relative periodic orbit,

and for a typical 'turbulent' long-time trajectory.

Projections from the ∞-dimensional phase space onto the 3-dimensional (E, P, D) representation of the flow, such as Figures 32 and 33, can be misleading. The most one can say is that if points are clearly separated in an (E, P, D) plot (for example, in Figure 32 E_1 equilibrium is outside the recurrent set), they are also separated in the full phase space. Converse is not true – states of very different topology can have similar energies.

An example is the relative periodic orbit $(T_p, \ell_p) = (32.8, 10.96)$ (see Figure 31(b)) which appears well embedded within the turbulent flow. The mean power $\overline{P_p}$ evaluated as in (107), see Figure 32, is numerically quite close to the long-time turbulent time average $\overline{P}$. Similarly close prediction of mean dissipation rate in the plane Couette flow from a single-period periodic orbit computed by Kawahara and Kida [54] has lead to optimistic hopes that 'turbulence' is different from low-dimensional chaos, insofar that the determination of one special periodic orbit could yield all long-time averages. Regrettably, not true – as always, here too one needs a hierarchy of periodic orbits of increasing length to obtain accurate predictions [20].

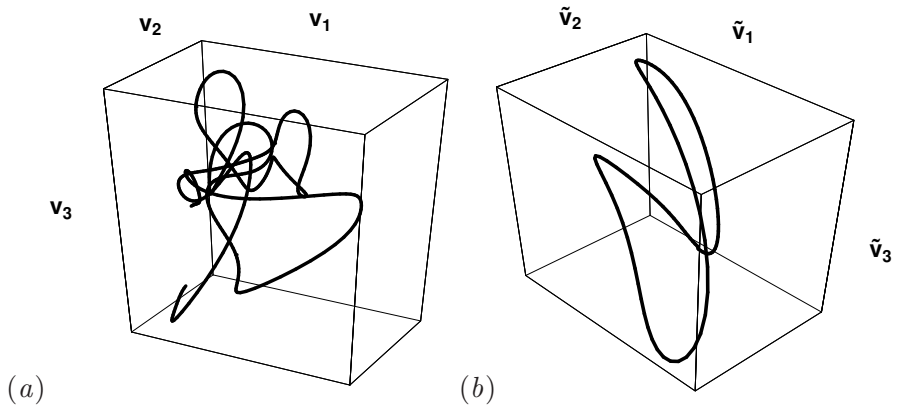

Figure 34: The relative periodic orbit with $(T_p, \ell_p) = (33.5, 4.04)$ from Figure 31 (c) which appears well embedded within the turbulent flow: (a) A stationary phase space projection, traced for four periods T_p. The coordinate axes v_1, v_2, and v_3 are those of Figure 26; (b) In the co-moving mean velocity frame, traced for one period T_p.

For any given relative periodic orbit a convenient visualization is offered by the *mean velocity frame*, i.e., a reference frame that rotates with velocity $v_p = \ell_p/T_p$. In the mean velocity frame a relative periodic orbit becomes a periodic orbit, as in Figure 34 (b). However, each relative periodic orbit has its own mean velocity frame and thus sets of relative periodic orbits are difficult to visualize simultaneously.

CHAPTER VIII

KURAMOTO-SIVASHINSKY REDUCED PHASE SPACE

8.1 Visualization

To visualize the reduced phase space of KS flow we will use a moving frame to compute the first few fundamental invariants of the action of SO(2) and, following the example of Complex Lorenz equations of Sect. 4.1.2.2, modify these invariants to overcome these singularities. This will help us understand what the invariant objects of importance in organizing the phase space are. The final goal is to choose Poincaré sections that capture the dynamics but on which we can define local slices, implement symmetry reduction on the Poincaré sections applying a moving frame on the points of intersection of trajectories with the Poincaré sections and finally construct return maps of the dynamics. At this point we do not quotient out the discrete symmetry. This can always do afterwards by utilizing a fundamental domain, as in Chapter 3.

We begin by computing invariants for the "standard action" (20) of SO(2) on $\mathbb{C}^N \cong \mathbb{R}^{2N}$ which we write here as

$$\begin{pmatrix} \overline{b}_k \\ \overline{c}_k \end{pmatrix} = \begin{pmatrix} \cos(k\theta) & -\sin(k\theta) \\ \sin(k\theta) & \cos(k\theta) \end{pmatrix} \begin{pmatrix} b_k \\ c_k \end{pmatrix}, \quad k = 1, \dots N\,. \tag{135}$$

with $a_k = b_k + ic_k\,,\ b_k, c_k \in \mathbb{R}$. The choice of a slice is arbitrary and thus, after some experimentation, we choose one that results in convenient algebra. Define the slice by

$$K_1(a) = c_1 = 0\,, \qquad b_1 > 0 \tag{136}$$

which leads to the normalization equation

$$\overline{c}_1 = \sin\theta\, b_1 + \cos\theta\, c_1 = 0\,. \tag{137}$$

from which we obtain the moving frame

$$\theta = -\tan^{-1}\frac{c_1}{b_1}\,, \tag{138}$$

where, as noted in Chapter 4, $\tan^{-1}$ distinguishes quadrants. Substituting the moving frame into the rest of (138) we get the fundamental invariants for the action of SO(2) in Fourier space of Kuramoto-Sivashinsky equation. The simplifications of expressions were performed using computer algebra system Mathematica. Computation of 255 invariants for $n = 128$ took approximately 20 minutes on a typical processor. We list the first 11 invariants on Table 3. It is important to note that computation in each irreducible subspace (for each k in (138)) can be carried out independently and thus we can parallelize the computations and also avoid recomputing invariants when increasing N. For the present visualization purposes, though, the invariants listed in Table 3 are more than enough.

As was the case in Complex Lorenz equations example in Chapter 4, there is an obvious singularity at $b_1 = c_1 = 0$ that can be corrected by substituting r_1 with $r = \sum_{i=1}^{N}(b_i^2 + c_i^2)$ in the denominators. Here we will instead use $r = \sum_{i=1}^{3}(b_i^2 + c_i^2)$ since dynamics in our case

Table 3: First 11 fundamental invariants for the standard action (138) of SO(2) on $\mathbb{R}^{2N}$.

$$u_1 = r_1 = \sqrt{b_1^2 + c_1^2}$$

$$u_3 = \frac{b_2(b_1^2-c_1^2)+2b_1c_1c_2}{r_1^2} \qquad u_4 = \frac{-2b_1b_2c_1+(b_1^2-c_1^2)c_2}{r_1^2}$$

$$u_5 = \frac{b_1b_3(b_1^2-3c_1^2)-c_1(-3b_1^2+c_1^2)c_3}{r_1^3} \qquad u_6 = \frac{-3b_1^2b_3c_1+b_3c_1^3+b_1^3c_3-3b_1c_1^2c_3}{r_1^3}$$

$$u_7 = \frac{b_4(b_1^4-6b_1^2c_1^2+c_1^4)+4b_1c_1(b_1^2-c_1^2)c_4}{r_1^4} \qquad u_8 = \frac{4b_1b_4c_1(-b_1^2+c_1^2)+(b_1^4-6b_1^2c_1^2+c_1^4)c_4}{r_1^4}$$

$$u_9 = \frac{b_1b_5(b_1^4-10b_1^2c_1^2+5c_1^4)+c_1(5b_1^4-10b_1^2c_1^2+c_1^4)c_5}{r_1^5} \qquad u_{10} = \frac{-b_5c_1(5b_1^4-10b_1^2c_1^2+c_1^4)+b_1(b_1^4-10b_1^2c_1^2+5c_1^4)c_5}{r_1^5}$$

$$u_{11} = \frac{b_6(b_1^6-15b_1^4c_1^2+15b_1^2c_1^4-c_1^6)+2b_1c_1(3b_1^4-10b_1^2c_1^2+3c_1^4)c_6}{r_1^6} \qquad u_{12} = \frac{-2b_1b_6c_1(3b_1^4-10b_1^2c_1^2+3c_1^4)+(b_1^6-15b_1^4c_1^2+15b_1^2c_1^4-c_1^6)c_6}{r_1^6}$$

like to visit E_2 and E_3 and this choice is enough to prevent the denominator from vanishing at any region of phase space of dynamical interest. Even with this modification one has to note that problems are still present: the invariants of Table 3 vanish at E_2 and E_3 (in general they vanish on $b_1 = c_1 = 0$). In principle this is not a problem since we want to carry out reduction in the principal stratum. In practice this causes two important equilibria to be mapped to the origin and leads to phase space portraits as in Figure 35. The neighborhood of E_2 and E_3 which is where we would like to get some intuition about the behavior of relative periodic orbits, has been squeezed into a kink shaped structure. Inspection of the invariants in Table 3 reveals that the problem is caused by b_1 and c_1 (which vanish at E_2, E_3) appearing in all monomials in the numerators. This is related to the fact that we have chosen the slice in the $k = 1$-irreducible subspace which introduces b_1 and c_1 through the substitution of (138) into (137). Note that the slice does not exist when $b_1 = c_1 = 0$, as there the group action fails to be regular when restricted on the $k = 1$-irreducible subspace. We still lack group-theoretical understanding of this behavior. We could overcome this difficulty by using the second, third, or sixth Fourier mode to setup the moving frame but then the expressions we get after substitution cannot be fully simplified and we loose the ability to manipulate the denominators. We will use a higher mode to setup the moving frame in the numerical implementation, though, after we define suitable Poincaré sections, see Chapter 9.

For visualization purposes we overcome the problem by modifying the invariants of Table 3 as follows. We observe that the invariants come as either symmetric or antisymmetric under the action of $D_1 \subset O(2)$. We modify the symmetric invariants by adding a term $\sqrt{b_i^2 + c_i^2}$ where i labels the corresponding irreducible subspace (Fourier mode). The new invariants are listed in Table 4. One has to note that such a modification is not unique as any linear combination of invariants is an invariant. The basic requirement is that the invariants remain linearly independent, which can be easily verified for the present choice. The motivation behind this choice, apart from its simplicity (the magnitudes of Fourier modes are SO(2)-invariant) is that if we set up a slice by $c_i = 0$ then the invariant that we get associated with the i'th irreducible subspace is $\sqrt{b_i^2 + c_i^2} = 0$ (and the trivial invariant 0). A linear combination of invariants resulting from more than one moving frame is a natural choice since the problem is caused by only taking into account the $i = 1$-mode in setting up the moving frame. Computing a full set of invariants using a moving frame in every irreducible subspace would be time consuming. For the group action we examine here the algebra required to obtain explicit expressions was not carried out by and thus we only

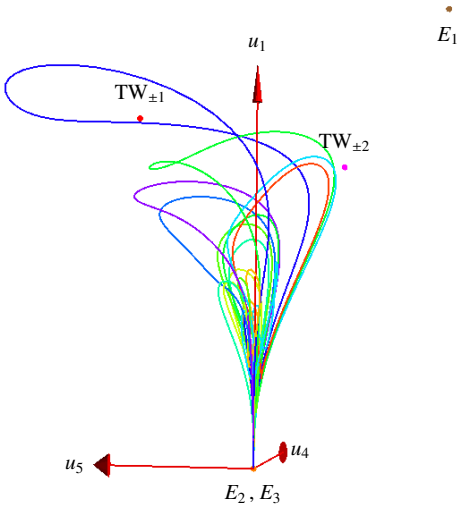

Figure 35: Phase space portrait of $L = 22$ Kuramoto-Sivashinsky dynamics projected to invariants given in Table 3. The trajectories shown are 20 short relative periodic orbits.

use the simplest available invariants, the Fourier magnitudes. An other choice would be to replace the D_1-invariant by the magnitudes instead of forming a linear combination, but we have found that the resulting phase space portraits are not as useful.

Phase space projections on the invariants of Table 4 are shown in Figures 36 to 37. Visualizing the unstable manifold of $TW_{\pm 1}$ is not a straightforward task, since it is 4-dimensional, see Table 1. Nevertheless, we observe that the ratio of real parts of the leading stability eigenvalues for the case of $TW_{\pm 1}$ is approximately 3.4 and thus we expect that the continuation of the strongly unstable eigenspace will play the dominant role. Thus we can get an idea of the importance of the unstable manifold of $TW_{\pm 1}$ for the dynamics by plotting the continuation of the $\lambda^{(1,2)}$ eigenplane under the flow, until just after it appears to fold back to itself. The way in which sample relative periodic orbits follow the unstable manifold in Figure 36 for some time before they visit different regions of state space reveals the importance of this object in organizing the flow, even though the immediate neighborhood of $TW_{\pm 1}$ is not visited by the "turbulent" dynamics or the relative periodic orbits. At this time these observations are of a rather speculative character as projections are frequently misleading, for instance the relative periodic orbit labeled $T = 40.14$ in Figure 36 is not tracking the unstable manifolds as well as implied by the figures, a fact that can be seen in different projections. One could observe this already in Figure 36, as the velocity on relative periodic orbit $T = 40.14$ is not aligned with the velocity of trajectories on the manifold. In order to be able to decide whether a relative periodic orbit is really influenced by an unstable manifold we need a notion of distance of the two objects. This distance will be easier to measure once we reduce the dynamics to discrete time maps on suitable Poincaré sections, see Chapter 9.

In Figure 37(b) we can see that the parts of the relative periodic orbits that do not follow the unstable manifold of Q_1 are "captured" by the unstable manifold of E_2. One has to remember that this manifold is restricted in the antisymmetric subspace while the relative periodic orbits live in the full space (more accurately, in the principal stratum). Nevertheless the invariant objects in the antisymmetric subspace provide a boundary for

Table 4: Modified invariants for the standard action of SO(2) on $\mathbb{R}^6$

$$
\begin{aligned}
u_1 = r_1 &= \sqrt{b_1^2 + c_1^2} \\
u_3 &= \frac{b_2\left(b_1^2 - c_1^2\right) + 2b_1c_1c_2}{r^2} \\
u_4 &= \sqrt{b_2^2 + c_2^2} + \frac{-2b_1b_2c_1 + \left(b_1^2 - c_1^2\right)c_2}{r^2} \\
u_5 &= \sqrt{b_3^2 + c_3^2} + \frac{b_1b_3\left(b_1^2 - 3c_1^2\right) - c_1\left(-3b_1^2 + c_1^2\right)c_3}{r^3} \\
u_6 &= \frac{-3b_1^2b_3c_1 + b_3c_1^3 + b_1^3c_3 - 3b_1c_1^2c_3}{r^3} \\
u_7 &= \frac{b_4\left(b_1^4 - 6b_1^2c_1^2 + c_1^4\right) + 4b_1c_1\left(b_1^2 - c_1^2\right)c_4}{r^4} \\
u_8 &= \sqrt{b_4^2 + c_4^2} + \frac{4b_1b_4c_1\left(-b_1^2 + c_1^2\right) + \left(b_1^4 - 6b_1^2c_1^2 + c_1^4\right)c_4}{r^4} \\
u_9 &= \sqrt{b_5^2 + c_5^2} + \frac{b_1b_5\left(b_1^4 - 10b_1^2c_1^2 + 5c_1^4\right) + c_1\left(5b_1^4 - 10b_1^2c_1^2 + c_1^4\right)c_5}{r^5} \\
u_{10} &= \frac{-b_5c_1\left(5b_1^4 - 10b_1^2c_1^2 + c_1^4\right) + b_1\left(b_1^4 - 10b_1^2c_1^2 + 5c_1^4\right)c_5}{r^5} \\
u_{11} &= \frac{b_6\left(b_1^6 - 15b_1^4c_1^2 + 15b_1^2c_1^4 - c_1^6\right) + 2b_1c_1\left(3b_1^4 - 10b_1^2c_1^2 + 3c_1^4\right)c_6}{r^6} \\
u_{12} &= \sqrt{b_6^2 + c_6^2} + \frac{-2b_1b_6c_1\left(3b_1^4 - 10b_1^2c_1^2 + 3c_1^4\right) + \left(b_1^6 - 15b_1^4c_1^2 + 15b_1^2c_1^4 - c_1^6\right)c_6}{r^6}
\end{aligned}
$$

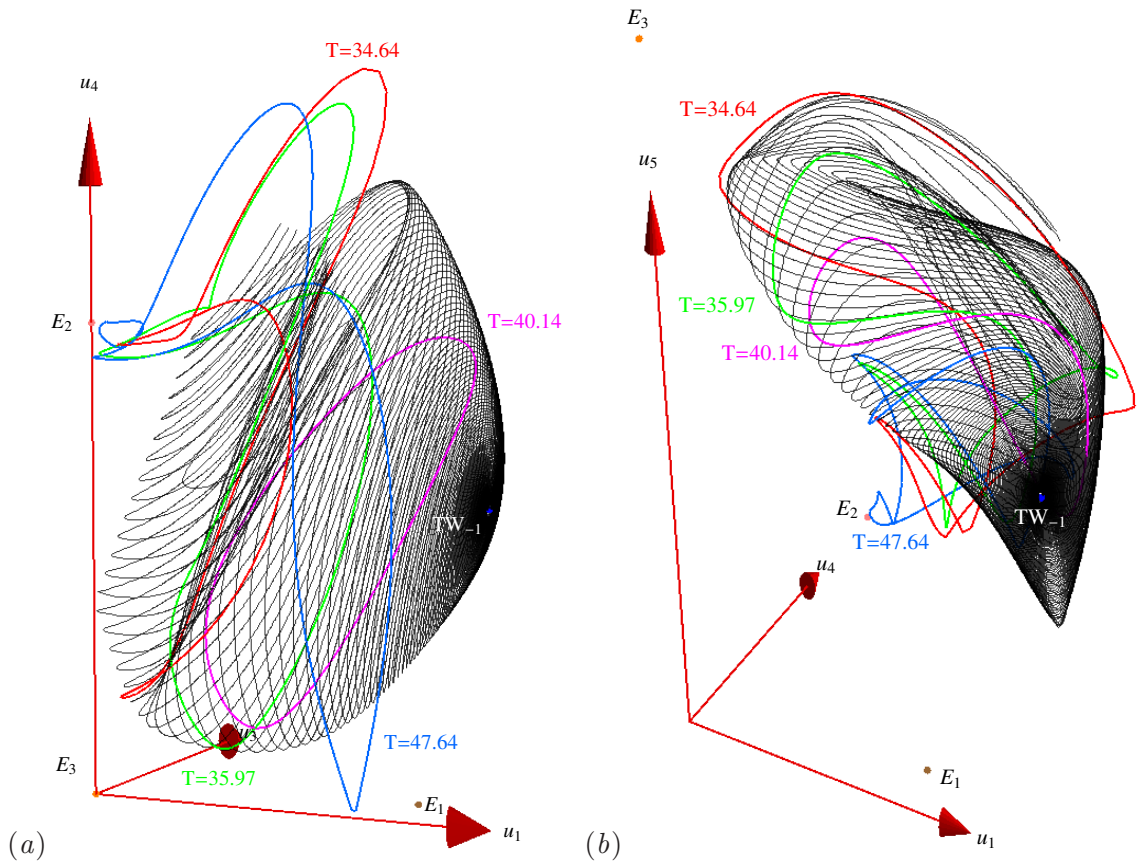

Figure 36: Two different projections of L=22 Kuramoto-Sivashinsky dynamics on invariants given in Table 4. We plot a few selected relative periodic orbits and part of the unstable manifold of TW_{-1} in black, with trajectories originating along the eigenspace corresponding to $\lambda^{(1)}$.

those orbits, in the same sense, that the z-axis in Lorenz flow of Chapter 3 acts as a topological obstruction to the flow. This behavior illustrates our point of view that the dynamics can be described through maps between a set of Poincaré sections, each associated with a (relative) equilibrium and parameterized by intrinsic coordinates such as the length along its unstable manifold. Further pursuing this goal will be subject of future work, see Chapter 9.

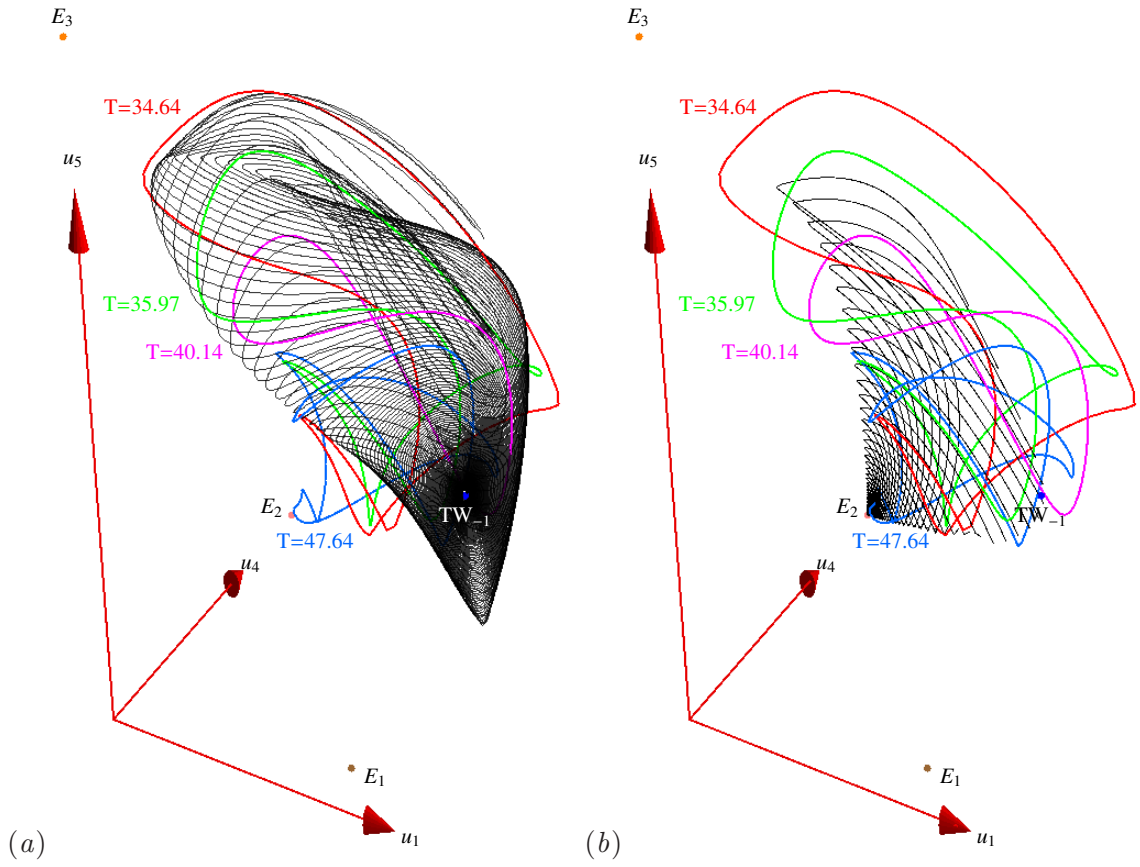

Figure 37: Two different projections of L=22 Kuramoto-Sivashinsky dynamics on invariants given in Table 4. We plot a few selected relative periodic orbits and (a) part of the unstable manifold of TW_{-1} in black, with trajectories originating along the eigenspace corresponding to $\lambda^{(1)}$, (b) part of the unstable manifold of E_1, in black.

CHAPTER IX

CONCLUSION AND FUTURE WORK

9.1 Phase space geometry of spatially extended systems

This thesis contribution to the dynamical system's approach to spatially extended systems is to provide a framework for elucidating state space geometry in the presence of continuous symmetries. The presence of symmetry enriches phase space structure and profoundly influences dynamical behavior. A a striking example is provided by the robust homoclinic (or heteroclinic) connections in Kuramoto-Sivashinsky flow (discussed in Chapter 7) that provide a recurrence mechanism by connecting neighborhoods of saddles along a homoclinic (or heteroclinic) loop and organizing a group of relative periodic orbits around them.

The phase space structure remains unclear until points related by continuous symmetry are identified and the dynamics is visualized in reduced phase space. Once this reduction procedure was carried out for Kuramoto-Sivashinsky flow we were able to identify (in Chapter 8) the "stretching and folding" of the unstable manifold of a relative equilibrium as the mechanism responsible for organizing a different group of relative periodic orbits. Moreover we were able to demonstrate that relative periodic orbits follow the unstable manifold of $\mathrm{TW}_{\pm 1}$ for a while until carried over to the unstable manifold of E_2 therefore revealing the interplay of unstable manifolds of different objects, living in subspaces with different symmetry, in shaping the geometry of the attractor.

The understanding of the geometry of Kuramoto-Sivashinsky equation for $L = 22$ is by no means complete. The obvious next step is to identify suitable Poincaré sections for the study of unstable manifolds and the relative periodic orbits clustered around them. Contrary to the Complex Lorenz equations example of Chapter 4 where a global section was found and the dynamics was described as a first return map to the section, in the case of Kuramoto-Sivashinsky equation we will need more than one sections. Each section will be used to capture the dynamics of the unstable manifold of a (relative) equilibrium until it starts folding back to itself. Parameterizing the intersection of a manifold with the Poincaré section by Euclidean length along it, a forward map from section to section will be constructed and convolution of those maps will result in a return map. This approach meshes very well with the construction of a Markov partition of the dynamics, if such a partition is within reach. A potential obstacle is that unstable manifolds of objects of interest for Kuramoto-Sivashinsky dynamics are often high-dimensional, e.g. 4-dimensional for $\mathrm{TW}_{\pm 1}$, and their visualization and parametrization is a non trivial task. Nevertheless, since the separation of the leading eigenvalues is large, we expect that the continuation of the strongly unstable eigenspace will play the dominant role. Furthermore, we still need to investigate the role played by trajectories originating in the $\lambda^{(1,2)}$ eigenspace of E_1 that are not in the antisymmetric subspace and are therefore expected to play a role in organizing the relative periodic orbits.

9.2 Symmetry reduction

For this geometric understanding to be possible we had to develop a a symmetry reduction procedure for our specific needs and with the following constraints in mind: 1) the method

must work efficiently in high-dimensional phase space, 2) reduction can be local but the local pieces have to be joined together in a way that the global geometry of the attractor is elucidated.

For visualization purposes the method of moving frames is efficient in providing symbolic expressions for invariants up to moderate dimension. When the representation of the symmetry group is a direct sum of irreducible representations, as usually is the case with discretizations of PDEs, we can define a moving frame in one irreducible subspace and construct invariants for the rest of the irreducible subspaces, as necessary for visualization. The invariants thus obtained are singular but the singularities can be removed, or merely moved away from regions of dynamical interest. Then solutions computed in the equivariant variables can be visualized in the invariant basis without any discontinuities introduced.

This leads us to the next step, which is reduction using the geometrical interpretation of moving frames as a group operation that brings points back to a local slice of group orbits. This is a linear operation for any given point and can be implemented efficiently even for high-dimensional discretizations of PDEs. The crucial step is to avoid transformation singularities by restricting attention to local, group-invariant Poincaré sections that do not contain any points on which the transformations become singular.

As noted in the introduction, a method of symmetry reduction for PDEs has been presented by Rowley and Marsden [75], that allows one to integrate a PDE defined in the reduced space along with a reconstruction equation to recover the dynamics of the original problem. This procedure identifies the reduced space $\mathcal{M}/\Gamma$ with a subset of $\mathcal{M}$, called a slice, in the same spirit we identified the reduced space with a cross-section. The reconstruction equation is guaranteed to work locally, in the neighborhood of the initial condition but can fail globally. In ref. [75] choosing a new slice is proposed as a method to overcome this difficulty and the different slices are to be treated as local coordinate charts on $\mathcal{M}/\Gamma$. Yet, this can obscure the study of global aspects of dynamics. It will be interesting to investigate how this difficulty is connected to the singularities present in the moving frame method and whether the insight gained here can help one avoid singularities while still identifying the reduced space with a single slice.

9.3 What are the cycles good for?

Up to this point we have concentrated in the geometry of the phase space and haven't addressed the second constituent of the dynamicist's view of turbulence, the natural measure. The periodic and relative periodic orbits found for Kuramoto-Sivashinsky equation form a skeleton of the dynamics in a geometrical sense but also, through trace formulas and spectral determinants [20], provide a means to accurately evaluate the spectra of evolution operators and evaluate the asymptotic values of observables.

Quoting ref. [20], "the strategy is 1) count, 2) weigh, 3) add up." The weights are given by the stability of the cycles, we can use trace formulas to add them up (in our case the continuous symmetry version in ref. [19]) but we have to start from the beginning and complete step number one. Counting means that we are able to organize and label all cycles up to a given length, establishing a hierarchy that will then be exploited in highly convergent trace formulas or spectral determinants. The need to organize the periodic and relative periodic orbits found for Kuramoto-Sivashinsky equation is underlined in Sect. B.2, where we try to utilize a set of $20,000$ periodic and relative periodic orbits computed by Davidchack [25], by means of periodic orbit theory, but without any understanding of their organization.

APPENDIX A

LYNDON WORDS

Consider a k-symbol alphabet $\mathcal{A}$. Let $\alpha = uv$ and $\beta = vu$, were u and v any word. The words α and β belong to an equivalence class known as a *necklace* and represented by its lexicographically lesser member. For instance, for the binary alphabet consisting of letters 0 and 1 the words {0001, 0010, 0100, 1000} form a necklace represented by 0001. An aperiodic necklace is called a *Lyndon word*.

Lyndon words are of relevance to us because we are often interested in listing all symbolic itineraries that correspond to prime cycles up to length n. For complete k-ary symbolic dynamics this is equivalent to the problem of generating all Lyndon words of length at most n. As n increases the efficiency of the algorithm becomes quickly an issue. An algorithm for generating Lyndon words has been found by Duval [26] and shown to be efficient in ref. [5]. Efficient here means that the running time is proportional to the number of words generated. In Table A we provide pseudocode for Duval's algorithm. For an explanation of the algorithm the reader is referred to ref. [26]. For efficient algorithms to generate necklaces *cf.* ref. [9] and references within.

Table 5: Duval's algorithm for efficient generation of Lyndon words up to length n. Here α and ω are the first and last letters of the alphabet $\mathcal{A}$ and the function $s(x)$ returns the next letter in the alphabet for every letter $x \neq \omega$. The auxiliary variable w is considered a list of length n.

```
set i to 1
set w[1] to α
while i ≠ 0
        for j = 1 to n − i
            set w[i + j] to w[j]
        end for
        append w[1, ..., i − 1] to list of Lyndon words
        set i = n
        while i > 0 and w[i] = ω
                set i to i − 1
        end while
        if i > 0 then set w[i] to s(w[i])
end while
```

APPENDIX B

STABILITY ORDERING FOR KURAMOTO-SIVASHINSKY CYCLES

In this chapter we describe a failed attempt to extract quantitative information from Kuramoto-Sivashinsky equation cycles by organizing them according to their stability. Details on cycle expansions can be found in [20]. Here we only provide some sketchy background to stability ordering by piecing together excerpts from [20].

B.1 Stability ordering of cycle expansions

For generic flows it is often not clear what partition of the phase space generates the "optimal" symbolic dynamics. Stability ordering does not require understanding dynamics in such detail: if you can find the cycles, you can use stability ordered cycle expansions. Stability truncation is thus easier to implement for a generic dynamical system than the curvature expansions [20] that rely on knowledge of the topology of the flow.

Cycles can be detected numerically by searching a long trajectory for near recurrences. The long trajectory method for detecting cycles preferentially finds the least unstable cycles, regardless of their topological length. Another practical advantage of the method (in contrast to Newton method searches) is that it only finds cycles in a given connected ergodic component of phase space, ignoring isolated cycles or other ergodic regions elsewhere in the phase space.

Stability ordering was introduced by Dahlqvist and Russberg [24]. The crucial observation is that stability is multiplicative, so shadowing is approximately preserved by including all terms with pseudocycle stability

$$|\Lambda_{p_1} \cdots \Lambda_{p_k}| \leq \Lambda_{\max} \tag{139}$$

and ignoring all more unstable pseudocycles. For bound flows all trajectories remain confined for all times, implying the conservation of material flow:

$$1/\zeta(0,0) = 1 + \sum_{\pi}{}' \frac{(-1)^k}{|\Lambda_{p_1} \cdots \Lambda_{p_k}|} = 0 \tag{140}$$

which we will try to verify for Kuramoto-Sivashinsky equation.

B.2 Stability ordering for KS cycles

In this section we attempt to numerically check the flow conservation sum rule (140) for Kuramoto-Sivashinsky equation with $L = 22$ using a set of $10,000$ periodic and $10,000$ relative periodic orbits computed by Davidchack [25]. In reduced space both relative periodic orbits and pre-periodic orbits are periodic so they should enter in the same way in dynamical zeta function calculations. the dynamical zeta function $1/\zeta(0,0)$ was evaluated from (140) with stability cutoff $\Lambda_{\max}$ as in (139). After $\Lambda_{\max} \simeq 1200$ dynamical zeta function grows, indicating that we are missing some cycles. To find them we will really have to understand the geometry of the flow.

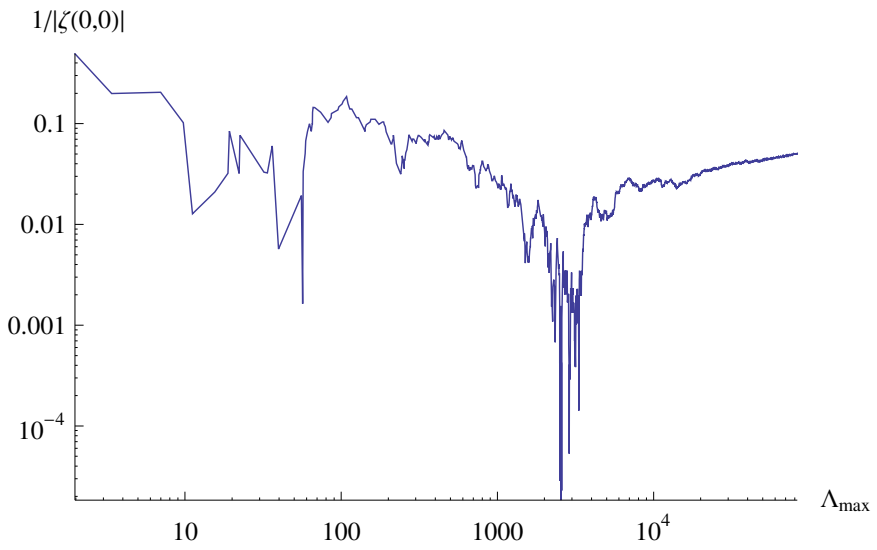

Figure 38: Consistency check of flow conservation relation (140) for Kuramoto-Sivashinsky equation (73) for $L = 22$. Here the dynamical zeta function $1/\zeta(0,0)$ was evaluated from (140) with stability cutoff $\Lambda_{\max}$ as in (139). The maximum stability cutoff shown corresponds to using the 5000 least unstable cycles (periodic orbits and relative periodic orbits) in the set.

Bibliography

[1] Armbruster, D., Guckenheimer, J., and Holmes, P., "Heteroclinic cycles and modulated travelling waves in systems with O(2) symmetry," *Physica D*, vol. 29, pp. 257–282, 1988.

[2] Armbruster, D., Guckenheimer, J., and Holmes, P., "Kuramoto-Sivashinsky dynamics on the center-unstable manifold," *SIAM J. Appl. Math.*, vol. 49, pp. 676–691, 1989.

[3] Bakasov, A. and Abraham, N., "Laser second threshold: It's exact analytical dependence on detuning and relaxation rates," *Phys. Rev. A*, vol. 48, 1993.

[4] Benney, D. J., "Long waves on liquid films," *J. Mathematics and Physics*, vol. 45, p. 150, 1966.

[5] Berstel, J. and Pocchiola, M., "Average cost of Duval's algorithm for generating Lyndon words," *Theoret. Comput. Sci.*, vol. 132, pp. 415–425, 1994.

[6] Bronski, J. C. and Gambill, T. N., "Uncertainty estimates and L_2 bounds for the Kuramoto-Sivashinsky equation," 2006. `arXiv:math/0508481`.

[7] Brown, H. S. and Kevrekidis, I. G., "Modulated traveling waves for the Kuramoto-Sivashinsky equation," in *Pattern Formation: Symmetry Methods and Applications* (Benest, D. and Froeschlé, C., eds.), vol. 5 of *Fields Inst. Commun.*, (Providence, RI), pp. 45–66, AMS, 1996.

[8] Cartan, E., "La méthode du repère mobile, la théorie des groupes continus, et les espaces généralisés," *Exposés de Géométrie*, vol. 5, 1935.

[9] Cattell, K., Ruskey, F., Sawada, J., Serra, M., and Miers, C. R., "Fast algorithms to generate necklaces, unlabeled necklaces, and irreducible polynomials over gf(2)," *J. Algorithms*, vol. 37, pp. 267–282, 2000.

[10] Chenciner, A. `www.imcce.fr/Equipes/ASD/person/chenciner/chenciner.html (June 2006)`.

[11] Chenciner, A., Gerver, J., Montgomery, R., and Simó, C., "Simple choreographic motions of n-bodies: A preliminary study," in *Geometry, mechanics and dynamics* (Newton, P., Holmes, P., and Weinstein, A., eds.), (New York), pp. 287–308, Springer, 2002.

[12] Chenciner, A. and Montgomery, R., "A remarkable solution of the 3-body problem in the case of equal masses," *Ann. Math.*, vol. 152, pp. 881–901, 2000.

[13] Chossat, P. and Lauterbach, R., *Methods in Equivariant Bifurcations and Dynamical Systems*. Singapore: World Scientific, 2000.

[14] Christiansen, F., Cvitanović, P., and Putkaradze, V., "Spatiotemporal chaos in terms of unstable recurrent patterns," *Nonlinearity*, vol. 10, p. 55, 1997.

[15] Constantin, P., Foias, C., Nicolaenko, B., and Temam, R., *Integral manifolds and inertial manifolds for dissipative partial differential equations*. New York: Springer, 1989.

[16] Cox, S. M. and Matthews, P. C., "Exponential time differencing for stiff systems," *J. Comp. Phys.*, vol. 176, no. 2, pp. 430–455, 2002.

[17] Crofts, J. J., *Efficient method for detection of periodic orbits in chaotic maps and flows*. PhD thesis, University of Leicester, Leicester, UK, 2007. arXiv:nlin.CD/0706.1940.

[18] Cushman, R. H. and Bates, L. M., *Global Aspects of Classical Integrable Systems*. Boston: Birkhäuser, 1997.

[19] Cvitanović, P., "Continuous symmetry reduced trace formulas." ChaosBook.org/∼predrag/papers/trace.pdf, 2007.

[20] Cvitanović, P., Artuso, R., Mainieri, R., Tanner, G., and Vattay, G., *Chaos: Classical and Quantum*. Copenhagen: Niels Bohr Institute, 2009. ChaosBook.org.

[21] Cvitanović, P., Davidchack, R. L., and Siminos, E., "State space geometry of a spatio-temporally chaotic Kuramoto-Sivashinsky flow." arXiv:0709.2944; SIAM J. Applied Dynam. Systems, to appear, 2009.

[22] Cvitanović, P. and Eckhardt, B., "Symmetry decomposition of chaotic dynamics," *Nonlinearity*, vol. 6, p. 277, 1993. arXiv:chao-dyn/9303016.

[23] Cvitanović, P., "Chaotic field theory: a sketch," *Physica A*, vol. 288, p. 61, 2000. arXiv:nlin.CD/0001034.

[24] Dahlqvist, P. and Russberg, G., "Cycle expansions for intermittent diffusion," *J. Phys. A*, vol. 24, p. 4763, 1991.

[25] Davidchack, R. L., 2007. Private communication.

[26] Duval, J.-P., "Generation d'une section des classes de conjugaison et arbre des mots de Lyndon de longueur borné," *Theoret. Comput. Sci.*, vol. 60, pp. 255–283, 1988.

[27] Faisst, H. and Eckhardt, B., "Traveling waves in pipe flow," *Phys. Rev. Lett.*, vol. 91, p. 224502, 2003.

[28] Fels, M. and Olver, P. J., "Moving coframes: I. a practical algorithm," *Acta Appl. Math.*, vol. 51, p. 161, 1998.

[29] Fels, M. and Olver, P. J., "Moving coframes: II. regularization and theoretical foundations," *Acta Appl. Math.*, vol. 55, p. 127, 1999.

[30] Feng, B., "Multiplicity and structures for traveling wave solutions of the Kuramoto-Sivashinsky equation," *International Journal of Mathematics and Mathematical Sciences*, vol. 2004, no. 70, pp. 3839–3848, 2004.

[31] Foias, C., Nicolaenko, B., Sell, G. R., and Temam, R., "Inertial manifold for the Kuramoto-Sivashinsky equation," *C. R. Acad. Sci. I-Math*, vol. 301, no. 6, pp. 285–288, 1985.

[32] Fowler, A., Gibbon, J., and McGuinness, M., "The complex Lorenz equations," *Physica D*, vol. 4, p. 139, 1982.

[33] Frigo, M. and Johnson, S. G., "The design and implementation of FFTW3," *Proceedings of the IEEE*, vol. 93, pp. 216–231, 2005.

[34] Frisch, U., *Turbulence*. Cambridge: Cambridge Univ. Press, 1996.

[35] Gatermann, K., *Computer algebra methods for equivariant dynamical systems*. New York: Springer, 2000.

[36] Giacomelli, L. and Otto, F., "New bounds for the Kuramoto-Sivashinsky equation," *Comm. Pure Appl. Math.*, vol. 58, pp. 297–318, 2005.

[37] Gibbon, J. and McGuinness, M., "The real and complex Lorenz equations in rotating fluids and lasers," *Physica D*, vol. 4, p. 139, 1982.

[38] Gibson, J. F., Halcrow, J., and Cvitanović, P., "Visualizing the geometry of state-space in plane Couette flow," *J Fluid Mech.*, vol. 611, pp. 107–130, 2008. `arXiv:0705.3957`.

[39] Gilmore, R. and Letellier, C., *The Symmetry of Chaos*. Oxford: Oxford Univ. Press, 2007.

[40] Golubitsky, M. and Stewart, I., *The symmetry perspective*. Boston: Birkhäuser, 2002.

[41] Golubitsky, M., Stewart, I., and Schaeffer, D. G., *Singularities and Groups in Bifurcation Theory, vol. II*. New York: Springer, 1988.

[42] Greene, J. M. and Kim, J. S., "The steady states of the Kuramoto-Sivashinsky equation," *Physica D*, vol. 33, pp. 99–120, 1988.

[43] Haken, H., "At least one lyapunov exponent vanishes if the trajectory of an attractor does not contain a fixed point," *Phys. Lett. A*, vol. 94, pp. 71–72, 1983.

[44] Halcrow, J., *Geometry of turbulence: An exploration of the state-space of plane Couette flow*. PhD thesis, School of Physics, Georgia Inst. of Technology, Atlanta, 2008. `ChaosBook.org/projects/theses.html`.

[45] Halcrow, J., Gibson, J. F., and Cvitanović, P., "Equilibrium and traveling-wave solutions of plane Couette flow." `arXiv:0808.3375`, submitted to J. Fluid Mech., 2008.

[46] Halcrow, J., Gibson, J. F., Cvitanović, P., and Viswanath, D., "Heteroclinic connections in plane Couette flow," *J. Fluid Mech.*, vol. 621, pp. 365–376, 2009. `arXiv:0808.1865`.

[47] Hof, B., van Doorne, C. W. H., Westerweel, J., Nieuwstadt, F. T. M., Faisst, H., Eckhardt, B., Wedin, H., Kerswell, R. R., and Waleffe, F., "Experimental observation of nonlinear traveling waves in turbulent pipe flow," *Science*, vol. 305, pp. 1594–1598, 2004.

[48] Hooper, A. P. and Grimshaw, R., "Travelling wave solutions of the Kuramoto-Sivashinsky equation," *Wave Motion*, vol. 10, pp. 405–420, Oct. 1988.

[49] Hopf, E., "A mathematical example displaying features of turbulence," *Comm. Appl. Math.*, vol. 1, pp. 303–322, 1948.

[50] Jolly, M., Rosa, R., and Temam, R., "Evaluating the dimension of an inertial manifold for the kuramoto-sivashinsky equation," *Advances in Differential Equations*, vol. 5, pp. 31–66, 2000.

[51] Jolly, M., Rosa, R., and Temam, R., "Accurate computations on inertial manifolds," *SIAM J. Scientific Computing*, vol. 22, p. 2216, 2001.

[52] Jolly, M., Kevrekidis, I., and Titi, E., "Approximate inertial manifolds for the Kuramoto-Sivashinsky equation: Analysis and computations," *Physica D: Nonlinear Phenomena*, vol. 44, pp. 38–60, Aug. 1990.

[53] Kassam, A.-K. and Trefethen, L. N., "Fourth-order time stepping for stiff PDEs," *SIAM J. Sci. Comput.*, vol. 26, no. 4, pp. 1214–1233, 2005.

[54] Kawahara, G. and Kida, S., "Periodic motion embedded in plane Couette turbulence: regeneration cycle and burst," *J. Fluid Mech.*, vol. 449, pp. 291–300, 2001.

[55] Kevrekidis, I. G., Nicolaenko, B., and Scovel, J. C., "Back in the saddle again: a computer assisted study of the Kuramoto-Sivashinsky equation," *SIAM J. Appl. Math.*, vol. 50, no. 3, pp. 760–790, 1990.

[56] Krupa, M., "Bifurcations of relative equilibria," *SIAM J. Math. Anal.*, vol. 21, pp. 1453–1486, 1990.

[57] Kuramoto, Y. and Tsuzuki, T., "Persistent propagation of concentration waves in dissipative media far from thermal equilibrium," *Progr. Theor. Phys.*, vol. 55, p. 365, 1976.

[58] Lan, Y., *Dynamical systems approach to 1-d spatiotemporal chaos – A cyclist's view*. PhD thesis, School of Physics, Georgia Institute of Technology, Atlanta, 2004. `ChaosBook.org/projects/theses.html`.

[59] Lan, Y. and Cvitanović, P., "Variational method for finding periodic orbits in a general flow," *Phys. Rev. E*, vol. 69, p. 016217, 2004. `arXiv:nlin.CD/0308008`.

[60] Lan, Y. and Cvitanović, P., "Unstable recurrent patterns in Kuramoto-Sivashinsky dynamics," *Phys. Rev. E*, vol. 78, p. 026208, 2008. `arXiv.org:0804.2474`.

[61] Lin, S. P., "Finite-amplitude side-band stability of a viscous film," *J. Fluid Mech.*, vol. 63, no. Apr29, pp. 417–429, 1974. Times Cited:138 Cited References Count:26.

[62] López, V., Boyland, P., Heath, M. T., and Moser, R. D., "Relative periodic solutions of the Complex Ginzburg-Landau equation," *SIAM J. Appl. Dyn. Syst.*, vol. 4, p. 1042, 2006.

[63] Lorenz, E., "Deterministic nonperiodic flow," *J. Atmos. Sci.*, p. 130, 1963.

[64] Manneville, P., *Instabilities, Chaos And Turbulence: An Introduction To Nonlinear Dynamics And Complex Systems*. Imperial College Press, 2004.

[65] Marsden, J. E., Misiolek, G., Ortega, J., Perlmutter, M., and Ratiu, T. S., *Hamiltonian Reduction by Stages*. New York: Springer, 1964.

[66] Marsden, J. E. and Ratiu, T. S., *Introduction to Mechanics and Symmetry*. New York: Springer, 1994.

[67] McCord, C., Montaldi, J., Roberts, M., and Sbano, L., "Relative periodic orbits of symmetric Lagrangian systems," in *Proceedings of "Equadiff 2003* (Dumortier, F. and et.al., eds.), pp. 482–493, 2004.

[68] Michelson, D., "Steady solutions of the Kuramoto-Sivashinsky equation," *Physica D*, vol. 19, pp. 89–111, 1986.

[69] Ning, C. and Haken, H., "Detuned lasers and the complex Lorenz equations: Subcritical and supercritical Hopf bifurcations," *Physica D*, vol. 4, p. 139, 1982.

[70] Olver, P. J., *Classical Invariant Theory*. Cambridge: Cambridge University Press, 1999.

[71] Press, W. H., Flannery, B. P., Teukolsky, S. A., and Vetterling, W. T., *Numerical Recipes in Fortran*. Cambridge: Cambridge Univ. Press, 1996.

[72] Quey, R. E. L., Mahajan, S. M., Rutherford, P. H., and Tang, W. M., "Nonlinear saturation of the trapped-ion mode," *Phys. Rev. Lett.*, vol. 34, pp. 391–394, 1974.

[73] Robinson, J. C., "Inertial manifolds for the Kuramoto-Sivashinsky equation," *Physics Letters A*, vol. 184, no. 2, pp. 190–193, 1994.

[74] Rowley, C. W., Kevrekidis, I. G., Marsden, J. E., and Lust, K., "Reduction and reconstruction for self-similar dynamical systems," *Nonlinearity*, vol. 16, pp. 1257–75, 2003.

[75] Rowley, C. W. and Marsden, J. E., "Reconstruction equations and the Karhunen-Loéve expansion for systems with symmetry," *Physica D*, vol. 142, pp. 1–19, 2000.

[76] Ruelle, D. and Takens, F., "On the nature of turbulence," *Commun. Math. Phys.*, vol. 20, p. 167, 1971.

[77] Sivashinsky, G. I., "Nonlinear analysis of hydrodynamical instability in laminar flames - I. Derivation of basic equations," *Acta Astronaut.*, vol. 4, p. 1177, 1977.

[78] Stoer, J. and Bulirsch, R., *Introduction to Numerical Analysis*. New York: Springer, 1983.

[79] Szebehely, V., *Theory of orbits*. New York: Academic Press, 1967.

[80] Viswanath, D., "Recurrent motions within plane Couette turbulence," *J. Fluid Mech.*, vol. 580, pp. 339–358, 2007. `arXiv:physics/0604062`.

[81] Wedin, H. and Kerswell, R. R., "Exact coherent structures in pipe flow," *J. Fluid Mech.*, vol. 508, pp. 333–371, 2004.